# Design and testing of an assistive Hand Exoskeleton with hybrid architecture

*A dissertation submitted in partial fulfillment of the requirements for the Degree of Doctor of Philosophy in*

INDUSTRIAL ENGINEERING
Scientific Disciplinary Sector ING-IND/13


**Candidate**
Chiara Brogi

**Advisor**
Dott. Ing. Alessandro Ridolfi

**Co-advisor**
Prof. Benedetto Allotta

**Coordinator**
Prof. Giovanni Ferrara

Department of Industrial Engineering
University of Florence
Florence, Italy



XXXVI Ph.D. Cycle - Years 2020/2023

*To my family,*
*to my grandmother,*
*to Leonardo*

**Acknowledgments**

The Ph.D. experience at the University of Florence is now drawing to a close, and I am very grateful to the people who shared with me this period.

First of all, I would like to thank my advisor, Dr. Alessandro Ridolfi, who welcomed me into the group and trusted me since the time of my Bachelor's Degree. I would express my gratitude for his time and advice whenever I needed it and for how much I learned from him as a teacher.

I want to thank my co-advisor, Prof. Benedetto Allotta, who allowed me to work in the field of Robotics, but mostly because he has always pushed me to make my voice heard more.

I thank Prof. Enrico Meli for his significant contribution and for always encouraging me to solve the problems I encountered.

Special thanks go to Nicola, who followed me all the way; he helped, supported, and endured me, trying to quell my anxieties until the very end.

I want to thank my colleagues at the Mechatronic and Dynamic Modeling Laboratory of the Department of Industrial Engineering at the University of Florence for sharing these three years with me.
Special thanks go to Jonathan and Marco, who have always been a guide and always ready to give me advice, and to Gherardo, for his fundamental help with electronics.

I would like to thank my friends, who are always willing to wait for me.

And finally, my family. I thank all my big family for encouraging me in this experience. I especially thank my brother and sister for being able to put up with me throughout this time, for their support and words of confidence; I really thank my mom and dad, who have brought me this far, and I want to thank my grandmother, who, despite her age, always showed curiosity about what I was doing, and her encouragement was never lacking. Last but not least, a huge thank you goes to my boyfriend for his constant support and encouragement and for how much he took care of me during this time.

Thank you all for shaping the person who I am.

*Chiara Brogi. University of Florence, January 2024.*

**Abstract**

Robotic technologies find application in increasingly diverse and heterogeneous environments: among these, the Healthcare System stands out due to its importance to society.
In 2022, the World Health Organization confirmed that the world population age is constantly increasing, and the same goes for chronic diseases, causing a growing number of people with disabilities. Therefore, research in Wearable Robotics for the Healthcare System focuses on developing devices to meet the continuing and increasing demand for assistance and rehabilitation treatment for use in daily life to support ordinary activities or be integrated with functional recovery processes.
Among wearable robotic devices, hand exoskeletons are considered special tools that enable people with hand impairments to interact with the environment by restoring their functional capabilities.

This is the context for the research presented in this thesis and carried out during the Ph.D. period. It was focused on developing a novel hand exoskeleton for assisting users in Activities of Daily Living to regain their independence and improve their quality of life.

An in-depth literature analysis found wearability, portability, safety, comfort, lightness, small overall dimensions, dexterity, efficacy in Activities of Daily Living, sense-of-touch preservation, and affordability as the primary design requirements an assistive hand exoskeleton should meet.

The novel hand exoskeleton presented in this thesis was designed to pursue such requirements. The mechanical design was carried out after a careful and thorough literature review. It is based on an innovative hybrid finger-handling mechanism that includes rigid and soft components to be effective in force transmission but keep the overall dimensions above the finger contained, enabling movements in confined spaces.

The first developed module and the whole hand exoskeleton were evaluated through Range Of Motion and force tests. The results showed that the subject wearing the device could grasp, hold, and manipulate the proposed items but highlighted flaws in the interface between the hand and exoskeleton. At the same time, the need for a more in-depth analysis of the soft architecture emerged. Therefore, a model of the hybrid finger-handling mechanism was developed and preliminary simulated.

The main contribution of this work is the development of a novel hand exoskeleton that meets most requirements for assistive purposes, whose results are promising and an excellent starting point for future developments.

**Parts of this thesis have been published in the following documents:**

**Journals**

- Secciani N., Brogi C., Pagliai M., Buonamici F., Gerli F., Vannetti F., Bianchini M., Volpe Y., Ridolfi A. (2021) Wearable Robots: An Original Mechatronic Design of a Hand Exoskeleton for Assistive and Rehabilitative Purposes. Frontiers in Neurorobotics, 15,750385.
- Bartalucci L., Secciani N., Brogi C., Topini A., Della Valle A., Ridolfi A., Allotta B. (2023). An original mechatronic design of a kinaesthetic hand exoskeleton for virtual reality-based applications. Mechatronics, 90, 102947.
- Vangi M., Brogi C., Topini A., Secciani N., Ridolfi A. (2023). Enhancing sEMG-Based Finger Motion Prediction with CNN-LSTM Regressors for Controlling a Hand Exoskeleton. Machines, 11(7), 747.
- Mirulla A. I., Brogi C., Barone G., Secciani N., Sansom W., Bartalucci L., Ridolfi A., Allotta B., Bragonzoni L. (2023). External devices increasing bone quality in animals: a systematic review. Heliyon.
- Brogi C., Secciani N., Bartalucci L., Di Iorio F., Meli E., Allotta B., Ridolfi A. (2023) An original hybrid-architecture finger mechanism for wearable hand exoskeletons. Mechatronics, 98, 103117.

**Conferences**

- Brogi C., Secciani N., Bartalucci L., Pagliai M., Allotta B., Ridolfi A., and Rindi A. (2022). Wearable Exoskeletons for Hand Assistance: Concept and Design of a Thumb Module with Hybrid Architecture. In Symposium on Robot Design, Dynamics and Control (pp. 70-78). Springer, Cham.
- Brogi C., Raggi A., Secciani N., Volpe Y., Ridolfi A. (2022). A Passive, Customizable and Kinetically-Accurate Hand Replica for Testing Assistive and Rehabilitative Hand Exoskeleton Systems. In The International Conference of IFToMM ITALY (pp. 505-513). Springer, Cham.
- Brogi C., Bartalucci L., Secciani N., Ridolfi A., Meli E., Allotta B. (2023). Hybrid-architecture finger mechanism towards dexterous and effective wearable hand exoskeletons, In I-RIM Conference 2023.

- Vangi M., Brogi C., Topini A., Secciani N., Ridolfi A., Allotta B. (2023). CNN-LSTM regressor towards dexterous sEMG-based control of wearable hand exoskeletons, In I-RIM Conference 2023.

# Contents

# List of Figures

# Acronyms

**a/a** abduction/adduction

**ABS** Acrylonitrile Butadiene Styrene

**ADLs** Activities of Daily Living

**ARAT** Action Research Arm Test

**CAD** Computer Aided Design

**CMC** CarpoMetaCarpal

**D-H** Denavit-Hartenberg

**DIP** Distal InterPhalangeal

**DOF** Degree Of Freedom

**DOFs** Degrees Of Freedom

**EE** End-Effector

**f/e** flexion/extension

**FDM** Fused Deposition Modeling

**FEM** Finite Element Method

**FSR** Force Sensing Resistor

**IP** Proximal Interphalangeal

**IRCCS** Istituto di Ricovero e Cura a Carattere Scientifico

**LP** Low Power

**MCP** MetaCarpoPhalangeal

**MDM Lab** Mechatronics and Dynamic Modeling Laboratory

**MoCap** Motion Capture

**PCB** Printed Circuit Board

**PIP** Proximal InterPhalangeal

**RCM** Remote Center of Motion

**ROM** Range Of Motion

**SD** Standard Deviation

**sEMG** surface ElectroMyoGraphy

**SMA** Spinal Muscular Atrophy

**UNIFI DIEF** Department of Industrial Engineering at the University of Florence

**WHO** World Health Organization

# Chapter 1

# Introduction

THE word *robot* was first used by the writer Karel Čapek in his play Rossum's Universal Robots, published in 1920, and comes from the Slavic word *robota*, which means serf or labourer [1]. The game is set in a factory that produces artificial people called *robot*, which can be mistaken for humans. In 1954, George Devol developed the Unimate, the first digitally operated and programmable industrial robot, which was later sold to General Motors and used for handling die-cast fabricated parts taken from a line and welded onto automobile bodies. This invention laid the foundation for the modern robotics industry [1].
The term *Robotics* means an interdisciplinary field involving mechanics, electronics, and computer programming, which studies the development, functioning, and use of robots that can help and assist humans by improving their functions. The technological advances of the Fourth Industrial Revolution have led Robotics to find application in increasingly diverse and heterogeneous environments, such as the military, industrial, deep sea, space exploration, agricultural, kitchen, and healthcare. Among them, robotic technologies addressed for the Healthcare System have high relevance since different societal factors drive them, such as the need for improving medical procedures, reducing side effects and, in turn, recovery time, or for developing new medical procedures among unexplored applications, globally the need for making the access to personalised healthcare system as free as possible from physical, social, and economic distances [2].

The introduction of robotic devices in the Healthcare System could be beneficial to reduce the clinicians' workflow pressure, support clinical practices, such as rehabilitation treatments or surgical procedures, prevent illness, and improve

the standard and accessibility of care [2, 3]. The surgical, rehabilitation, mobility, radiotherapy, and assistive robots are among the most frequently detected in the literature [3]. Surgical Robotics is one of the most successful and advanced areas of Robotics [3, 4]. Many surgical robots used to assist surgeons in performing their procedures are already commercially available with impressive economic returns (e.g., the *Da Vinci robot* from Intuitive Surgical [1], *neuromate* from Renishaw [2], *enos* from Titan Medical [3]). Nonetheless, the research in this field is still highly active, focusing on developing new systems for unmet clinical needs or increasing the level of autonomy of devices established in specific clinical applications [4].
Currently, rehabilitation and assistive robots that can serve to improve dexterity, achieve rehabilitation goals, or promote mobilisation [3] are also under study. Rehabilitation means all the interventions needed to recover lost physical, cognitive, or social functions due to ageing or a health condition, including chronic diseases, disorders, injuries, or traumas [5]. Different forms of disabilities can also be expected at a younger age, e.g., due to traumas or congenital disorders [6]. The assistive technology instead should provide those products and services that improve individual's abilities and independence, thus promoting their well-being while reducing the need for formal support services, long-term care, and the work of caregivers, which are in short supply in hospitals, rehabilitation centres, and assisted living communities [7]. Robotic devices may represent special tools to answer the need for rehabilitation and assistive facilities, which is mainly unmet and predicted to increase due to changes in population health and characteristics. The World Health Organization (WHO) declared in 2022 that the world population age is steadily increasing and that by 2030, 1 in 6 people will be aged 60 years or over [4]. In addition to the age, the occurrence of chronic diseases is increasing as well [8], thus resulting in a growing number of people with disabilities (currently, around 16% of the global population [5]), who experience limitations in everyday life.

The research concerning Robotics for assistance and rehabilitation is a growing, promising, and challenging field, increasingly explored due to the medical

[1]https://www.intuitive.com/en-us/products-and-services/da-vinci (accessed January 31, 2024)

[2]https://www.renishaw.it/it/sistema-robotico-neuromate-per-la-neurochirurgia-stereotassica–10712 (accessed January 31, 2024)

[3]https://titanmedicalinc.com/enos/ (accessed January 31, 2024)

[4]https://www.who.int/news-room/fact-sheets/detail/ageing-and-health (accessed January 31, 2024)

[5]https://www.who.int/news-room/fact-sheets/detail/disability-and-health (accessed January 31, 2024)

and social needs mentioned above [9]. Robotic systems can be addressed for these purposes to people with disabilities or any impairment to reduce their caregivers' efforts. Among the others, wearable devices, which *"can extend, complement, substitute or enhance human functions and capabilities or empower or replace (a part of) the human limb where it is worn"* [10], and specifically robotic exoskeletons are the most tackled and developed [9, 11]. Exoskeletons are those wearable technologies designed to enable, augment, or assist physical activities [12]. They consist of active orthoses to support and help patients with motor disabilities, which are deployable for daily activities [9]. Upper and lower limbs are the most studied body parts since their functions' recovery is essential to regain daily independence [11, 13]. Significantly, the hand is a dexterous tool that allows the human to interact with the environment by tightening, grasping, touching, manipulating, feeling, and communicating [14, 15], hence enabling performing the so-called Activities of Daily Living (ADLs) at home, at school, at work [16]. Therefore, hand function loss represents a significantly limiting disability that can affect people of all ages and can be due to different causes: increasing age, unhealthy habits, traumas, diseases (e.g., stroke, Parkinson's, senile dementia, tremors), or congenital disorders. All these conditions might reduce or preclude hand capabilities, leading to complete hand dysfunction [6, 17, 18].

This crucial need is significantly pushing the research activity in this field. At the current state of the art, on one side, rehabilitative exoskeletons are designed to enable accurate, highly repetitive, intensive, and adaptive to patient's performance and need treatments to recover lost motor functions [19, 20]. Some devices are already commercially available (e.g., *Gloreha* from Idrogenet [6] or *InMotion ARM* from Bionick [7]) and exploited for treatments in clinical environments. Despite their promising results, more studies with a larger participant size are needed to compare the robot-assisted therapy to the conventional one [21, 22]. On the other side, assistive exoskeletons are designed to support the users in everyday activities, e.g., eating, dressing, and toileting, to restore their independence. To this aim, they should meet portability, wearability, dexterity, and affordability requirements [20]; they should be effective in force transmission, designed for the specific user needs and anatomy, comfortable, and safe. Although research is expanding significantly in this direction, the development of these devices is highly complex since their primary requirements are often antagonistic (e.g., the customization concept might be synonymous with high

[6] https://www.gloreha.it/ (accessed January 31, 2024)

[7] https://bioniklabs.com/inmotion-arm/ (accessed January 31, 2024)

cost), and it is difficult to find solutions in the literature that satisfy all of them.

The research activity presented in this thesis is placed right in this context. It was focused on developing a hand exoskeleton that would meet design requirements for assistive purposes, which are still largely unmet. It will also be usable during low-intensity rehabilitation sessions since the requirements for the assistive purpose are the most severe and challenging to meet. The main aim was to develop a low-cost device capable of adequately assisting possible users in daily activities to regain their independence and improve their quality of life. Its design is founded on an innovative hybrid finger-handling mechanism, which includes both rigid and soft components to be effective in force transmission, limiting the overall dimensions of the mechanism on each finger to enable movement in confined spaces. All the design choices were made to achieve the best solution to meet these requirements, reducing the trade-offs. Thus, this thesis will present the mechanical design of the device, carried out following a careful and thorough literature review, concluding with preliminary tests performed on a healthy subject.

## 1.1 Overall framework

The research activity that will be presented in this thesis started in November 2020 and has been conducted within the Mechatronics and Dynamic Modeling Laboratory (MDM Lab) of the Department of Industrial Engineering at the University of Florence (UNIFI DIEF). The research group started focusing on wearable robots in 2013 when a patient suffering from Spinal Muscular Atrophy (SMA) asked the group, already active in Underwater Robotics, to develop a device to help him with daily activities. This demand resulted in the beginning of a highly relevant and ever-evolving activity that is constantly setting new goals for technological development.

The first prototype (Figure 1.1) was designed and tested on the patient who had expressed the request as voluntarily enrolled in the activity. In 2016, a collaboration with the Don Carlo Gnocchi Foundation of Florence (Istituto di Ricovero e Cura a Carattere Scientifico (IRCCS), Scandicci, Firenze) — a private nonprofit foundation for personalised rehabilitation and care born in 1952 — allowed for an increase in possible target subjects, the use of instrumentation the rehabilitation centre is provided with, and last but not least established a dialogue with the clinical counterpart, which is fundamental for developing systems that interface with humans and that clinicians introduce to the patients during the rehabilitation process. The collaboration, still lasting today, enriched

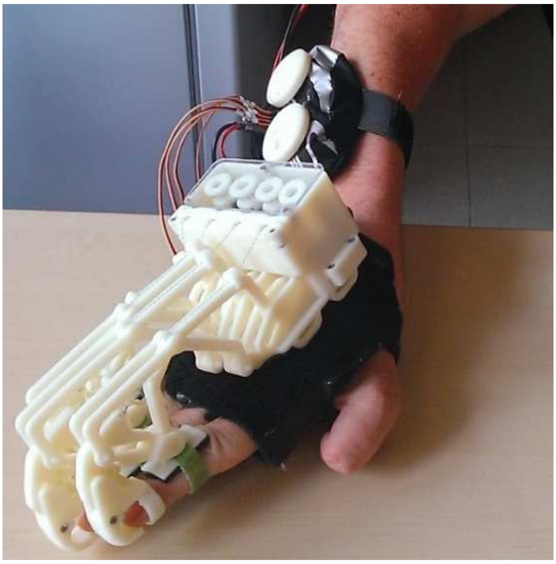

Figure 1.1: The first prototype developed by the MDM Lab.

the research group's knowledge, which found a crucial activity partner in the centre. Different prototypes were developed over the years, and the strengths and flaws that emerged during the last tests performed at the IRCCS centre laid the foundation for studying the completely renewed device presented in this thesis.
This activity was made possible thanks to two research projects (Figure 1.2): R3COVER ("Riabilitazione Robot assistita per il Recupero di funzioni neurocognitive e motorie") and THE ("Tuscany Health Ecosystem"). The former was a two-year project funded by Fondazione CR Firenze from December 2021. Its primary purpose was to develop a multicomponent and modular platform for robot-assisted rehabilitation. The platform was thought to include a robotic manipulator provided with a soft gripper, wearable tactile stimulators, and a hand exoskeleton, allowing for a comfortable human-robot interaction. The platform will enable cooperation between the manipulator and patient involved in the physical and cognitive therapy session, while the patient itself wears the exoskeleton that helps them in performing the programmed task and tactile stimulators that give feedback while interacting with *serious games* in a virtual realty. As well as assisting the patient in carrying out the required tasks,

Figure 1.2: Logos of the completed and ongoing projects at the UNIFI MDM Lab.

the exoskeleton can be exploited to monitor the patient's progress by recording valuable parameters. THE is instead a three-year PNRR project, started in November 2022 and funded by the European Union. Its challenge is to push research toward its application and to companies so that technologies dedicated to health and wellness, such as the wearable devices developed within the MDM Lab, can grow and improve the healthcare system. The exoskeleton is now being evaluated for its introduction into a rehabilitation program at the Neurorehabilitation Department of the University Hospital of Pisa.

## 1.2 State of the art of Hand Exoskeletons

The hand is a highly complex body part consisting of bone, muscles, joints, and ligaments, whose myriad of nerves and innervations provide high sensitivity to the limb [23]. Multiple Degrees Of Freedom (DOFs), together with those of the arm and wrist, determine the hand movement functionality, making it versatile in interacting with its surroundings [24]. The hand can perform prehensile and non-prehensile actions: if the former implies partially or wholly seizing and holding an object, the latter does not involve grasping the object, but perhaps touching it, such as for flipping a light switch [24]. Power and precision grasp fall between prehensile actions, irrespective of pad, palm, or side opposition (e.g., the pen pinching with the thumb and index palmers or tips, the ball grasping, and writing or key pinch, respectively) [25]. All the ADLs can be decomposed into subtasks carried out sequentially to be traced back to specific prehensile and non-prehensile actions [24, 26]. Thus, the loss of motor functions, which can be attributed to traumas (e.g., strokes, spinal cord injury), chronic and genetic conditions (e.g., cerebral palsy), or other neurological disorders affecting the central nervous system, reflects on the ability to perform ADLs, impacting in the person quality of life.

Rehabilitation represents the chance of recovering hand functionality, and more and more studies have been carried out to improve such practice [27], leading to the introduction of robotic technologies in this context [19, 22, 28, 29]. Rehabilitation therapy may involve practising a functional activity by repeatedly performing it (e.g., hand opening and closing) or carrying out power or precision grasps [27, 29, 30]. Moreover, the treatment needs tailoring to the patient's condition: the same training administered to two patients in the same condition can have different outcomes [27, 30]. These therapy issues lead to long treatment sessions and a significant amount of human effort and, therefore, high costs [19, 30]. Given these premises, robot-assisted therapy might represent an attractive solution since it can provide highly repetitive, intensive, adaptive physical training, but also more objective, flexible, and controlled therapeutic paradigms than the conventional one [19, 21, 30]. Indeed, robotic devices allow for providing treatments with improved accuracy and reduced variance, measuring several parameters, among which subjective performances, spasticity, reflexes, and functional movements, tracking the patient status and progress made, and adapting the rehabilitation patterns, without the need to supervise them constantly [21, 30]. This aspect allows the therapist to perform multiple tasks and, eventually, follow various patients simultaneously, and this necessarily implies a reduction in the treatment cost [19, 21, 30], making it affordable to more people in need. These devices may also be combined with other technologies, such as virtual reality and haptic stimuli, to make the exercise engaging and motivate the patient [21, 30].

Rehabilitation devices can be mainly categorised into exoskeletons and end-effector robots [21, 28, 31, 32, 33], two examples of which are shown in Figure 1.3. The latter consists of the distal part of a robotic system enabling it to interact with the environment, which does not act in parallel with the hand but usually on the distal phalanx of each finger, forcing the other segments to move (e.g., [34, 35, 36, 37] or the already commercial available *Amadeo* from tyromotion [8]). On the contrary, exoskeletons (e.g., [38, 39, 40, 41, 42, 43, 44, 45, 46, 47],

[8]https://tyromotion.com/en/products/amadeo/ (accessed January 31, 2024)

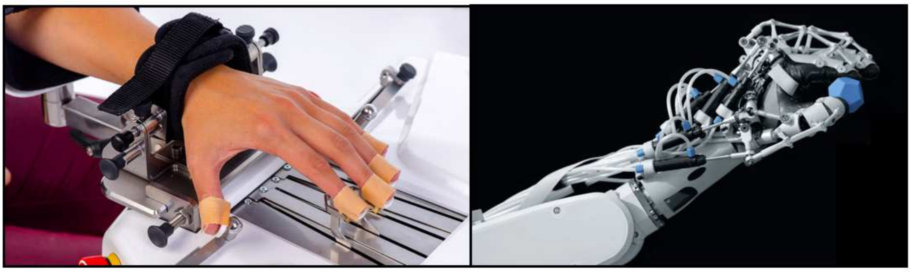

Figure 1.3: *Amadeo* by tyromotion, an end-effector robot, on the left, *ExoHand* by Festo, an exoskeleton robot, on the right.

or the commercial *Gloreha* from Idrogenet, *ExoHand* from Festo [9]) involve a mechatronic structure combined with a control strategy, which is worn by the user on the hand and can support each finger joint movements, depending on the mechanical design. They must comply with the user movements and provide the power required to perform them. Despite promising results, the outcomes of robot-assisted rehabilitation do not always match patients' expectations, and, in general, evidence that they are better or comparable to those obtained through conventional therapy is still lacking as the patient itself, its recovery stage, the device used, and treatment intensity and duration may influence the outcomes; more studies with larger participant sample are needed [21, 30].

Designed for daily life rather than for specific therapy sessions, robotic assistance devices are wearable exoskeletons that have the primary purpose of supporting the user in performing ADLs [48, 49, 50, 51, 52, 53, 54, 55, 56, 57, 58]. Besides, hand robotic devices can also be exploited for haptics, to give feedback in virtual or teleoperation applications [59, 60, 61], and for augmentation, thus to amplify the user's power [62], in different contexts than the healthcare one as well [20, 63].

Focusing on exoskeletons for rehabilitation and assistance, representing the main topic of this work, they mainly differ on the purpose for which they are developed that, in turn, drive the design process, even if both should be easily wearable and not cause discomfort or pain to the user [20, 64, 65]. If the former should apply high output forces and monitor the user performance, the latter must be lightweight, force effective, correctly coupled with the hand to avoid

[9] https://www.festo.com/it/it/e/informazioni-su-festo/ricerca-e-sviluppo/bionic-learning-network/highlights-2010-2012/exohand-id_33631/ (accessed January 31, 2024)

wrong and painful poses, and necessarily requires portability to assist the user in their ADLs as long as possible, based on the device battery life. On the contrary, this aspect is not critical for rehabilitation devices that can instead be directly connected to power. However, they share that customisation and low-cost are challenging features to pursue in the same device, or rather typically at the antipodes, also due to the high complexity of the target body part.

To date, not all exoskeletons have a clear distinction in terms of purpose since robotic devices make it possible to move therapy to different environments, for instance, at home, increasing the patient involvement [21, 32, 40, 66, 67, 68, 69]. At the same time, assistive devices can also be exploited for training sessions in non-clinical settings [41, 70, 71, 72, 73, 74, 75, 76, 77, 78, 79].

The assistive one is the device's purpose developed during the research activity presented in this thesis. However, the requirements it should pursue are more stringent than those for rehabilitation, and compliance with them also does not preclude the device use for rehabilitation purposes.

First, an in-depth literature analysis allowed for defining the primary design requirements for a hand exoskeleton with assistive aims. Boser *et al.* [80] conducted an explorative interview involving six clinicians and eight people with hand impairments to define specific design criteria for assistive hand exoskeletons. Based on end-users expectations, the study revealed that these devices should assist independent and coupled movements of all the fingers, including the thumb, support the user in a variety of grasp patterns related to ADLs, should allow for the wrist motion, exert forces to lift at least a drink, and involve intuitive control strategies rather than simple solutions (e.g., using a button). End-users would exploit hand exoskeletons as long as possible, considering their battery life and comfort; to this aim, their overall dimensions and mass should be kept contained. Despite the small participants sample employed in this preliminary study, the results obtained are in agreement with other studies in the literature [20, 63, 64, 65, 81]. In particular, the main design requirements for assistive hand exoskeletons that emerged from this starting research can be summarised as follows:

1. *Wearability and portability:* the overall dimensions and mass of the hand exoskeleton should allow for completely wearing it, without any components remotely placed from the hand [65], so to ensure its complete portability [63] and not prevent the user mobility;

2. *Safety and comfort:* hand exoskeletons must ensure patient safety and comfort over prolonged use [20]. Customised devices are preferred, even if also adaptable systems to different users can be considered to keep the cost

contained. The actuation and control systems must ensure natural fingers' movements; in particular, the hand exoskeleton must be correctly coupled with the hand and its mechanisms aligned with the fingers to avoid wrong or excessive movements that may cause pain to the user. The hand's high mobility makes determining a safe and comfortable interaction with the exoskeleton challenging. The difficulty increases in the case of an impaired hand.

3. *Lightness and small sizes:* they are crucial requirements for assistive hand exoskeletons, on which those already listed depend. Hand exoskeletons should not exceed the limb dimensions, thus the critical issue increases for pediatric devices. Regarding the mass, the literature considers manageable about 200 g on the hand back and 500 g on the forearm [80];

4. *Dexterity:* the hand exoskeleton dexterity can be related to the reproducible different gestures, among which irregular-shaped objects grasping since it depends on the number of independent finger mechanisms [82], and the DOFs of each. Also, implementing a thumb mechanism that provides opposition and bidirectional movements improves dexterity [81];

5. *Efficacy in ADLs*: the hand exoskeleton's primary purpose is to assist in ADLs or eventually to perform at-home rehabilitation. Therefore, it should be able to exert suitable forces for typical everyday life activities, such as eating, bathing, and drinking; experimental research detected in the literature enabled to fix the target force at 15 N per finger [83, 84]. In the ideal case in which the object weight is equally distributed over the fingers, and considering an average friction coefficient of 0.3 for ordinary objects of daily living (e.g., a ceramic mug, plastic bottle, wooden hair brush, metal scissors), the target amount of force per finger shall make it possible to lift objects weighing up to 2.3 kg, which is a slightly higher value than the average of daily objects [85];

6. *Sense-of-touch preservation*: the device should not foreclose the touching objects and leave the hand palm as free as possible to preserve the natural sense of touch for the fundamental feedback tactile sensations; besides, if the mechanism occupies the palm, objects grasping and full hand closure are prevented [63];

7. *Intuitiveness:* the device should be provided with an intuitive control strategy for easy operation, not complicated, for instance, by the need to control it through the other hand, as in the case of buttons [80];

8. *Affordability:* Adoption of hand exoskeletons is usually prevented by the cost of these technologies, which is still too high due to being a relatively new area of research [20]. The cost is influenced by materials, manufacturing processes, actuators, control systems, customisability, and other factors [65]. Only a cost-effective design can increase its dissemination so that more and more people can benefit from robotic-based assistance [19].

As well as the purpose for which they are developed [20, 32, 63, 64, 65, 86], more designing aspects can distinguish hand exoskeletons.

The hand exoskeleton mobility varies according to the assisted fingers, DOFs of each one, and if coupled or independent finger movements are implemented [29, 64, 82], thus influencing the various delicate grasping tasks in ADLs. Multi-finger exoskeletons can be designed to control each finger individually or couple some finger movements. Exoskeletons require at least three fingers to assist most ADLs [64]; however, those that control four or five fingers independently [48, 56, 58, 66, 67] can be used for the most applications than those with coupled-movement fingers [51, 52, 72, 73, 74], which are limited to specific tasks (e.g., key pinch or precision grasps) [64, 82]. In addition, most ADLs can be performed through devices whose finger mechanisms are provided at least with 2 DOFs [64], even if the optimal number of DOFs has not yet been derived [87]. In general, increasing the number of assisted fingers or their DOFs complicates the device design and control but improves its *dexterity* in grasping motions [87]. The number of interactions between the exoskeleton and hand may change in diverse devices [64]: they can have a single interaction point with each finger in case of single-phalanx mechanisms [36, 35, 56, 88], or more than one, for multi-phalanx configurations [41, 48, 57, 66, 67, 74]. Exoskeletons with multiple interactions suffer from more complex design (influencing *wearability* and *comfort*) than those with a single interaction but improve grasping stability and *dexterity* [64].

Besides, hand exoskeletons may differ according to the strategies for the mechanism placement on the hand and fingers [64], which can involve the hand back, as most solutions detectable in the literature, the palm [35], thus preventing the *sense-of-touch preservation*, or finger sides [43, 68, 89, 90], which might suffer from possible collision in case of multi-finger devices, especially if abduction/adduction (a/a) movement is allowed [64].

From a mechanical point of view, hand exoskeletons can be distinguished mainly based on the actuation system and mechanism architecture. Regarding the mechanism, rigid and soft architectures are mainly exploited [20, 64, 86]. The former consists of mechanical structures made of rigid material, such as metal or plastic (e.g., linkage-based mechanisms [38, 41, 44, 45, 48, 54, 56, 59, 66, 67, 68, 70, 71, 74, 77, 79, 88, 91]), which transmit force and torque to the finger joints, ensuring kinematic accuracy. However, they can suffer from misalignment issues with the finger, affecting the device *safety* and *comfort*. Thus, these mechanisms must be correctly aligned with the finger to prevent wrong and painful motions to the user [20, 63]. In the literature, different alignment methods can be detected [20, 63]. Exoskeletons involving the finger sides whose joints coincide with those of the mechanism ensure the straightforward alignment of the matching axes. Still, lateral finger encumbrance may be limiting for multiple finger systems [43, 68, 89, 90]. Some devices introduce Remote Center of Motion (RCM) mechanisms, meaning that the mechanism can rotate around a point distal to the mechanism itself [92], which can be implemented, for instance, through circular-prismatic-joint [38, 70, 74, 77], parallelogram-based [91, 93], double-parallelogram-based [67, 94, 95] architectures. Hand exoskeletons may also present redundant linkages, such as four-bar mechanisms, which attach to the finger before and after each actuated joint with additional linkages and joints between them [41, 48, 96, 97], or base-to-distal linkages [54, 56, 59, 60, 88] that have only one contact point between the mechanism and finger (usually, on the proximal or distal phalanx). Compliant systems are instead peculiar of soft architectures [20, 63], which do not require alignment. Such devices, indeed, may consist of cable-driven gloves [50, 51, 53, 75], and fibre-reinforced [69, 72], polymer-or-elastomer-based [78, 98], fabric-based [49, 58] solutions, which promote *lightness* and *small sizes*, and increase compliance, and *comfort* [52, 99]. Nevertheless, they are helpful only for low assistance levels due to the forces they can exert. *Force effectiveness* and accuracy are crucial features of rigid architectures, which, instead, usually turn out to be cumbersome systems that can prevent in-confined-spaces motions or fine manipulation. First hybrid solutions, including rigid and soft elements in their mechanical structure, have been studied, aiming to catch the strengths of both [51, 52, 69, 73, 86].

Hand exoskeletons can also be distinguished according to the actuation system exploited [20, 32, 63, 64, 65, 86], which consists of the actuator type and transmission system, enabling to transmit motion from the actuator to the finger mechanism. For what concerns the type of actuators, pneumatic, hydraulic, and electric motors are the most detected in the literature, even if also other technologies are lately frequent in this field (e.g., shape memory alloy actuators) [65, 100]. Pneumatic actuators use gas as a means of power transmission, while hydraulic ones exploit liquids. Such systems are the most employed in soft wearable devices [101], especially with polymer-or-fabric-based and fibre-reinforced structures, such as artificial muscles, bending, or cylinder actuators [65], which can provide the device with high compliance, power, and force. Indeed, the force effectiveness of soft architectures may be improved by combining them with pneumatic and even more with hydraulic actuators. Nonetheless, they require multiple components for their functioning, among which a compressor or a pump, valves, separate chambers, tubes, and water reservoir in case of hydraulic systems, in addition to the control electronics and battery pack, which increase the device's overall dimensions and mass [20, 32, 101]. As a result, the actuation and control units must be necessarily dislocated to other body parts, thus limiting the user's mobility. Besides, possible leakages determine limited use in a not-so-large niche of applications as they may compromise the device's *safety*. However, most devices for wearable applications exploit electric motors for actuation [20, 64, 65] due to their ease of use, control, *safety*, backdrivability, reliability, and *cost*. Several models of as many weights, sizes, and power outputs are available on the market, providing many different alternatives for each application. Also, the transmission system can vary in hand exoskeletons [32, 63, 64]. Rigid solutions, among which direct drive, gears, or linkages, are usually combined with electric motors [41, 68, 74] and can transfer forces with kinematic accuracy and without loss, despite cost implications [32, 100]. Rigid transmission is often synonymous with placing actuators near the finger-handling mechanism, thus on the hand back, usually enabling the device *portability*, even if the device mass on the hand increases [63]. Flexible methods, such as cable transmissions, are exploited to transmit motion both to soft architectures (acting as tendons) [53, 75] and rigid ones [54]. One of the most frequent solutions in the literature combines electric motors placed away from the hand and Bowden cables for transmission [100]. Hand exoskeletons benefit from their compliance and lightness that ensure comfort but, as tendon-driven devices, suffer from control and loss issues and non-linear tension variation due to friction and backslash [32, 63]. In addition, cable-driven exoskeletons allow for unidirectional movements, meaning that a single task (e.g., flexion or extension) can be performed by exploiting only one cable [20, 63]. At least another cable, or specific cable configurations (e.g., pull-pull or push-pull configurations), enable bidirectional motions while increasing the device's overall dimensions and complexity and reducing *wearability* and *portability* [100, 102]. The actuation system can thus influence the device *portability*, which can be pursued by concentrating the device components as much as possible on the assisted limb and avoiding displacing them to other body parts (e.g., in a waist belt [72], in the back [52], in the chest [73]), thus preventing the user freedom of motion.

Finally, hand exoskeletons differ in the control system, from which the device *intuitiveness*, consisting in the way of detecting the user intention [20, 63],

| Ref. | Indep. finger movement | Transmission system | Actuator | Mechanism architecture | Forces [N] | Mass [g] | Alignment | Remote location |
|---|---|---|---|---|---|---|---|---|
| [41] | T, I-M-R-S | Linkage mechanism (active O/C) | Electric (Linear motors) | Linkage mechanism (R) | 9 (Grasp) | / 183 | Yes | - |
| [48] | T, I, M | Bowden cables (active O/C) | Electric | Linkage mechanism (R) | - | 205/ - | Yes (4-bar mechanism) | Yes |
| [49] | T-I-M-R-S | Pneumatic (active O/C) | Pneumatic | Fabric-based glove (S) | 15 (Grasp) | 77/ 5000 | Yes (Auto) | Yes |
| [51] | T, I, M-R-S | Bowden cables (active O/C) | Electric (7 DC motors) | Rigid elements, glove (H) | 16.6 (Grasp) | 220/ 16000 | Yes (Auto) | Yes |
| [52] | T, I-M-R-S | Bowden cables (active O/C) | Electric (2 DC motors) | Three-layered springs, rigid elements (H) | | 259/ 560 | Yes (Auto) | Yes |
| [53] | T, I, M, R | Cables (active O/C) | Electric (4 DC motors) | Glove (S) | 16 (Pinch) | 250/ 340 | Yes (Auto) | No |
| [54] | I-M-R-S | Cables (active O) | Electric (1 DC motor) | Linkage mechanism (R) | | 460/ 540 | Yes (Base to distal) | No |
| [56] | T, I, M, R, S | Cables and torsion springs (active O/C) | Electric (6 servomotors) | Linkage mechanism (R) | 10.8 (Pinch) | 235/ 1400 | Yes (Base to distal) | Yes (waist) |
| [58] | T, I, M, R, S | Pneumatic (active O/C) | Pneumatic | Fabric based (S) | 88 (Grasp) | 137/ 971 | Yes (Auto) | Yes |
| [67] | T, I, M, R, S | Linkage mechanism (active O/C) | Electric (5 linear motors) | Linkage mechanism (R) | - | 340/ 340 | Yes (Double-parallelogram mechanism) | No |
| [69] | T, I, M, R, S | Pneumatic (active O/C) | Pneumatic | Fiber-reinforced elastomeric chambers and rigid element (H) | 19.5 (Grasp) | 100/ 2600 | Yes (Auto) | Yes |
| [72] | T-I-M-R-S | Hydraulic (active O/C) | Hydraulic | Fiber-reinforced elastomeric chambers (S) | 8 | 285/ 3300 | Yes (Auto) | Yes (waist) |
| [73] | T, I, M, R-S | Bowden cables (active O/C) | Electric (4 linear motors) | Rigid sheath guides elastomeric chambers (S) | 5 | 50/ 3300 | Yes (Auto) | Yes (chest) |
| [74] | T, I-M-R-S | Linkage mechanism (active O/c) | Electric (2 DC motors) | Linkage mechanism (R) | - | 420/ 420 | Yes (Circular-prismatic joint) | No |
| [75] | T-I-M-R-S | Cables (active O/C) | Electric (2 linear motors) | Glove (S) | - | 377/ 377 | Yes (Auto) | No |
| [79] | I-M-R-S | Gears and (active O/C) | Electric (1 servomotor) | Linkage mechanism (R) | 94 (Grasp) | 380/ 500 | No | No |
| [98] | T, I, M-R-S | Cables (active O/C) | Electric (4 linear motors) | Rigid elements (R) | 10 (Thumb fingertip) | 200/ | Yes (Auto) | Yes |
| [103] | T, I, M, R, S | Pneumatic (active O/C) | Pneumatic | Polymer based (S) | 18 (Grasp) | - | Yes (Auto) | - |
| [104] | T, I, M, R, S | Pneumatic (active O/C) | Pneumatic | Elastomer and fabric based (S) | 4 (Grasp) | 200/ | Yes (Auto) | Yes |

Table 1.1: Main features of state-of-the-art devices for assistance or at-home rehabilitation.

e.g., trigger ([49, 52]), force ([68, 97]), or biosignal ([41, 43, 51, 54, 67, 75, 79]) methods, derives. Therefore, sensors providing position, force, and biosignals feedback to the control strategy can also differ among the devices in the literature [20, 63, 64, 65].

According to the hand exoskeletons characterization, Table 1.1 summarizes some features of the leading current state-of-the-art assistive and portable-rehabilitation devices that most influence the assistive requirements achievement, and thus that are of interest for the focus of the discussion proposed in this study. For each reference, independent finger movement, transmission system, actuator type, mechanism architecture, measured force, mass, alignment, and remote location information are reported. Specifically, under the "Independent finger movement" column, thumb, index, middle, ring, and small are denoted with the matching initial letters (T, I, M, R, and S, respectively). A comma separates letters if that finger movement is independent of the others and by the symbol (-) if the fingers are coupled. The matching column indicates the transmission system in which active movements (O=Opening, C=Closing) are highlighted in brackets. The "Actuator" column includes the number and specific type of actuators if reported in the article. In the "Mechanism architecture" column, the type of architecture (R= Rigid, S=Soft, H=Hybrid) is specified in brackets. Forces measured during experimental sessions are reported in the corresponding column, in which the specific task that allowed for that measurement is highlighted if mentioned in the article cited. The device mass on the hand and total are separated by the symbol (/) in the "Mass" column. If reported in the article cited, the alignment method and remote location are specified in brackets in the matching columns. The symbol (-) is instead used in case of lack of information.

Despite the alternatives existing in the literature, it is challenging to identify hand exoskeletons that simultaneously meet all the requirements mentioned above [20, 63, 64, 65, 80, 81]. Table 1.1 shows the prevalence of electric actuators in the current state of the art. Among them, DC and servomotors are the most exploited [51, 52, 53, 54, 56, 74, 79], even if also examples of linear motor applications are reported [41, 67, 73, 75, 98]. However, linear motors usually determine an increase in *overall sizes* that is not reflected in their *force effectiveness.* Electric motors are those actuators that can most easily placed on the hand rather than in remote locations, especially if coupled with rigid transmission [41, 67, 74, 79], thanks to the wide variety commercially available that enables to detect the best trade-off between dimensions, mass, performance, and cost. However, it is frequent to find electric motors also placed away from the hand when accompanied by Bowden cables for transmission [48, 51, 52, 73]. Remotely placing some components is of crucial relevance in the case of pneumatic [49, 58, 69, 103, 104] and hydraulic [72] actuators, which require heavy components for their functioning that could not be placed only on the hand. As the table shows, this solution keeps contained the *mass* on the hand, improving the device *comfort* (e.g., [48, 49, 51, 52, 56, 58, 69, 72, 73, 98, 104]), but worsens its *wearability* and *portability*, limiting the user mobility. Excessive *overall sizes* of the finger-handling mechanism on the hand, usually due to bulky rigid architectures, can also be significantly limiting for fine manipulation or in-confined-space movements. Referring to the table, rigid linkage architectures [54, 56, 67, 74, 79] may imply higher *mass* on the hand, but also more *effectiveness* in force transmission rather than soft ones. For those devices that avoid remote placing some components, the mass on the hand is mainly due to the number of actuators from which the DOFs per finger and independent finger derive [41, 53, 67], in addition to the control electronics, power supply system [54, 74, 75], and mechanism architecture [74, 79]. Exceptions are those devices that exploit cables to transmit motion to rigid elements fixed on a glove for actuating the phalanges [51, 73, 98], which are characterised by reduced mass on the hand but still lower exerted forces than rigid finger-handling mechanism, especially if coupled with gear transmission [79]. High forces and low masses on the hand are also achieved in [58], in which pneumatic actuators are implemented to increase the forces soft architecture can exert. However, they necessarily imply the remote placement of some components required by these actuators' mass, overall sizes, and safety.

## 1.3 Contribution and thesis structure

The research activity conducted during the Ph.D. period focused on developing a new hand exoskeleton for assisting users with hand disabilities in ADLs and enabling rehabilitation training in non-clinical environments, e.g., at home. The new hand exoskeleton has been designed in accordance with the primary requirements detected in the literature for assistive devices, i.e., wearability, portability, safety, comfort, lightness, small overall sizes, force effectiveness, dexterity, sense-of-touch preservation, intuitiveness, and affordability. The design was preceded by in-depth and critical literature research to identify the strengths and weaknesses of the leading current state-of-the-art solutions, revealing the lack of devices that meet all these requirements. If, on one side, remotely placed components may reduce the mass and overall sizes above the hand, on the other, they limit the user mobility, thus preventing the device's wearability and portability. Remote placing can be avoided by keeping low dimensions and mass of the mechanism architecture, actuation system, and electronic components, as long as the force effectiveness for ADLs is still ensured. Therefore, the literature research led to designing a novel finger-handling mechanism with a hybrid architecture, meaning that rigid and soft components are involved, which can be easily adapted to all fingers. Such a solution stems from the need to keep the overall dimensions above the finger contained, not to prevent movements in confined spaces and fine manipulation while exerting suitable forces for ADLs. To this aim, the rigid architecture was designed to act on the proximal phalanx, while the flexion/extension (f/e) of the distal phalanx is delegated to the soft architecture that enables improving finger dexterity by introducing a multi-phalanx configuration. The promising results obtained from the first finger-handling mechanism paved the way for developing a completely wearable and portable hand exoskeleton, shown in Figure 1.4. The device involves two main modules: the one placed on the hand back includes the finger-handling

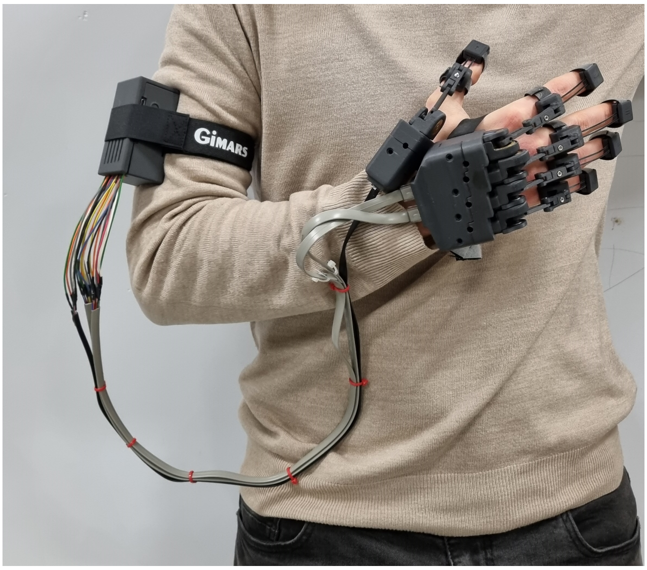


Figure 1.4: The assistive hand exoskeleton developed during the Ph.D. period.

mechanisms and actuation system, while the one fixed to the upper limb encloses the electronic components and power supply. Reachable Range Of Motion (ROM) and exerted forces were evaluated in the finger module and then in the whole device, achieving the prefixed aim of developing a hand exoskeleton that meets the design requirements for assistive devices detected in the literature. Finally, preliminary tests were conducted on healthy subjects to measure the device's performance and functionality.

The research presented in this thesis is organised as follows: Chapter 2 presents the background of the MDM Lab on wearable devices. The results of the Action Research Arm Test (ARAT) conducted in the first phase of the Ph.D. period with the last developed device are reported since they are a fundamental starting point for conceptualising the renewed hand exoskeleton, summarised at the end of this chapter. The mechatronic design of the finger-handling mechanism and the whole device is reported in Chapter 3, in which, firstly, the hybrid architecture is deeply explored, and then the hand exoskeleton embodiment is presented. Chapter 4 presents tests on ROM and force effectiveness, performed on the first finger module prototype, and then the grasping and pinching force tests extended to the whole device. The results achieved are then reported and discussed. Chapter 5 introduces the model developed in Simscape/Simulink to simulate the behaviour of the soft component within the hybrid architecture, and findings from preliminary simulations are reported. Finally, conclusions will be drawn in Chapter 6.

# Chapter 2

# MDM Lab background

The activity research (November 2020 - January 2024) presented in this thesis has been conducted within the MDM Lab of the UNIFI DIEF, which has been working on Wearable Robotics since 2013 and over the years studied and developed more and more devices, especially for hand assistance and rehabilitation.

This chapter will walk through the main assistive solutions developed over time with a twofold aim of highlighting the key points of the study that are still considered in the current design phase (such as the kinematic optimisation process, helpful for tailoring the finger-handling mechanisms on the user's hand), and the main challenges that led to defining the device presented in this thesis. The results achieved with the last prototype developed by conducting an ARAT are also reported since they paved the way for the renewed design of the hand exoskeleton for assistance proposed in this work. A description of the hand anatomy will precede this overview to introduce helpful terminology for the subsequent discussion.

## 2.1 Hand anatomy

Allowing as much full motion as possible is the first evident and fundamental requirement of any hand device. For this reason, during the design phase, knowing each finger joint trajectory is of paramount importance.

The hand anatomy is very complex, inevitably implying equally complex kinematics. Fingers count 14 bones, i.e., phalanges: two in the thumb and three in the other fingers. Phalanges, shown in Figure 2.1, are named, starting from

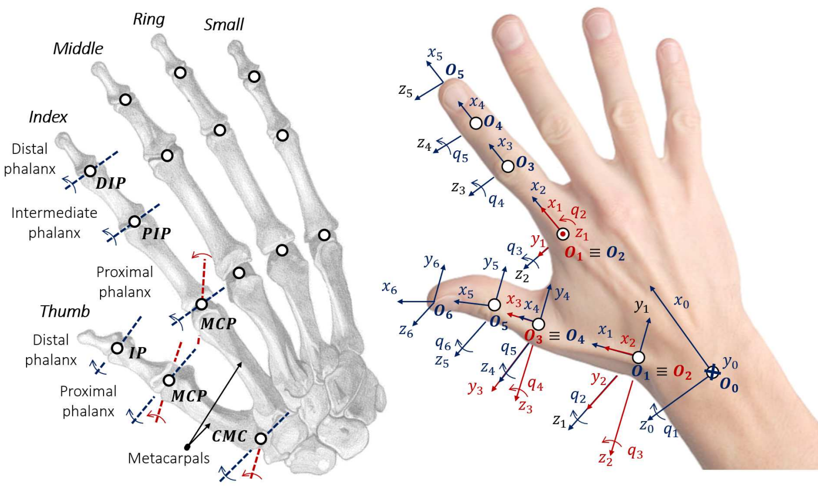


Figure 2.1: On the left, the hand anatomy. On the right, the modified D-H model of the thumb and index exploited in this study. Red and blue axes (both dashed and solid) represent, respectively, a/a and f/e motions.

the palm, respectively, as “proximal,” “intermediate,” and “distal”; the thumb lacks the intermediate one. Also, adding the thumb metacarpal, there are 15 mobile bones globally. Figure 2.1 shows the joints enabling these bones to move: (i) the CarpoMetaCarpal (CMC) between the carpal bone and metacarpal, (ii) the MetaCarpoPhalangeal (MCP) between the metacarpal and proximal phalanx, (iii) the Proximal InterPhalangeal (PIP) joint between the proximal and intermediate phalanges, (iv) the Distal InterPhalangeal (DIP) joint between the intermediate and distal phalanges. CMC joints are almost entirely fixed except for the thumb one that guarantees the so-called circumduction and opposition movements. MCP joints enable f/e and a/a movements. DIP and PIP joints, which in the thumb are “merged” in the Proximal Interphalangeal (IP) joint, have just one Degree Of Freedom (DOF), allowing their f/e motion.

Joint trajectories can generally be identified experimentally or by hand kinematic models. In the former, a Motion Capture (MoCap) system may be exploited to track the position of markers placed in each finger joint during its f/e (or hand opening/closing), as done in [105]. The latter, on the other side, is also applied in this thesis work and involves considering kinematic hand models found in the literature. It is worth noting that a specific thumb characteri-

| | Thumb | | | | | | Index | | | | |
|---|---|---|---|---|---|---|---|---|---|---|---|
| Joint $\rightarrow$ | 1 | 2 | 3 | 4 | 5 | 6 | 1 | 2 | 3 | 4 | 5 |
| $\theta_j$ (°) | $q_1 + \beta$ | $q_2 + \delta$ | $q_3$ | $q_4$ | $q_5$ | $q_6$ | $q_1$ | $q_2$ | $q_3$ | $q_4$ | $q_5$ |
| $\alpha_j$ (°) | $\epsilon$ | 90 | 0 | -90 | 0 | 0 | 90 | -90 | 0 | 0 | 0 |
| $a_j$ (mm) | $l_c \cos\gamma_t$ | 0 | $l_m$ | 0 | $l_p$ | $l_d$ | $l_m \cos\gamma_i$ | 0 | $l_p$ | $l_i$ | $l_d$ |
| $d_j$ (mm) | $l_c \sin\gamma_t$ | 0 | 0 | 0 | 0 | 0 | $l_m \sin\gamma_i$ | 0 | 0 | 0 | 0 |

Table 2.1: D-H parameters $(\theta, \alpha, a, d)$ for the thumb and index fingers.

sation [106] was also considered to define some useful parameters in solving thumb kinematics. According to the hand kinematic model considered in this study [107], fingers are modelled as rigid kinematic chains whose joints and links correspond to hand joints and bones. The Denavit-Hartenberg (D-H) method was applied to each finger kinematic chain to determine its joint position and orientation, namely its pose. D-H parameters and each joint admissible ROM, determined by maximum and minimum achievable f/e angles, are acquired after fixing a reference frame on the wrist and different coordinate systems on each finger joint, as shown in Figure 2.1. Five coordinate systems are placed for the thumb (two in the CMC joint, two in the MCP joint, and one in the IP joint), and four (two in the MCP joint, one in the PIP joint, and one in the DIP one) for each of the other fingers. In addition to those of the thumb, Figure 2.1 shows only the coordinate systems of the index finger as representative of the analogous cases of the middle, ring, and small fingers. From now on, the discussion will refer to the thumb and index fingers for clarity. The reference system $O_j x_j y_j z_j$, where $j = 0, 1, ..., 5$ for the thumb and $j = 0, 1, ..., 4$ for the index, is associated to joint $j+1$, while $O_6 x_6 y_6 z_6$ and $O_5 x_5 y_5 z_5$ are integral with their fingertips, respectively. Table 2.1 lists the D-H parameters of the model for the thumb and index. Specifically: $q_j$ is the angular coordinate of the $j$-th joint; $\beta$, $\epsilon$, and $\delta$ are fixed thumb anthropometric parameters, among which $\beta$ is the initial orientation of the thumb carpometacarpal segment to the palm plane, $\epsilon$ describes the orientation of the reference frame centred in the CMC joint to that in the wrist, while $\delta$ is a user-specific value since it depends on the finger bones' length; $\gamma_t$ is the angle between the thumb carpal bone and $x_0$; $l_c, l_m, l_p, l_i, l_d$ are the length of the thumb carpal bone, metacarpal, proximal, intermediate, and distal phalanges, respectively. According to [106, 107], for the thumb study, $\beta$ and $\epsilon$ have been set equal to 35° and -135°, respectively. $q_1$, $q_2$, $q_3$, and $q_4$ are set equal to 0° as the wrist and CMC joints are considered fixed, while the MCP a/a is neglected as the finger mechanism will only actuate the f/e motion.

| | Thumb | | Index | | |
|---|---|---|---|---|---|
| Joint | $\theta_{MCP}$ | $\theta_{IP}$ | $\theta_{MCP}$ | $\theta_{PIP}$ | $\theta_{DIP}$ |
| Maximum extension | $-10°$ | $-20°$ | $-20°$ | $0°$ | $-5°$ |
| Maximum flexion | $60°$ | $90°$ | $90°$ | $100°$ | $60°$ |

Table 2.2: The maximum ROM achievable for the thumb and index fingers, according to the kinematic model considered in this study [107].

$q_5$ and $q_6$, which will subsequently be referred to as $\theta_{MCP}$ and $\theta_{IP}$, can vary between the maximum extension and flexion angles of the proximal and distal phalanges around the MCP and IP joints, respectively, as specified in Table 2.2.

Considering that, as for the thumb, the other finger mechanisms will only actuate f/e motion, $q_1$ and $q_2$ are set to 0° since the wrist f/e and MCP a/a are not actuated. $q_3$, $q_4$, $q_5$, corresponding to $\theta_{MCP}$, $\theta_{PIP}$, and $\theta_{DIP}$ for the other fingers, are the angular coordinates of the MCP, PIP, and DIP joints, which describe the proximal, intermediate, and distal phalanges f/e, respectively. Their ranges are reported in Table 2.2.

## 2.2 MDM Lab hand exoskeletons evolution

The research activity of the MDM Lab has always aimed to develop an easily wearable, small, lightweight, safe, and low-cost robotic device for users with impaired hands. The first prototype the research group developed is shown on the left of Figure 2.2. The device was designed to validate the kinematic model

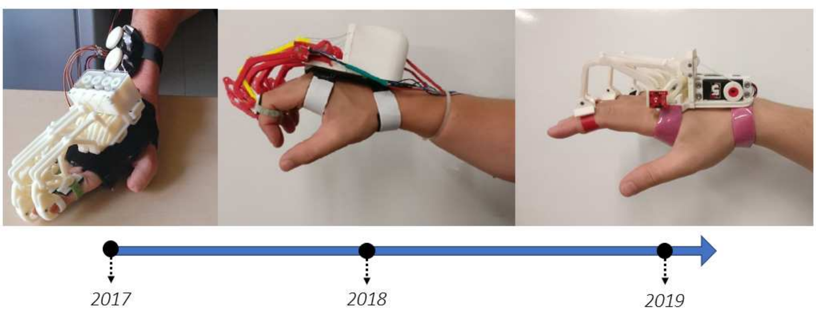


Figure 2.2: Assistive hand exoskeletons evolution in the MDM Lab.

proposed in [96] and according to the need of a patient suffering from SMA since birth, i.e., assistance in ADLs by supporting the hand opening rather than its closing. Indeed, the disease had caused such retraction of the tendons that the hand was forced into a closed position, no longer allowing the patient to open it independently. This hand exoskeleton included the finger-handling mechanisms for all the fingers except for the thumb, for which the patient still presented good mobility, four servomotors (one per finger) to actively open the fingers at the same time by pulling cables while releasing them the closing gesture was passively allowed, and two buttons to control the fingers opening and closing. No independent finger movements were considered for simplicity. A 4-cell Lithium battery powered the whole system. The introduction of a thimble for the distal phalanx to increase stability, representing a second connection point between the mechanism and finger, did not influence the main 1-DOF kinematic chain, whose end-effector was placed on the intermediate phalanx. The mechanism design was user-centred since an optimisation MATLAB-based algorithm was exploited to fit its kinematics to the 2D trajectories of the index finger of the specific user acquired through video recording and extrapolated by using the open source software Kinovea [108].

The overall architecture key points have not changed in subsequent prototypes: it remained based on single-phalanx, single-DOF, rigid, and cable-driven finger-handling mechanism, acting on all the finger except for the thumb [108]. As shown in Figure 2.2, the prototype on the centre did not include the thimble wrapping the fingertip, thus avoiding the uncomfortable feeling of constraint to a rigid system perceived with the previous architecture, while a passive DOF was added to allow for the a/a movement, improving the compliance between the finger and mechanism. The one on the right instead has been further simplified by eliminating another component. The mechanism components were designed to be 3D printed in Acrylonitrile Butadiene Styrene (ABS) and withstand forces up to 15 N, a reasonable value for typical manipulation tasks of ADLs. The number of actuators was reduced first to two and then to one to improve the overall sizes and mass of the system. If in the former, one servomotor actuated the index and the other guided the f/e of the middle, ring, and small, the latter exploited only one motor to move the fingers. These prototypes included, respectively, two and one encoders for the finger position control in accordance with the number of motors.

In developing the second prototype, a kinematic optimisation procedure based on the Nelder-Mead algorithm was introduced as a straightforward method to tailor the device to each new user [105]. Specifically, the procedure allowed for comparing two trajectories — the so-called *desired* and *actual* trajectories

— and deriving those component sizes that minimise the error between them. To clarify what has just been said, the *desired* trajectory is that of the contact point between the finger and exoskeleton, evaluated according to the hand kinematic model, while the *actual* one is that of the same point (mechanism end-effector) according to the mechanism kinematics. For the sake of simplicity, these trajectories are converted into polar coordinates to be compared. The component sizes are collected in a vector resulting from the optimisation procedure. This iterative process, indeed, looks for the vector $\mathbf{x} \in S$ — where $S$ is the so-called admissible region — that minimises the objective function $f(\mathbf{x}) \in R$, as formalised below:

$$\begin{gathered} min_{\mathbf{x} \in \mathbf{S}} f(\mathbf{x}) \\ \mathbf{g(x)} < 0 \\ \mathbf{h(x)} = 0 \end{gathered} \tag{2.1}$$

Specifically, $S$ is identified by all the constraints that characterise the mechanism in terms of dimensions, ROM, and geometry expressed as equations $\mathbf{h(x)} = 0$ and inequalities $\mathbf{g(x)} < 0$; the objective function $f(\mathbf{x})$ is, instead, defined as:

$$f(\mathbf{x}) = \alpha \Sigma \frac{\mathbf{e}_i(\theta_i)}{n} + (1 - \alpha) \max \mathbf{e}_i(\theta_i) \tag{2.2}$$

where $\mathbf{e}_i(\theta_i) = |\rho(\theta_i) - \rho^*(\theta_i)|$ represents the absolute value of the error between the *actual*, $\rho(\theta_i)$, and *desired*, $\rho^*(\theta_i)$, radial coordinates evaluated at the same $i$-th angular coordinate $\theta_i$ (Figure 2.3), while $\alpha \in R$ is the weight to emphasise or not the contribution of the mean error versus the maximum one. The procedure consists of firstly evaluating the *desired* trajectory, which for this prototype was caught experimentally by exploiting the MoCap system available at the Don Carlo Gnocchi Foundation Rehabilitation Centre in Florence, i.e., a SMART-DX MoCap optoelectronic system by BTS Bioengineering (BTS Bioengineering S.p.A., Milano, Italy) that allows for tracking the natural motion of the user's fingers. Secondly, the kinematics of the mechanism whose component lengths are initially given by a first attempt vector $\mathbf{x}_0$ was solved to detect the end-effector *actual* trajectory. Then, $f(\mathbf{x})$ is calculated, and its value is memorised. If the current solution violates the constraints defining $S$, a penalty is added to the objective function's final value. For each iteration, a new vector $\widetilde{\mathbf{x}}$ to solve the mechanism kinematics is produced, and the error between the compared trajectories is measured once again. The procedure is repeated for an arbitrary and finite number of times: the vector $\mathbf{x}$ producing the lowest $f(\mathbf{x})$ is a local optimum that guarantees a minimum error between the compared trajectories and, possibly, satisfies all the problem constraints. The resulting vector was

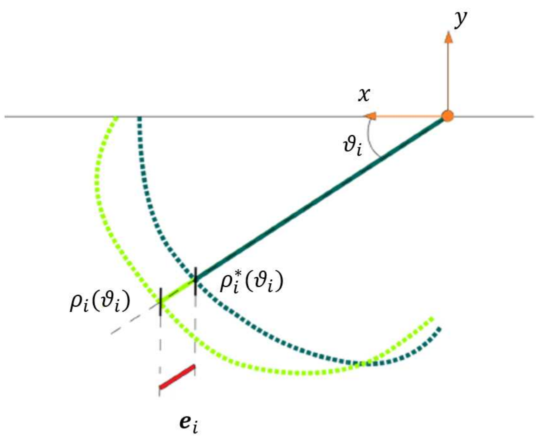


Figure 2.3: Comparison between the radial coordinates of the *actual* (light-green colored) and *desired* (dark-green colored) trajectories evaluated at the same angular coordinate.

properly scaled to detect the component sizes for the other finger mechanisms. Besides, the resulting vector for each finger could be attached to the parametric Computer Aided Design (CAD) model of the components of the matching finger mechanism to update it for the new user quickly.

If this prototype (on the centre in Figure 2.2) was developed focusing on ergonomics and customisability, the next one (on the right in Figure 2.2) saw the introduction of a highly intuitive control strategy. A control architecture based on surface ElectroMyoGraphy (sEMG) was developed to leave the total control of the exoskeleton actuation to the user without being forced to use the other hand to send the command to the device [109, 110]. The single-DOF and single-phalanx finger handling mechanism of this last prototype, which was made less bulky than the previous solutions without influencing the already validated kinematic model [96], allows the complex hand kinematics to be reproduced through a more compact device than others presenting rigid mechanisms in the literature [38, 48, 66]. Constraint feelings are prevented thanks to customisation, made possible by the kinematic optimisation process, and passive a/a movement for all the fingers, leading to an ergonomic and comfortable device, which also helps the fingers to arrange themselves efficiently when grasping an object. The cable transmission enables to perform irregular grasps thanks to its flexibility that allows the fingers to adapt to objects of different shapes, while the single actuator positively impacts the system mass, even though it prevents independent finger movement. The electronic components (i.e., an Arduino Nano controller board, a Bluetooth module, a driver, a magnetic encoder, sEMG sensors) were also chosen for lightness, cheapness, and intuitiveness. For the same purposes, two MyoWare Muscle Sensors (AT-04-001) by Advancer Technologies were exploited to collect electromyography signals from specific forearm muscles, which were flexor digitorum superficialis and extensor digitorum superficialis. Indeed, they can detect, interpret, and measure bioelectric signals from muscle activity. A custom graphical user interface was also developed to collect sEMG signals training datasets and upload the classifier to the micro-controller board on the device.

Although, at this point of the study, the hand exoskeleton is customisable on the patient's hand, compliant with it, and intuitive, some flaws remain. They mainly concern the device's complete portability and wearability, the sEMG sensor cables management and dressing, the connection between the hand and exoskeleton that can cause inconsistency between the device *actual* trajectories and *desired* ones it has been designed for as well as discomfort and the lack of an integrated and wearable power supply system [54]. To overcome these issues, modifications were performed in the fields of the sEMG technology, the interface between the exoskeleton and hand, and overall mechatronic architecture leading to the prototype shown in Figure 2.4 [54]. The overall mechatronic structure was modified to achieve a completely wearable and portable device. Specifically, it was made a modular structure, consisting of a module to be located right above the fingers, including the finger-handling mechanisms, and another module to be fixed on the hand back, housing the actuation and control system and the power supply. One of this prototype's main novelty is the battery relocation in the core module, endowing the device with portability. Besides, the modular structure minimises maintenance downtime: if the module on the hand back might be subjected to limited changes, the one on the fingers requires mechanisms replacement for each new patient or each time its mobility positively or negatively changes. An interface allowing for the rapid and removable connection with the exoskeleton (through the guide and holes for threaded connections visible on it in Figure 2.4) was designed as tailored to the specific user anatomy starting from the scan of a thermoplastic splint modelled by a therapist on the patient. It can then be fixed to the hand through Velcro straps, freeing the touch. It is worth noting that this interface stiffens the wrist articulation, conferring stability to the system, and provides rigid support for the thumb while keeping its proximal phalanx in a semi-opposition state to the palm, thus facilitating ob-

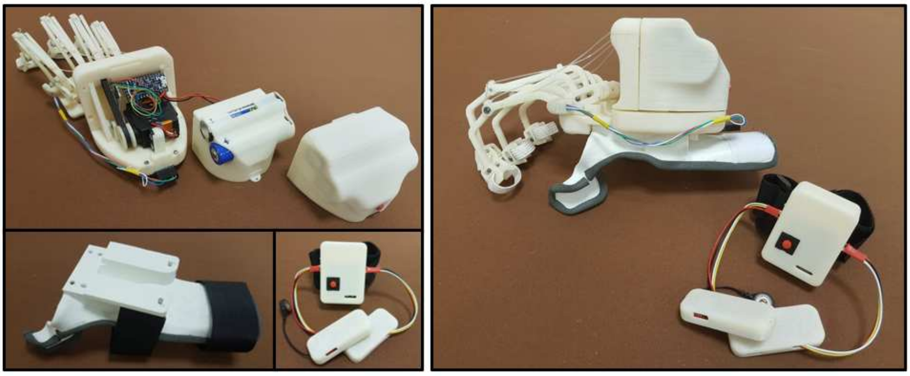

Figure 2.4: The last prototype developed by the MDM Lab research group before the one presented in this thesis: on the left, the three main modules in which modifications are introduced (on the top, the module on the hand back, on the bottom left, the interface between the hand and exoskeleton, on the bottom right, the sEMG bracelet), and on the right, the whole device.

ject grasping by mitigating tendon retraction. Finally, a new bracelet to collect sEMG signals, visible in Figure 2.4, was designed to prevent cable issues and mitigate disturbances. Its central unit includes a single-cell Li-ion battery to be autonomous and independent, and a micro-controller and a Bluetooth module to process sEMG signals, caught by the sensors placed on the secondary units, and send commands to the exoskeleton through the Bluetooth bridge. Due to this control and actuation system, the exoskeleton is suited for all patients who can arbitrarily contract the muscles and can assist only in opening the hand.

## 2.3 Test, results, and new perspectives

This last prototype was experimentally tested in July 2021 on a patient suffering from SMA. The tests were conducted to evaluate the actual effectiveness and functionality of the redesigned hand exoskeleton. Specifically, the tests wanted to show if the exoskeleton might improve the patient independence in ADLs, allowing for more efficient object grasping than without wearing the device, the strengths of the new design, and the remaining flaws. An ARAT, which is an observational test used to determine the upper limb functions, was performed with this purpose [111, 112, 113]. The test consists of asking the subject to

Table 2.3: The ARAT items for each task: the first column shows the four subgroups; the second one lists the task identifier, in which letters indicate the corresponding subgroup (G=Grasp, GR=Grip, P=Pinch, GM=Gross Movement), while numbers show the order of the proposed tasks to the subject; the third column describes the item involved and activity to perform.

| Task subgroups | Tasks identifier | Item and activity |
|---|---|---|
| Grasp | G1 | Block, wood, 10 cm cube (most difficult) |
| | G2 | Block, wood, 2,5 cm cube (easiest) |
| | G3 | Block, wood, 5 cm cube |
| | G4 | Block, wood, 7,5 cm cube |
| | G5 | Ball (Cricket), 7,5 cm diameter |
| | G6 | Stone 10 x 2,5 x 1 cm |
| Grip | GR1 | Pour water from glass to glass (most difficult) |
| | GR2 | Tube 2,25 cm (easiest) |
| | GR3 | Tube 1 x 16 cm |
| | GR4 | Washer (3,5 cm diameter) over bolt |
| Pinch | P1 | Ball bearing, 6 mm, 3rd finger and thumb (most difficult) |
| | P2 | Marble, 1,5 cm, index finger and thumb (easiest) |
| | P3 | Ball bearing 2nd finger and thumb |
| | P4 | Ball bearing 1st finger and thumb |
| | P5 | Marble 3rd finger and thumb |
| | P6 | Marble 2nd finger and thumb |
| Gross movements | GM1 | Place hand behind head |
| | GM2 | Place hand on top of head |
| | GM3 | Hand to mouth |

handle 19 items grouped into four types of subtests: grasp, grip, pinch, and gross arm movement. The test administration lasts approximately 10 minutes and requires considerable non-standard equipment [113], as shown in Table 2.3, in which the items involved in the matching tasks are listed. For each task subgroup, the first and second items are the most difficult and easiest, respectively; then, the difficulty increases with the subsequent items. According to the standard protocol, the patient has to be seated in a chair in front of a table, with the feet on the floor and the head in a neutral position. Each item listed in Table 2.3 has to be grasped and lifted on a 37-cm-high shelf above the table. The patient performance is rated on a 4-point scale ranging from 0, if no movement is possible, to 3, whether the movement is correctly performed. Starting from the first task subgroup, the patient is required to perform the most challenging task, i.e., the first one on the list. If this task is rated with 3, the other items of that subgroup are automatically rated with 3, and the next

Figure 2.5: Some tasks carried out during the ARAT: in order from left to right, (i) the cricket ball grasping (G5) performed without, and (ii) with the hand exoskeleton, (iii) the wooden block grasping (G1), and (iv) alloy tube gripping (GR2) wearing the device are reported.

subgroup can be administered. Whether, instead, the score of the first item is less than 3, the second one is tested. If it is rated as 0, then all the other items of that subgroup are credited with 0. If, otherwise, its score is higher than 0, all the other items have to be assessed. The same procedure must be followed for all the subgroups. The maximum obtainable score performing the ARAT is 57. The protocol indicates 60 s as the maximum task duration if the patient does not complete it first.

For this case study, the experimental tests were performed in a clinical environment in collaboration with the Don Carlo Gnocchi Foundation Rehabilitation Centre. The patient was seated in a wheelchair in front of a table. The test was repeated three times. In the first session, the patient performed the test without wearing the hand exoskeleton; in the second one, the hand exoskeleton was worn, and the test was conducted by setting the device to enable a hand closing/opening in 1.2 s; the third and last session was instead performed setting the device to achieve a complete closing/opening in 0.8 s, after ascertaining that it would not cause discomfort and pain to the patient. After assessing the administered tasks during the first session, the patient wore the hand exoskeleton thanks to the help of a physiotherapist: donning the sEMG bracelet required particular attention, especially to find the correct spot for sensors. It is worth noting that in this case study, it was necessary to use the wrist muscular activity for intention detection since the patient could not provide strong finger signals without fatigue and pain. Once the device was worn, an intermediate training phase was required for the classifier training. After that, the other two testing sessions were performed. Some pictures of them can be seen in Figure 2.5. The score obtained for each task is reported in Table 2.4, which highlights that the patient had no impairments in arm motion due to scoring 3 points for all gross movements in the three sessions. For the other task subgroups, the patient

Table 2.4: The scores obtained for each task during the three sessions of ARAT. HE in the first column means “Hand exoskeleton”.

| Sessions | G1 | G2 | G3 | G4 | G5 | G6 | GR1 | GR2 | GR3 | GR4 | P1 | P2 | P3 | P4 | P5 | P6 | GM1 | GM2 | GM3 | Total score |
|---|---|---|---|---|---|---|---|---|---|---|---|---|---|---|---|---|---|---|---|---|
| Without HE | 2 | 2 | 2 | 2 | 1 | 2 | 2 | 2 | 2 | 2 | 0 | 2 | 2 | 2 | 0 | 2 | 3 | 3 | 3 | 36 |
| With HE (1.2 s) | 2 | 2 | 2 | 2 | 2 | 2 | 0 | 2 | 2 | 0 | 0 | 2 | 0 | 2 | 0 | 0 | 3 | 3 | 3 | 29 |
| With HE (0.8 s) | 2 | 2 | 2 | 2 | 2 | 2 | 0 | 2 | 2 | 0 | 0 | 2 | 0 | 2 | 0 | 0 | 3 | 3 | 3 | 29 |

experienced more or less difficulty, even though the patient totalled the same score in the two sessions wearing the hand exoskeleton. To analyse the results obtained more thoroughly, the times taken to perform the various tasks (except for the gross movements) were compared in a histogram reported in Figure 2.6. Sixty seconds were assigned to tasks the patient did not complete in less time or failed to perform. Regardless of the subgroups, the histogram shows that the time taken to perform most tasks was shorter in the third session than in the second one due to the greater set speed and the greater confidence taken with the device.

Concerning the grasping activities, the histogram shows comparable times in the first and third sessions, except for the ball grasping task (G5), and a marked worsening in the second one. More observations need to be raised in this regard. First of all, it is worth noting that over the years, the patient has adjusted their grasping based on the movement they can perform, allowing them to grasp different objects; for this reason, the patient could grasp objects relatively quickly without the hand exoskeleton. The unique task the patient failed without wearing the device is the 7.5-cm-diameter cricket ball grasping (G5). Grasping large objects, indeed, could sometimes be prevented by the hand opening impairment, which instead the exoskeleton assists, as can be observed in the G5 column of the histogram (Figure 2.6), allowing for a more correct and effective grasp than without its support. Similarly, the execution time in the case of wearing the hand exoskeleton also decreases for the 10-cm-cube wooden block grasping task (G1).

Moving on to grip movements, tasks involving glasses (GR1) and a washer (GR4) were entirely prevented by hand exoskeleton usage, even though washer manipulation is also highly challenging for the patient without wearing the device since its shallow thickness. Gripping alloy tubes (GR2 and GR3) while wearing the device required more time, but it was also a more correct, stable, and effective grip than without wearing it.

Most limitations while wearing the hand exoskeleton were encountered in performing pinch movements, except for those involving the thumb and index fin-

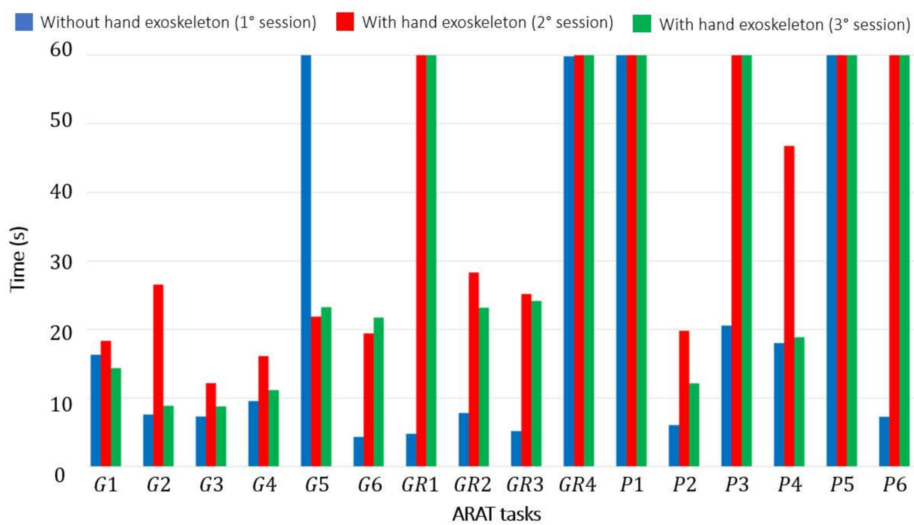


Figure 2.6: The results of the ARAT reported in a histogram in terms of the time needed to perform the matching task: the items administered are reported in the horizontal axis, while the time (in seconds) corresponding to the column height is shown in the vertical axes; the blue, red, and green column colours distinguish if the task was carried out in the first, second, or third session, respectively.

gers. The worsening performances can be attributed to the overall dimensions of the finger-handling mechanisms, which were still excessive and limited mobility, especially in confined spaces, e.g., when the patient reaches across the table to grab a coin.

Although ARAT did not show improvements from using the exoskeleton, the prototype achieved promising results, especially related to the main design requirements of wearable devices for assistive purposes. This device indeed answers the demand for wearability and portability, safety and comfort, intuitiveness, sense-of-touch preservation, force effectiveness, and affordability (it costs around 500 €), thanks to the finger-handling mechanism architecture, actuation and control systems, and mechatronic design involved. However, some flaws remained. Although all the components (including the power supply system) were integrated into the device core module to be fixed on the hand back, the complete portability for prolonged use is limited due to the mass of the exoskeleton concentrated on the hand back, whose distribution had worsened. For the same reason, the device's comfort has to be improved. The patient involved in the experimental sessions highlighted these points at the end of the tests, which altogether lasted about two hours, including training and dressing time. As the low performance when grabbing small objects highlighted, the finger-handling mechanism architecture still prevents the exoskeleton usage in confined spaces due to its overall dimensions ($80 \times 72.5 \times 70.6$ mm$^3$, reaching even 40 mm above the fingers). Device dexterity, intended as mentioned in Section 1.2, is completely lacking. Indeed, the cable transmission exploited in this prototype needs to be replaced since its configuration allows only for the active hand opening, leaving its closing passive. In addition, it sometimes presents a reversal of motion issue, requiring specific maintenance work to restart the exoskeleton that might be avoided. Dexterity is also foreclosed by the absence of independent finger motion, which would allow for fine manipulation or irregular-shaped object grasping, and the thumb-handling finger, which instead is crucial for its opposition role in object handling.

The strengths and flaws of this last prototype and the literature research presented in Chapter 1 paved the way for developing the novel hand exoskeleton presented in this thesis work and characterised by a completely renewed design. The main change is associated with the finger-handling mechanism architecture, which becomes hybrid in the new device, thus involves rigid and soft elements to achieve *force effectiveness* in performing ADLs while maintaining *small overall sizes* to ensure usage in confined spaces and for fine manipulation. Precisely, the new architecture consists of a well-known rigid mechanism (a four-bar mechanism) that acts on the middle of the proximal phalanx, exerting on it at least 15 N, a suitable value to perform the ADLs, and a soft component to which the f/e of the other phalanges is delegated as a result of the relative movement between the rigid mechanism bars. Exploiting a compliant soft architecture that by its nature does not suffer from misalignment issues and a four-bar mechanism that instead enables alignment with the finger correctly confer *comfort* and *safety* to the device, avoiding more complex designs [38, 41, 48, 56, 66]. Such requirements are also pursued thanks to the quick and easy mechanism customisation on the specific user's hand sizes performed through the optimisation procedure [105] mentioned in Subsection 2.2, and revised for the new architecture.

The new hand exoskeleton was conceived with all the components placed on the hand and upper limb to improve the overall mass distribution and avoid remote components in favour of complete *wearability* and *portability.* Two main modules will compose the device: one, to be connected to the upper limb, will include the electronic components and power supply system, while the core one, to be fixed to the hand, will consist in turn of five equal modules, one per finger, each including the finger-handling mechanism, the electric motor that actuates it, and the rigid transmission that transmits motion to the hybrid architecture. Employing one motor per finger allows for independent finger movement even if it might increase the device mass, which can be contained by carefully choosing the commercially available actuators. This aspect adds *dexterity* to the hand exoskeleton, as the gear transmission that will ensure active bidirectional movements without increasing the device's overall dimensions and improve *safety* thanks to its kinematic accuracy, which contributes to avoiding incorrect and painful movements for the patient, along with the mechanism alignment and its customisation. Initially, a flexible shaft was also considered for this application [114]. Indeed, it would allow for moving the actuation and control system away from the hand, e.g., in the forearm or upper limb, and transmit motion from the actuator to the mechanism on the hand, thus reducing the hand's mass while improving its distribution; in addition, this solution would have transmitted torque more efficiently than Bowden cables. Nonetheless, the stringent dimensional constraints on the hand prevented the usage of this component. Micro gearmotors coupled with gear transmissions appeared to be an interesting solution to include the actuation system on the core module on the hand back to pursue *wearability*, *portability*, and *lightness* by keeping low this module mass. Velcro straps and elastic bands will connect the mechanism end-effectors to the fingers, and the two modules to the hand and upper limb, respectively, thus preserving the *sense of touch* as opposed to devices fixed on gloves [48, 51, 52, 53, 58, 75, 103, 104]. The mechanism components and rigid parts of the hand exoskeleton will be 3D printed in ABS CF10 due to its remarkable mechanical features, ensuring *lightness* and *affordability*. This last requirement will be pursued in choosing all the commercially available components. The possibility of making the device by size will also be considered. Finally, sEMG signals will be maintained to provide this prototype with an *intuitive* user intention detection method. However, it is important to point out that this thesis focuses on the completely renewed mechatronic design of a hand exoskeleton for assistive purposes, while the control strategy to implement it will not be addressed in this work.

# Chapter 3

# Mechatronic design

This chapter presents the novel assistive hand exoskeleton developed during the Ph.D. Course. As already mentioned at the end of Chapter 2, the new device, whose design is driven by the desire to overcome the limitations of other existing assistive solutions, consists of two main modules: one for electronics to be fixed on the upper limb and the other to be placed on the hand consisting in turn of five modules, one per finger, with the same hybrid architecture.

The hybrid architecture is the focus of the first part of this chapter, in which both the rigid and soft architecture are presented: for the former, the kinematic and kinetostatic analyses are solved, while a preliminary study of the latter is reported.

The second part of the chapter, instead, is devoted to presenting the design of the entire exoskeleton: the mechanical components chosen for developing the new prototype are reported, together with verification and dimensioning of purchased components and Finite Element Method (FEM) analysis of those produced in-house by 3D printing. Finally, also the electronic components required for its functioning are presented.

## 3.1 Finger-handling mechanism synthesis

First hybrid solutions [51, 52, 69] have been introduced in the literature in recent years to reduce the overall sizes above the fingers and increase the device compliance, improving comfort, as those reported in Figure 3.1. Different architectures are implemented: from rigid vertebrae-like components serving as

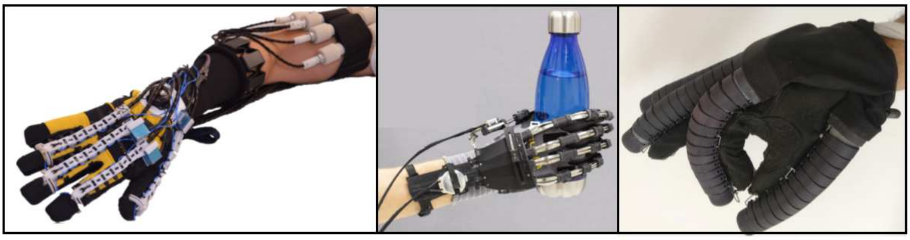

Figure 3.1: Hybrid solutions detected in the literature: from the left, the hand exoskeletons of Rose *et al.* [51], Dittli *et al.* [52], and Kladovasilakis *et al.* [69].

the termination point of a Bowden cable transmission [51] to rigid components, within which layered springs slide, corresponding to the interaction points between the exoskeleton and hand that prevent the finger hyperextension [52, 115], as the modular external cover consisting of rings in rigid polymer, which enhance the structural integrity [69]. The solutions of [51] and [69] are quite force effective since they measured 16.6 N and 19.5 N, respectively, during grasping tasks, while the target value is 15 N per finger. However, the actuation systems employed in [51, 52, 69] require their remote location from the hand. Thus, the hybrid architecture of the finger-handling mechanism described in this section was designed to overcome these issues. The novel hybrid architecture, designed to place the actuator and transmission directly on the hand, was conceived only for the finger f/e and initially developed for the thumb since it was lacking in the previous MDM Lab prototypes. It is important to point out that the mechanism allows for the f/e of its phalanges while leaving passive the CMC joint circumduction, i.e., the thumb opposition, not to add complexity and mass to the system. Besides, although initially designed for the thumb, it can be easily generalised to the other fingers by considering the matching dimensions, ROM, and kinematics derived from the specific user's hand anatomy.

After some preliminary iterations [116], the actual architecture shown in Figure 3.2 was defined [117]: a well-known rigid architecture, i.e., a four-bar mechanism, acts on the middle of the proximal phalanx, allowing for its f/e, and exerts suitable forces for ADLs on it; a flat spring, whose movement is due to the relative motion between the components of the rigid mechanism, is instead introduced to enable the f/e of the other phalanges while keeping the mechanism overall sizes on the finger small. A passive DOF was also introduced to leave the a/a movement free, thus improving the mechanism compliance by

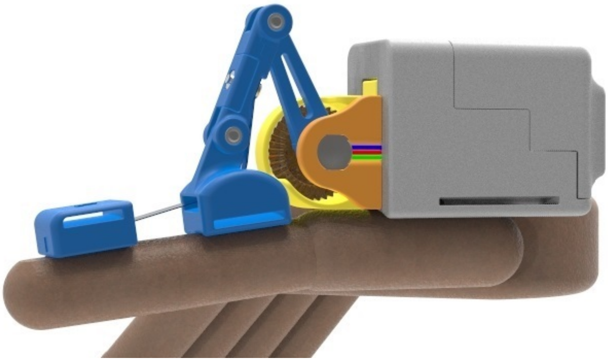

Figure 3.2: An overview of the hybrid-architecture finger exoskeleton that is the base concept for the hand exoskeleton proposed in this work.

allowing it to adapt to the finger and not force it into wrong poses.

### 3.1.1 The rigid architecture

As mentioned, the rigid architecture of the overall mechanism, consisting of a four-bar mechanism, was designed to act only on the middle of the proximal phalanx and enable its f/e around the MCP joint. As visible on the left of Figure 3.3, the four-bar mechanism involves Link 1, Link 2, a third bar that includes Link 3 and the finger segment between the End-Effector (EE) and MCP joint (matching the segment $O_3O_{EE}$ of length $d$ on the right of Figure 3.3), and another segment (matching $O_0O_3$ of length $e$ on the right of Figure 3.3), connecting the actuated joint ($O_0$) and the MCP one. The mechanism kinematic, therefore, closes on the hand. Additionally, it has four revolute joints, one of which is anatomical. According to the Grübler formula, the mechanism has one DOF, meaning that its kinematics can be solved as a function of one independent variable, knowing the whole geometry.

The mechanism is designed to produce a RCM overlapping with the MCP joint and so that its EE (Figure 3.3) follows the trajectory of the matching point on the surface of the proximal phalanx, determined by the natural finger motion, which is deduced by solving the hand kinematic model through the D-H method, as mentioned in Subsection 2.1. From now on, the adjective *desired* will denote the trajectory thus determined. It is worth highlighting that, evaluated referring to the MCP joint, this trajectory corresponds to a circumference arc

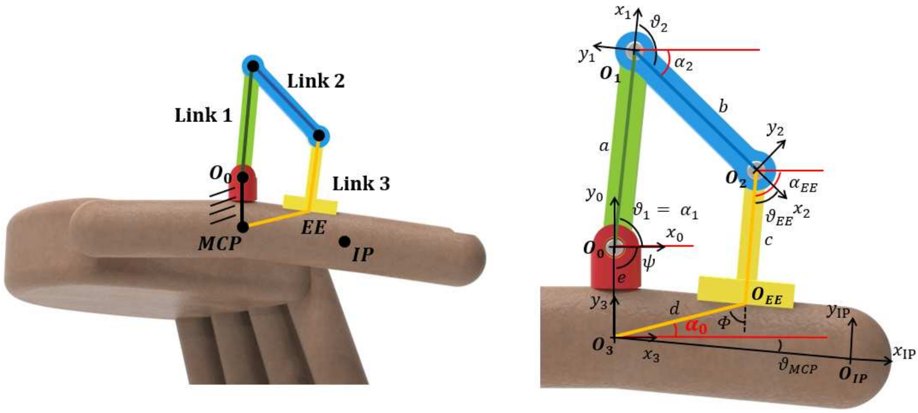


Figure 3.3: On the left, the schematic four-bar mechanism placed on the thumb of a hand parametric CAD model is shown. Its bars are highlighted: (i) the mechanism frame, black coloured, (ii) Link 1, green coloured, (iii) Link 2, blue coloured and (iv) the third bar, consisting of the rigid mechanism Link 3 and part of the proximal phalanx, yellow coloured. In addition, the IP, MCP joint ($O_3$), and EE are shown. On the right, the reference frames convention for kinematic analysis and the length of each bar are reported. The reference frame integral to the distal phalanx and centred in the IP joint ($O_{IP}x_{IP}y_{IP}$) and the f/e angle of the proximal phalanx $\theta_{MCP}$ are highlighted.

since EE remains at the same distance from the MCP joint during hand opening and closing due to belonging to the same rigid body, the proximal phalanx. By converting it into polar coordinates, the radial one corresponds to the radius of the desired circumference arc that remains constant during the motion; instead, the angular coordinate, identified by the angle $\alpha_0$, varies as much as $\theta_{MCP}$, indicating the proximal-phalanx f/e (Figure 3.3). The two angles indeed correspond minus a constant dependent on the specific user's proximal phalanx length and thickness. Since it directly depends on the phalanx f/e, $\alpha_0$ was chosen as the independent variable as a function of which to solve the kinematics.
A kinematic study was conducted to ensure the EE correctly rotates around the MCP joint and covers the *desired trajectory* as much as possible. The EE trajectory referred to the linkage mechanism and, depending on its kinematics, will be identified with the adjective *actual*.

### Kinematic analysis

An in-depth analysis of the single-DOF rigid-architecture kinematics is detailed in the following. The forward kinematic analysis allows for determining the pose (i.e., position and orientation) of all the mechanism points, including its EE. For the sake of brevity, the analysis is reported only referred to the thumb mechanism but can be equally applied to other fingers as well. The reference systems were positioned as shown in Figure 3.3. They are numerically labelled clockwise from the actuated joint $O_0$ to the MCP one $O_3$. The kinematics is referred to the $O_0x_0y_0$ frame, which is fixed and centred in the $O_0$ joint. The frame $O_3x_3y_3$ is centred in the MCP joint. The segment $O_0O_3$ is the mechanism frame. It forms the angle $\psi = -90$ to the horizontal, thus determining the actuated joint $O_0$ placement right above the MCP joint ($O_3$) to enable the introduction of the passive joint for a/a. The other reference frames ($O_1x_1y_1$, $O_2x_2y_2$) are instead integral to Link 1 and Link 2, respectively centred in the passive joints $O_1$, $O_2$. $\alpha_0$ is the angle the segment $O_3O_{EE}$ forms to the horizontal, as the other $\alpha$-angle ($\alpha_1$, $\alpha_2$, $\alpha_{EE}$) are the angles Link 1, Link 2, and Link 3 form to the horizontal. The following convention was considered for the kinematic analysis: (i) the symbol $\mathbf{O}_j^i$ indicates the $j$-th joint position evaluated referring to the $i$-th coordinates frame; (ii) the symbol $\mathbf{R}_j^i$ defines the $j$-th frame orientation referred to the $i$-th one (it is worth noting that the motion of the single-DOF mechanism is planar, determining that all rotation matrices can be expressed as basic rotations about the $z$-axis); (iii) the superscript is omitted if positions are referred to the fixed frame $O_0x_0y_0$; (iv) goniometric operators as sine and cosine are replaced with $s$ and $c$, respectively.
The joint poses are reported in Equations from 3.1 to 3.5:

$$\mathbf{O}_1 = -\mathbf{R}_1^0\mathbf{O}_0^1 \tag{3.1}$$

$$\mathbf{O}_2 = \mathbf{O}_1 + \mathbf{R}_1^0\mathbf{O}_2^1 \tag{3.2}$$

$$\mathbf{O}_{EE} = \mathbf{O}_2 + \mathbf{R}_2^0\mathbf{O}_{EE}^2 \tag{3.3}$$

$$\mathbf{O}_3 = -\mathbf{R}_3^0\mathbf{O}_0^3 \tag{3.4}$$

$$\mathbf{O}_{EE} = \mathbf{O}_3 + \mathbf{R}_3^0\mathbf{O}_{EE}^3 \tag{3.5}$$

Since Equations 3.3 and 3.5 have the same results, thus one of these can be exploited to verify the correctness of the kinematic solution, only four vector equations describe the system state entirely, resulting in the following unknowns vector:

$$\mathbf{s} = [O_{1x}\ O_{1y}\ O_{2x}\ O_{2y}\ O_{EEx}\ O_{EEy}\ O_{3x}\ O_{3y}]' \in R^8. \tag{3.6}$$

Specifically, Equation 3.1 can be explicitly expressed as follows:

$$\mathbf{O}_1 = -\begin{bmatrix} c_{\theta_1} & -s_{\theta_1} & 0 \\ s_{\theta_1} & c_{\theta_1} & 0 \\ 0 & 0 & 1 \end{bmatrix} \begin{bmatrix} -a \\ 0 \\ 0 \end{bmatrix} \tag{3.7}$$

while, bearing in mind that vector $\mathbf{O}_2^1$ in Equation 3.2 is defined as $\mathbf{O}_2^1 = -\mathbf{R}_2^1\mathbf{O}_1^2$, $\mathbf{O}_2$ can be made explicit as

$$\mathbf{O}_2 = -\begin{bmatrix} c_{\theta_1} & -s_{\theta_1} & 0 \\ s_{\theta_1} & c_{\theta_1} & 0 \\ 0 & 0 & 1 \end{bmatrix} \begin{bmatrix} -a \\ 0 \\ 0 \end{bmatrix} - \begin{bmatrix} c_{\theta_1} & -s_{\theta_1} & 0 \\ s_{\theta_1} & c_{\theta_1} & 0 \\ 0 & 0 & 1 \end{bmatrix} \begin{bmatrix} c_{\theta_2} & -s_{\theta_2} & 0 \\ s_{\theta_2} & c_{\theta_2} & 0 \\ 0 & 0 & 1 \end{bmatrix} \begin{bmatrix} -b \\ 0 \\ 0 \end{bmatrix} \tag{3.8}$$

Then, considering that $\mathbf{O}_{EE}^2$ is defined as $\mathbf{O}_{EE}^2 = [cc_{\theta_{EE}}\ cs_{\theta_{EE}}\ 0]'$, Equation 3.3 becomes

$$\begin{aligned} \mathbf{O}_{EE} = -\begin{bmatrix} c_{\theta_1} & -s_{\theta_1} & 0 \\ s_{\theta_1} & c_{\theta_1} & 0 \\ 0 & 0 & 1 \end{bmatrix} \begin{bmatrix} -a \\ 0 \\ 0 \end{bmatrix} - \begin{bmatrix} c_{\theta_1} & -s_{\theta_1} & 0 \\ s_{\theta_1} & c_{\theta_1} & 0 \\ 0 & 0 & 1 \end{bmatrix} \begin{bmatrix} c_{\theta_2} & -s_{\theta_2} & 0 \\ s_{\theta_2} & c_{\theta_2} & 0 \\ 0 & 0 & 1 \end{bmatrix} \begin{bmatrix} -b \\ 0 \\ 0 \end{bmatrix} + \\ + \begin{bmatrix} c_{\theta_1} & -s_{\theta_1} & 0 \\ s_{\theta_1} & c_{\theta_1} & 0 \\ 0 & 0 & 1 \end{bmatrix} \begin{bmatrix} c_{\theta_2} & -s_{\theta_2} & 0 \\ s_{\theta_2} & c_{\theta_2} & 0 \\ 0 & 0 & 1 \end{bmatrix} \begin{bmatrix} cc_{\theta_{EE}} \\ cs_{\theta_{EE}} \\ 0 \end{bmatrix} \end{aligned} \tag{3.9}$$

Finally, Equation 3.4 results as below:

$$\mathbf{O}_3 = -\begin{bmatrix} 1 & 0 & 0 \\ 0 & 1 & 0 \\ 0 & 0 & 1 \end{bmatrix} \cdot \begin{bmatrix} -ec_{\psi} \\ -es_{\psi} \\ 0 \end{bmatrix} \tag{3.10}$$

It is worth noting the identity matrix as $\mathbf{R}_3^0$ due to the absence of the relative rotation between $O_3x_3y_3$ and $O_0x_0y_0$ frames. The kinematic solution is verified through solving also Equation 3.5, while considering that the vector $\mathbf{O}_{EE}^3$ can be expressed as $\mathbf{O}_{EE}^3 = [dc_{\alpha_0}\ ds_{\alpha_0}\ 0]'$.
However, it is fundamental to know the relations between each joint angle and $\alpha_0$, indicative of the f/e movement, and lengths of each bar to solve the kinematics. The unknowns vector $\mathbf{s} \in R^8$ can be expressed indeed as a function of the angle $\alpha_0$ and a vector $\mathbf{x}$ including the bars length, as formalized below:

$$s = f(\mathbf{x}, \alpha_0). \tag{3.11}$$

If the vector $\mathbf{x}$ is defined as $\mathbf{x} = [a \ b \ c \ d \ e]' \in R^5$ and it is derived from the kinematic optimization procedure that will be described in the following, the relations between the independent variable $\alpha_0$ and the other joint angles were determined through the linkage mechanism *closure equation*, which can be expressed as below (Figure 3.3):

$$\boldsymbol{O_1O_0} + \boldsymbol{O_2O_1} + \boldsymbol{O_{EE}O_2} = \boldsymbol{O_3O_0} + \boldsymbol{O_{EE}O_3} \tag{3.12}$$

By projecting this equation along the $O_0x_0y_0$-frame $x$ and $y$ axes, the following equations system can be deduced:

$$\begin{cases} ac_{\alpha_1} + bc_{\alpha_2} + cc_{\alpha_{EE}} = ec_{\psi} + dc_{\alpha_0} \\ as_{\alpha_1} + bs_{\alpha_2} + cs_{\alpha_{EE}} = es_{\psi} + ds_{\alpha_0} \end{cases} \tag{3.13}$$

By taking terms depending on $\alpha_2$ to each equation left member, moving the others to the right, and bearing in mind that

$$\alpha_0 + \phi - \alpha_{EE} = \pi \tag{3.14}$$

since $\alpha_{EE}$ is a negative number, the equations system results

$$\begin{cases} bc_{\alpha_2} = -ac_{\alpha_1} + cc_{\alpha_{0+\phi}} + ec_{\psi} + dc_{\alpha_0} \\ bs_{\alpha_2} = -as_{\alpha_1} + cs_{\alpha_{0+\phi}} + es_{\psi} + ds_{\alpha_0} \end{cases} \tag{3.15}$$

Referring to Figure 3.3, it is worth noting that $\phi$, which is the angle between the segment $O_3O_{EE}$ and the extension of segment $O_2O_{EE}$, can be evaluated as the complementary angle of $\alpha_0$ when $\theta_{MCP} = 0$, and it is a constant depending on the specific user hand anatomy.
After squaring and summing the Equations system 3.15, it can be achieved:

$$\begin{aligned} b^2 = a^2 + c^2 + d^2 + e^2 - 2ac(c_{\alpha_1}c_{\alpha_{0+\phi}} + s_{\alpha_1}s_{\alpha_{0+\phi}}) - 2ae(c_{\alpha_1}c_{\psi} + s_{\alpha_1}s_{\psi}) + \\ - 2ad(c_{\alpha_1}c_{\alpha_0} + s_{\alpha_1}s_{\alpha_0}) + 2ce(c_{\alpha_{0+\phi}}c_{\psi} + s_{\alpha_{0+\phi}}s_{\psi}) + 2ed(c_{\psi}c_{\alpha_0} + s_{\psi}s_{\alpha_0}) + \\ + 2cd(c_{\alpha_0}c_{\alpha_{0+\phi}} + s_{\alpha_0}s_{\alpha_{0+\phi}}) \end{aligned} \tag{3.16}$$

Equation 3.16 can be solved through the *added angle method* if reported in the form of $A = Bc_1 + Cs_1$. To this purpose, in Equation 3.16, terms independent of $\alpha_1$ are collected on its left member, while those depending on $\alpha_1$ separately on the right, determining the following expressions for $A$, $B$, and $C$,

$$A = b^2 - a^2 - c^2 - d^2 - e^2 - 2ce(c_{\alpha_0+\phi}c_\psi + s_{\alpha_0+\phi}s_\psi) - 2ed(c_\psi c_{\alpha_0} + s_\psi s_{\alpha_0}) + \\ - 2cd(c_{\alpha_0}c_{\alpha_0+\phi} + s_{\alpha_0}s_{\alpha_0+\phi}) \quad (3.17)$$

$$B = -2acc_{\alpha_0+\phi} - 2aec_\psi - 2adc_{\alpha_0} \quad (3.18)$$

$$C = -2acs_{\alpha_0+\phi} - 2aes_\psi - 2ads_{\alpha_0} \quad (3.19)$$

in which the last term of Equation 3.17 can be reduced to $-2cdc_\phi$ by the cosine addition formulas. Thus, the *added angle method* and goniometric function transformations allow for expressing Equation 3.16 as

$$A = \sqrt{(B^2 + C^2)}\sin(\alpha_1 + \rho) \quad (3.20)$$

where $\rho$ can be evaluated as $\rho = \arctan 2(\sin\rho, \cos\rho)$, with $\sin\rho = \frac{B}{\sqrt{B^2+C^2}}$ and $\cos\rho = \frac{C}{\sqrt{B^2+C^2}}$.
Since $A$, $B$, and $C$ depend only on $\alpha_0$, once vector $\mathbf{x}$ is derived, $\rho$ can be evaluated by exploiting the arctan 2 function, and the two following alternative solutions are achieved by reversing Equation 3.20:

$$\alpha_{1,1} = \sin^{-1}\frac{A}{\sqrt{B^2 + C^2}} - \rho \quad (3.21)$$

$$\alpha_{1,2} = \pi - \sin^{-1}\frac{A}{\sqrt{B^2 + C^2}} - \rho \quad (3.22)$$

In this specific case study, it is possible to choose the solution for which $\alpha_1$ spans in the range $[-\pi/2, \pi/2]$. If these equations allow for expressing $\alpha_1$ as a function of $\alpha_0$, the expression for $\alpha_2$ can be derived from Equations 3.15, while Equation 3.14 is valid for $\alpha_{EE}$. The value obtained from such expressions is due to considering the angle $\theta_{MCP}$, which influences the angle $\alpha_0$, while spanning along the desired ROM specified in Table 2.2 in Section 2.1. Within this range, $\alpha_0$ initially assumes positive and then negative values, $\alpha_1$ decreases from positive to negative values, while $\alpha_2$ and $\alpha_{EE}$ are negative and negatively increase. The angle trends retrieved from solving the *closure equation* allow to deduce the relations between these angles and the joint variables:

$$\theta_1 = \alpha_1 \tag{3.23}$$
$$\theta_2 = \alpha_2 - \alpha_1 \tag{3.24}$$
$$\theta_{EE} = \alpha_{EE} - \alpha_2 \tag{3.25}$$

Equations from 3.1 to 3.25 allows solving the four-bar mechanism's kinematics once coupled with the finger. However, as reported in Equation 3.11, the unknowns vector is also a function of the mechanism bar dimensions, collected in the vector $\mathbf{x}$. Such a vector results from the kinematic optimization procedure that allows determining the mechanism's dimensions whose EE best follows the *desired trajectory*. In particular, this procedure compares the *actual* and *desired trajectories*, expressed in polar coordinates, to identify the dimensions of the mechanism that minimize the error between them. If the *desired trajectory* derives from the user hand kinematics, the *actual* one is that of the point $O_{EE}$ (Figure 3.3) evaluated by solving the mechanism kinematics as reported above. Thus, the final goal of this procedure is to adapt the mechanism to the specific user's anatomy to improve the device comfort and prevent wrong and painful finger movement.
For this purpose, the *Nelder-Mead* optimisation algorithm [105] mentioned in Section 2.2 was exploited after making appropriate modifications for the case study. In particular, the code inputs are a first attempt vector $\mathbf{x}_0$, the hand palm and finger thickness of the specific user, and the vertical distance between the hand back and actuated joint due to the overall dimensions of the actuation system. The sum of this last distance and half of the hand palm thickness indeed determines the length $e$, the only vector $\mathbf{x}$ component not subjected to the optimisation procedure. For the specific case, in addition, the following six constraint expressions were introduced in the code to define the admissible region $S$, and they are based on the mechanism geometry and overall dimensions:

$$\begin{array}{ccc} \alpha_{1max} < 90^\circ & \alpha_{2max} < 0 & \alpha_3 < \alpha_2 \\ O_{1x,(1)} < O_{2x,(1)} & O_{2x,(1)} < O_{EEx,(1)} & O_{1y,max} < 27 \end{array} \tag{3.26}$$

where the subscript (1) indicates that the variable is evaluated at the first ROM step, corresponding to the finger maximum extension (or complete opening). As already mentioned, for each iteration, a new vector $\widetilde{\mathbf{x}}$ that solves the kinematics is produced, and the error between the two compared trajectories, evaluated in terms of the difference between their radial coordinates measured at the same angular coordinate, is calculated. Finally, the vector producing the lowest ob-

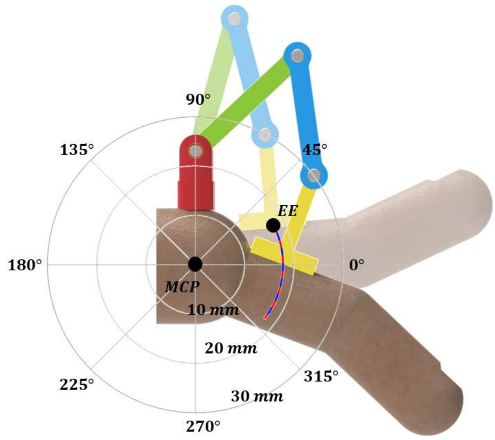


Figure 3.4: The comparison between the *desired* (continuous blue) and *actual trajectories* (dashed red lines) in polar coordinates.

jective function $f(x)$ (as the one presented in Section 2.2) is a local optimum ensuring the minimum error between the compared trajectory and possibly satisfying all the problem constraints. This resulting vector $\mathbf{x}$, which collects the dimensions for designing the linkage mechanism bars, is an input, together with the angle $\alpha_0$ varying according to the desired ROM, to solve the mechanism kinematics and derive the EE *actual trajectory*. This vector is, hence, saved in a text file (.txt) to be connected to a parametric CAD model in the software SolidWorks so that for each new optimised result, the model updates. Figure 3.4 shows the *desired* and *actual trajectories* of the EE point referred to the thumb finger of a voluntary healthy subject enrolled for the study. Different optimisations were performed for each finger, resulting in the dimensions reported in Table 3.1. It can be noted the obvious similarity of the two compared trajectories, achieving a maximum error during different optimisation processes performed for the same fingers on the order of $10^-6$, which can be traced back to the extreme straightforwardness of the *desired trajectory*, which allows easily detecting a mechanism whose EE covers an *actual trajectory* similar to the desired one.

| | a [mm] | b [mm] | c [mm] | d [mm] | e [mm] |
|---|---|---|---|---|---|
| Thumb | 28.92 | 25.00 | 18.66 | 17.78 | 24.20 |
| Index | 26.72 | 30.19 | 13.85 | 24.41 | 25.91 |
| Middle | 26.75 | 29.65 | 12.98 | 28.53 | 23.24 |
| Ring | 27.33 | 28.58 | 13.41 | 26.91 | 24.09 |
| Small | 28.86 | 25.15 | 20.10 | 19.72 | 24.67 |

Table 3.1: Dimensions of the four-bar mechanism bars for the healthy subject enrolled for the study resulted from the optimisation process performed for all the fingers.

### Kinetostatic analysis

A 15-N force perpendicular to the proximal phalanx was targeted to achieve *efficacy-in-ADLs* requirement [83, 84, 85]. Thanks to the possibility of neglecting dynamic effects — due to the low masses and velocities involved — the mechanism kinetostatic analysis can be solved to calculate the torque $\tau_z$ to be applied to the mechanism actuated joint ($O_0$) so that its EE ($O_{EE}$) exerts such a desired force. This information will then be necessary to choose the components of the actuation system.
The torque $\tau_z$ was initially measured by exploiting the *Principle of Virtual Work*, and then the value was verified through the kinetostatic analysis, which was also performed to evaluate the reaction forces at each mechanism joint. In the case study, the only external forces applied to the mechanism are the torque $\tau_z \in R$ and force $\mathbf{F} \in R^3$, arranged in the load configuration shown in Figure 3.5. Considering $\alpha_0$ as the generalised coordinate, the *Principle of Virtual Work* can be formalised as follows:

$$\tau_z \ \delta\alpha_1(\alpha_0) + \mathbf{F}^T \cdot \delta\mathbf{O}_{EE}(\alpha_0) = 0 \tag{3.27}$$

where $\delta\alpha_1 \in R$ and $\delta\mathbf{O}_{EE} \in R^3$ are the virtual displacement of the actuated joint and EE, respectively. Both $\delta\alpha_1$ and $\delta\mathbf{O}_{EE}$ can be expressed as a function of the generalised coordinate as reported below:

$$\delta\alpha_1(\alpha_0) = \frac{\partial\alpha_1}{\partial\alpha_0}\delta\alpha_0 \tag{3.28}$$

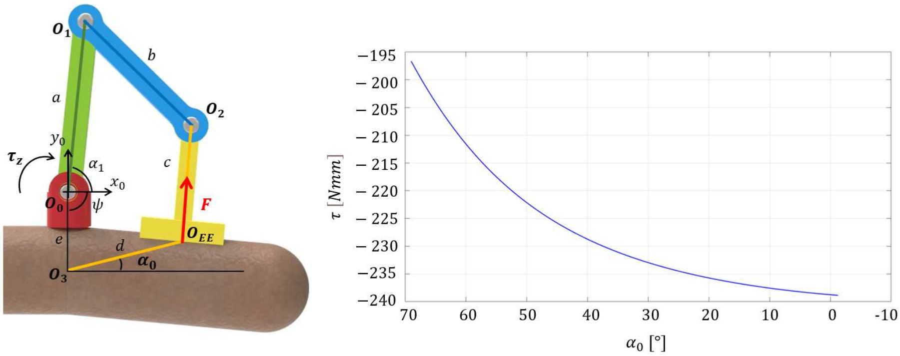


Figure 3.5: On the left, the schematic mechanism representation with external forces applied, and, on the right, the torque trend as a function of $\alpha_0$, resulting from solving the *Principle of Virtual Work* for the linkage mechanism.

$$\delta \mathbf{O}_{EE}(\alpha_0) = \frac{\partial \mathbf{O}_{EE}}{\partial \alpha_0} \delta \alpha_0 = \begin{bmatrix} \frac{\partial O_{EE\,x}}{\partial \alpha_0} \\ \frac{\partial O_{EE\,y}}{\partial \alpha_0} \\ 0 \end{bmatrix} \delta \alpha_0 \tag{3.29}$$

Finally, considering $\mathbf{F}^T = [F_x \; F_y \; 0]$, Equation 3.27 can be rewritten as:

$$\tau_z \frac{\partial \alpha_1}{\partial \alpha_0} \delta \alpha_0 + [F_x \; F_y \; 0] \cdot \begin{bmatrix} \frac{\partial O_{EE\,x}}{\partial \alpha_0} \\ \frac{\partial O_{EE\,y}}{\partial \alpha_0} \\ 0 \end{bmatrix} \delta \alpha_0 = 0 \tag{3.30}$$

where $\frac{\partial \alpha_1}{\partial \alpha_0}$ can be deduced from Equation 3.21 in Section 3.1.1 as follows:

$$\frac{\partial \alpha_1}{\partial \alpha_0} = \frac{\partial (\sin^{-1} \frac{A}{\sqrt{B^2+C^2}} - \rho)}{\partial \alpha_0} \tag{3.31}$$

and $\frac{\partial \mathbf{O}_{EE}}{\partial \alpha_0}$ is derived from Equation 3.5, resulting in the vector $[-ds_0 \; dc_0 \; 0]'$. Equation 3.30 was implemented in MATLAB and solved by varying the generalised coordinate $\alpha_0$ within its ROM (depending on that in Table 2.2). The resulting $\tau_z$ trend is reported in Figure 3.5 as a function of $\alpha_1$, meaning the angular coordinate of the joint that this torque will then actuate. Table 3.2 summarises the maximum values achieved for all the fingers.

| | Thumb | Index | Middle | Ring | Small |
|---|---|---|---|---|---|
| $\tau_z$ [Nmm] | 238.86 | 330.19 | 370.61 | 355.33 | 262.26 |

Table 3.2: Values of the maximum torque required by each finger mechanism to exert at least 15 N on the proximal phalanx.

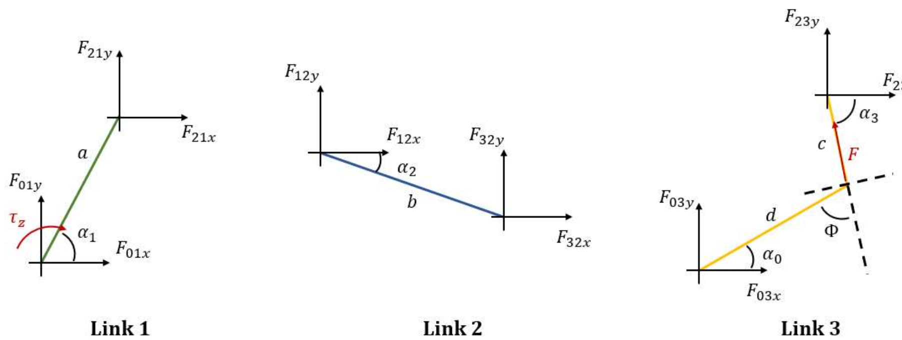


Figure 3.6: The outline of the linkage mechanism bars in which both reaction and external forces are considered to solve Equations 3.32-3.34.

The same values were detected by solving the kinetostatic analysis of the mechanism. Given the possibility of solving the equivalent static problem due to low mass and velocities, the system is in equilibrium if the resulting forces and moments are null for each bar after replacing the revolute joints at their extremities with the matching constraint reaction components along the $x$ and $y$ axes. In other words, the *Cardinal Equations of Statics* for a planar mechanism must be satisfied by each of them:

$$\sum F_x = 0 \tag{3.32}$$

$$\sum F_y = 0 \tag{3.33}$$

$$\sum M_z = 0 \tag{3.34}$$

Figure 3.6 shows the forces outline exploited for the kinetostatic analysis of each mechanism bar.

It is worth noting that if, at this point of the study, this analysis was performed to detect the torque required so that the linkage mechanism exerts at least 15 N on the middle of the proximal phalanx, thus to choose the actuation system to achieve this requirement, then it will be repeated to evaluate the reaction forces at each joint if the maximum actuator torque is delivered, which the mechanism bars must withstand. Besides, at the moment, the rigid and soft architectures were considered decoupled, and the actuation system was defined only based on the rigid architecture. It is, therefore, expected that the introduction of the soft component will result in reducing the force exerted on the finger.

### 3.1.2 The soft architecture

The soft architecture is designed to enable the f/e movement of the thumb distal phalanx (also the intermediate one for the other fingers) while keeping the overall mechanism dimensions above the finger as reduced as possible. Cable-driven [51, 53, 73, 75, 98], fibre-reinforced [69, 72], polymer-or-elastomer-based [103, 104], and fabric-based [49, 58] solutions are the most frequently employed in the literature. However, as mentioned in Section 1.2, they usually require remote location of some components (e.g., electronic components, actuators, power supply) to achieve a better distribution of masses, thus reducing the device wearability and end-user mobility. In addition, they prevent the sense of touch. Therefore, flat springs were chosen for this purpose, similar to the solution presented in [52]. However, if in [52] a layered-spring system is driven by a rack-and-pinion mechanism actuated by DC motors through Bowden cables, in this study, a single flat spring was exploited to enable the distal phalanx f/e movement thanks to the relative motion between Link 2 and 3 (see Figure 3.7). The spring is placed at a distance of $h_s$ from the distal-phalanx axis. Its ends are fixed to Link 2 and the distal-phalanx EE, while the spring itself may slide into the proximal-phalanx EE. Specifically, when the rigid architecture actuates the proximal phalanx f/e, its EE rotates around $O_2$ (see Figure 3.3) according to the four-bar mechanism kinematics, and the relative movement between Link 2 and Link 3 determines the variation of the distance separating point B and A. Referring to Figure 3.7, it is worth noting that the angle $\gamma$ decreases during the flexion movement that produces an approach of point B to point A. Since the flat spring elasticity is negligible in the longitudinal direction and not fixed to Link 3, this movement causes the spring to slide into the housing, which has been designed in the proximal-phalanx EE for this purpose. For a first approximation, the spring sliding into Link 3 can be compared to the change in the $AB$ distance during the flexion movement. In addition, the reduction of the $AB$ distance can be translated into the increase of the $CD$ distance,

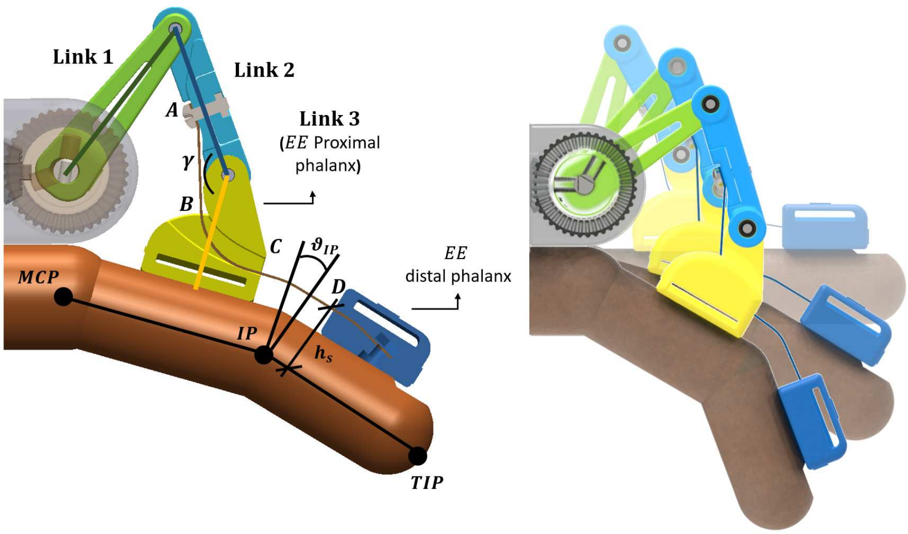


Figure 3.7: On the left, a sectional view of the soft architecture. A indicates the housing for the spring end to Link 2, B is the inlet for the spring into the proximal-phalanx EE, C is the exit point of the spring from it, and D shows the spring inlet to the distal-phalanx EE. On the right, the spring behaviour during the flexion movement.

measured along the spring, and not as minimum distance among these points. Geometric considerations show that the springs are compelled to flex around the IP joint, which represents a RCM for this architecture, thus producing the distal-phalanx flexion by pushing its EE to which the spring is fixed. On the contrary, the spring produces the distal-phalanx extension when the four-bar mechanism causes the proximal-phalanx extension. This condition determines the increase of the $AB$ distance due to reverse sliding. Accordingly, the $CD$ distance reduces, and the distal-phalanx EE is pulled.
The correlation between the sliding $l$ of the spring into the proximal-phalanx EE and IP joint f/e angle $\theta_{IP}$ can be expressed as follows:

$$l = \frac{2\pi h_s}{360}\theta_{IP} \tag{3.35}$$

It is worth noting that the soft architecture is not involved in the opti-

| | Thumb | Index | Middle | Ring | Small |
|---|---|---|---|---|---|
| $\theta_f$ [°] | 51.02 | 72.06 | 77.14 | 73.13 | 78.26 |
| $\theta_{PIP}$ [°] | - | 43.23 | 46.28 | 43.90 | 46.96 |
| $\theta_{DIP}$ [°] | - | 28.82 | 30.86 | 29.27 | 31.30 |

Table 3.3: The maximum flexion ($\theta_f$) achievable through the spring sliding in the configuration chosen: for the thumb, it corresponds with the IP joint ROM, while for the other fingers it contributes to both the PIP and DIP joints ROM according to the mentioned intrafinger constraint.

misation procedure described above, but the springs' length can be evaluated considering the phalanges lengths, EE dimensions, and optimised dimensions of the rigid architecture. Specifically, the spring configuration (Figure 3.7) is determined by the position of points $A$ and $B$, and $h_s$. All these parameters affect the achievable IP joint f/e range, valuable through Equation 3.35. For each tested configuration, the maximum sliding $l$ was evaluated as the variation of the distance $AB$ among the rest ($\theta_{MCP} = 0°$) and the complete finger flexion ($\theta_{MCP} = -60°$) condition. The corresponding $\theta_{IP}$ was calculated by reversing Equation 3.35, and the configuration enabling the more extensive IP joint f/e — $\simeq 50°$ — was chosen. Even if the complete IP ROM ($\simeq 110°$) is not reachable, such a configuration can be considered acceptable based on [118], in which a study concerning thumb joint ranges in grasping ordinary objects of daily living is presented.

In the case concerning the other fingers, a consideration must be made: the soft-architecture EE still acts on the distal phalanx, thus determining also the intermediate phalanx f/e. According to intrafinger constraints that correlate the angular coordinates of the different finger joints during manipulation tasks, such as cylindrical grasp [119, 120], a relation between the PIP and DIP joints ROM exist. In particular, it is valid that $\theta_{DIP} \simeq \frac{2}{3}\theta_{PIP}$. Due to such a relation, it is possible to assume that the maximum sliding achieved from the rest to the complete flexion condition of the proximal phalanx translates into the flexion of both these joints. The total maximum flexion $\theta_f$ that can be achieved with the chosen configurations is reported in Table 3.3 for all the fingers, in which it is highlighted that if for the thumb $\theta_f$ contributes only to the IP joint flexion, for the other fingers, it contributes to the PIP and DIP joints flexion. The table shows how the spring configurations chosen also for the other fingers (as they result in the best among those evaluated) allow to reach about half of the ROM targeted in the hand kinematic model presented in Section 2.1. However, the

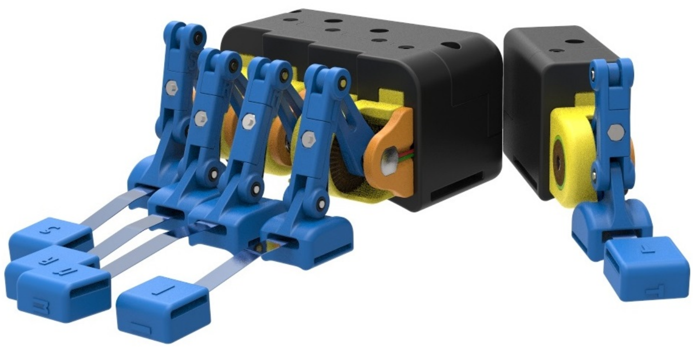

Figure 3.8: The CAD model of the hand exoskeleton resulted from the design process described in this section.

reachable PIP and DIP joints ROM resulted about $\simeq 70\%$ and $\simeq 55\%$ of their matching functional ROM measured in [121] and defined as the ROM at each joint required to complete the 90% of gripping tasks daily typical. Due to the approximated evaluation, these results seemed promising and a good starting point for experimental testing of the hybrid architecture.

## 3.2 Hand exoskeleton design

The finger-handling mechanism presented in the previous section was the base concept for designing and developing the whole hand exoskeleton shown in Figure 3.8. In the remainder of this section, all the design choices made to develop a completely wearable and portable device that meets the requirements of lightness, small overall dimensions, force effectiveness, dexterity, comfort, and affordability will be presented.

### 3.2.1 Actuation system

As mentioned in Section 1.2, different types of actuation can be employed in wearable robotic devices, and each grants unique features to the system [100]. However, among those available, electric motors seemed to be the best candidates for this application, which involves using one motor per finger. Indeed, they are those that most easily can be placed on the hand, thus pursuing the *wearability* and *portability* requirements, allowing at the same time for suitable

forces for ADLs. In addition, it is possible to find the one that best meets the required specifications among the different models of as many weights, sizes, power, and costs available on the market.
Housing all the actuators on the hand was preferred to placing them in the forearm while transmitting motion through flexible shafts. These components' peculiarity consists of the ability to transmit torque like rigid shafts, while they can also be bent as happens to cable transmission, allowing for relative movements of the driving and driven components during operational conditions [114]. Unlike Bowden cables, they do not suffer from friction loss or backlash issues. Nonetheless, the stringent dimensional constraint prevented exploiting this attractive component as commercially available flexible shafts (which have to be one per finger to ensure dexterity through the independent finger movement) could not fit on the hand back. For these reasons, electric motors coupled with rigid transmissions were considered to pursue the requirements mentioned above.

Bearing in mind the torque required by each finger mechanism to exert at least 15 N on the finger (reported in Table 3.2), an interesting solution to implement was found in the micro metal gearmotors #4790, Low Power (LP) 6V, 380:1 from Pololu. Specifically, this brushed gearmotor enjoys extremely small sizes and weight, $26 \times 12 \times 10$ mm$^3$ plus a 10-mm driving shaft and 10 g, respectively. Such dimensions allow for placing them on the hand back in the longitudinal direction to the fingers (in Figure 3.8, they are inside the black modules). Its peak power is 0.27 W in operating conditions, while a no-load speed of 36 rpm and torque $\tau_{in}$ up to 284.49 Nmm (29 kgmm), measured at stall condition, characterize it. Since the actuator should provide at least 370.61 Nmm (the maximum value among those in Table 3.2), it was coupled with a 1:2-gear-ratio transmission. Considering the 110°-ROM for each finger proximal phalanx, except for the thumb for which it is lower (70°), such a transmission system allows to perform a whole finger opening or closing in 1.2 s.

Bevel gears with the mentioned above gear ratio were chosen for the target application since they ensured smaller overall sizes than other transmission systems capable of transmitting motion between orthogonal axes, as in the case study. After consulting different catalogues, a couple of steel (B50S 20*3) and brass (B50B 40*4) straight bevel gears from KG GEARS were chosen as driving and driven wheels, respectively. The reason for using wheels of different materials (steel and brass) is that this coupling provides a lower friction coefficient than the gear with both steel wheels. Figure 3.9 shows the proportioning parameters useful for the following dissertation, while the features of the chosen gear are reported in Table 3.4.

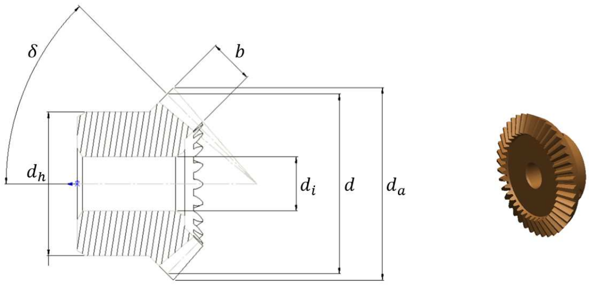


Figure 3.9: On the left, the main proportioning parameters for straight bevel gear: the cone angle $\delta$, gear width $b$, inner diameter $d_i$, hub diameter $d_h$, addendum diameter $d_a$, and reference diameter $d$ are highlighted; on the right, its CAD model.

| | Module $m$ | Material | N° of teeth | $d$ [mm] | $d_i$ [mm] | $d_h$ [mm] | $d_a$ [mm] | $b$ [mm] | $\delta$ |
|---|---|---|---|---|---|---|---|---|---|
| Driving wheel | 0.5 | C45 ($\sigma_{sn} = 345$ MPa) | 20 | 10 | 3 | 8 | 10.89 | 3.2 | 29° 8' |
| Driven wheel | 0.5 | Brass ($\sigma_{sn} = 335$ MPa) | 40 | 20 | 4 | 12 | 20.45 | 3.2 | 66° |

Table 3.4: The transmission gear features.

Due to the gear ratio other than 1, $\tau_{in}$ and $\tau_{out}$ correspond to the input and output torque to the transmission system the driving and driven wheels should withstand, respectively. According to calculations for tooth bending stress, the maximum transmissible torque $M_t$ by the wheel is evaluated as follows:

$$M_t = \frac{\sigma_{adm} m_m^2 bzy}{2\zeta} \tag{3.36}$$

in which $\sigma_{adm}$ is the specific material admissible stress, $m_m$ is the gear mean module, $y$ the Lewis coefficient, while $\zeta$ is equal to 1.4 for common gear. Specifically, the Lewis coefficient is evaluated as $y = 0.48 - \frac{2.87}{z'}$, in which $z' = \frac{z}{cos\delta}$ means the fictitious number of teeth, while the mean module measured at mid-tooth derives from $m_m = m - \frac{b}{z} sin\delta$. It is important to highlight that the transmissible torque is referred to the mean module since bevel gears, due to their conical shape, exchange forces that are considered applied at mid-tooth, thus in correspondence with the mean radius $r_m$. Specifically, bevel gears exchange

| | $F_{01x}$ [N] | $F_{01y}$ [N] | $F_{21x}$ [N] | $F_{21y}$ [N] | $F_{32x}$ [N] | $F_{32y}$ [N] | $F_{01} = F_{21} = F_{32}$ [N] |
|---|---|---|---|---|---|---|---|
| Thumb | 6.1693 | -38.8121 | -6.1693 | 38.8121 | -6.1693 | 38.8121 | 39.30 |
| Index | 21.4158 | -35.6803 | -21.4158 | 35.6803 | 21.4158 | 35.6803 | 41.61 |
| Middle | 3.4131 | -38.1865 | -3.4131 | 38.1865 | -3.4131 | 38.1865 | 40.27 |
| Ring | 3.0559 | -38.1865 | -3.0559 | 38.1865 | -3.0559 | 38.1865 | 38.30 |
| Small | 6.1693 | -38.8121 | -6.1693 | 38.8121 | -6.1693 | 38.8121 | 38.42 |

Table 3.5: Reaction forces at each finger mechanism joint and their module measured through the kinetostatic analysis in the worst load condition.

tangential, radial, and axial forces, as revealed by the following expressions, in which subscripts 1 and 2 indicate the driving and driven wheels, respectively, and the pressure angle $\alpha$ is equal to 20°:

$$F_t = \frac{\tau_{in}}{r_{m1}} = 65.80\ N \tag{3.37}$$

$$F_r = F_t \tan\alpha \cos\delta_2 = 10.12\ N \tag{3.38}$$

$$F_a = F_t \tan\alpha \sin\delta_2 = 21.70\ N \tag{3.39}$$

The overall actuation system can thus transmit torques up to $\tau_{out} = F_t r_{m2} =$ 562.55 Nmm.
Based on Equation 3.36, the driving wheel can transmit torque up to 577.82 Nmm, which is higher than the maximum deliverable by the actuator $\tau_{in}$ and also than that required by the finger mechanism so that it can exert at least 15 N on the finger (370.61 Nmm). Besides, the driven wheel can transmit $\tau_{out}$ since its maximum transmissible torque reached 939.7 Nmm, according to Equation 3.36. Therefore, the chosen gear was exploited for the target application.
It is important to point out that $\tau_{out} = 562.55$ Nmm derived from considering a torque $\tau_{in}$ measured at stall condition, which instead the actuator should reach as little as possible to avoid excessive overheating. However, from now on, all the components will be verified and designed cautiously to withstand the loads due to this condition in case it is reached. For this reason, the kinetostatic analysis presented in Section 3.1.1 was newly performed to evaluate the forces exerted on the finger mechanism bars when such torque was applied. Table 3.5 reports all the force components, following the outline shown in Figure 3.6, and their module. It is worth noting that the index-handling mechanism is subjected to the highest load than the other fingers. Thus, the components presented below are designed to withstand it.

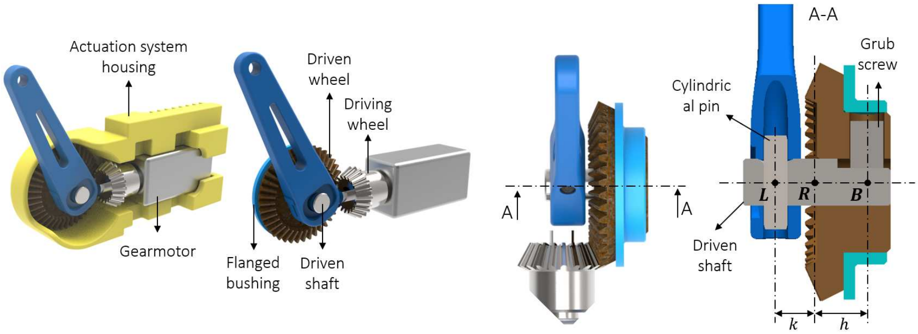


Figure 3.10: Actuation system arrangement: on the left, the actuation system components (gearmotor and gear transmission) placed in a housing designed for the purpose, and the flanged bushing to reduce friction among the parts; on the right, a sectional view of the driven shaft in which $L$, $R$, and $B$ represent points where forces due to the interaction with the finger mechanism, driven wheel, and support, respectively, are considered applied.

Forces exchanged by the wheels are then transmitted to a driven shaft, which in turn puts the finger-handling mechanism into rotation through a cylindrical pin. If the inner diameter of the driving wheel ($d_i = 3mm$) fits well with that of the actuator shaft, the driven one had to be designed for the specific application. Indeed, the inner diameter of the driven wheel dictates that of the driven shaft, at least in the connection area between them. However, it should also have a hole to house a cylindrical pin to put into rotation Link 1 of the linkage mechanism and a double flattening at the opposite side to make it integral to the driven wheel through two grub screws. Figure 3.10 shows how the mentioned components of the actuation system were assembled. A flanged bushing was placed among the driven wheel and actuation system housing to support the shaft loads and reduce friction between the two moving parts. This arrangement and strict size constraint above the hand led to a driven-shaft length of 12.6 mm. Due to its peculiar features, the driven shaft was designed as reported below and then realised by turning and milling. The design procedure results can be seen in Figure 3.11.

Figure 3.12 shows the loads outlined along the shaft for the stress analysis after returning the gear exchange forces to the shaft axis. Specifically, based on the *Transport Theorem*, the axial force $F_a$ produces a torque along the $y$-axis, which is equal to $M_{ay} = 185.57$ N while the tangential component $F_t$ determines

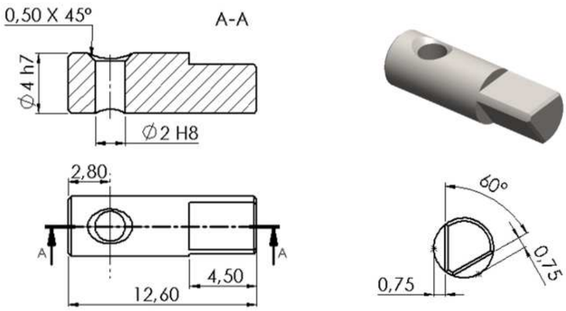


Figure 3.11: Technical drawing of the driven shaft and its CAD model resulting from the design procedure presented in this section.

the torque $\tau_{out}$, as evaluated above. Points $L$, $R$, and $B$ indicate where loads due to the finger-handling mechanism, wheel (its mean radius), and bushing reactions were applied, respectively.
The *Cardinal Equations of Statics* were applied to the force diagram in both planes by exploiting point $B$ as the reduction centre, as reported below:

$$\begin{cases} F_{10x} + F_r + R_{Bx} = 0 \\ F_a + R_{Bz} = 0 \\ C_{By} + M_{ay} - F_r h - F_{10x}(h+k) = 0 \end{cases} \tag{3.40}$$

$$\begin{cases} R_{By} + F_t + F_{10y} = 0 \\ C_{Bx} + F_t h + F_{10y}(h+k) = 0 \end{cases} \tag{3.41}$$

from which derives respectively that

$$R_{Bx} = 11.29\ N \tag{3.42}$$

$$R_{Bz} = -21.70\ N \tag{3.43}$$

$$C_{By} = -313.25\ N \tag{3.44}$$

$$R_{By} = -101.48\ N \tag{3.45}$$

$$C_{Bx} = -595.43\ N \tag{3.46}$$

Finally, it is also valid that $C_t = \tau_{out}$ due to the torque transmission, even if they are opposite in direction.

Normal, shear and bending loads were evaluated along the shaft while con-

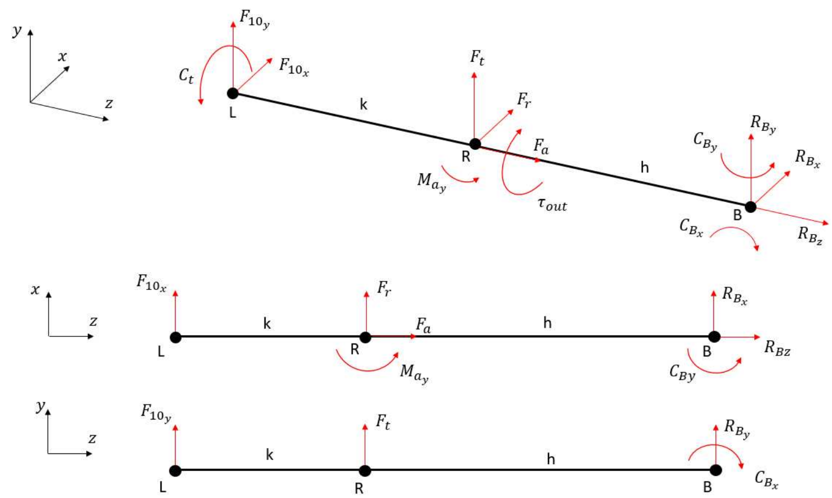

Figure 3.12: Schematic load representation of the driven shaft: on the top, the 3D representation, while on the bottom, the loads decomposition into the $xz$ and $yz$ planes.

sidering forces at the left of each section as detailed in Table 3.6, while Figure 3.13 shows the matching diagrams. Table 3.7 reports the total loads evaluated on the reference points. Section $R$, in which loads due to the driven wheel are applied, seemed the most stressed as the loads on it are higher than those measured in the other sections. However, all three sections were analysed because they should present specific features to transmit motion from the driven wheel to Link 1 of the finger mechanism.

Immediately analysing the most stressed section, normal, shear, bending, and torque loads were detected. Section area, bending and torsion strength modulus may be evaluated as $A = \frac{\pi D^2}{4}$, $W_f = \frac{\pi D^3}{32}$, and $W_t = \frac{\pi D^3}{16}$ respectively, in which the diameter $D = 4\ mm$ imposed by the chosen wheel was considered for first calculations. Given these premises, normal and shear stresses resulted

| | | N | T | M |
|---|---|---|---|---|
| $xz$ plane | $z \in [0, k]$ | 0 | $F_{10x}$ | $-F_{10x}z$ |
| | $z \in [k, k+h]$ | $F_a$ | $F_{10x} + F_r$ | $-F_{10x}z - F_r(z-k) + M_{ay}$ |
| $yz$ plane | $z \in [0, k]$ | 0 | $F_{10y}$ | $F_{10y}$ z |
| | $z \in [k, k+h]$ | 0 | $F_{10y} + F_t$ | $F_{10y}z + F_t(z-k)$ |

Table 3.6: Expressions for normal, shear, and bending loads along the shaft reported for both planes.

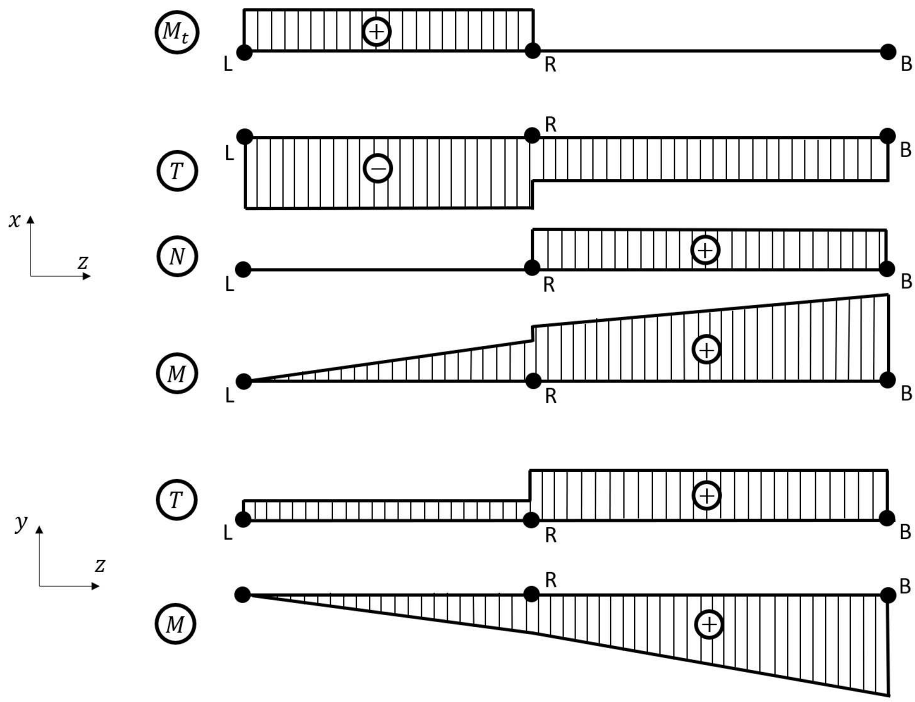


Figure 3.13: The stress diagrams of the driven shaft: from top to bottom, torsional stress due to the applied torque, shear, normal, and bending stresses in the $xz$ plane, and finally, shear and bending stresses in the $yz$ plane, in which no normal forces were measured.

| | $N$ [N] | $T$ [N] | $M$ [Nmm] | $M_t$ [Nmm] |
|---|---|---|---|---|
| $L$ | 0 | 41.61 | 0 | 562.55 |
| $R$ | 21.70 | 102.10 | 289.60 | 562.55 |
| $B$ | 21.70 | 102.10 | 672.80 | 0 |

Table 3.7: Total normal, shear, bending and torque loads evaluated in points $L$, $R$, and $B$ of the driven shaft.

as follows:

$$\sigma = \sigma_N + \sigma_M = \frac{N_R}{A} + \frac{M_R}{W_f} = 186.09\ MPa \tag{3.47}$$

$$\tau = \tau_{shear} + \tau_{torque} = \frac{T_R}{A} + \frac{M_{tR}}{W_t} = 44.77\ MPa \tag{3.48}$$

Based on Von Mises criterion, the equivalent stress resulted as

$$\sigma_{eq} = \sqrt{\sigma^2 + 3\tau^2} = 207.42\ MPa \tag{3.49}$$

For what concern section $B$, it is worth noting that the shaft requires in this region (as shown in Figure 3.11) a double flattening for making the wheel integral to the shaft through two grub screws (M3 $\times$ 4), thus allowing for the motion transmission between these two entities. Due to the particular shape of this section (Figure 3.11), an equivalent circular section, meaning that its area was equivalent to that under study, was considered for calculations.
The shaft in this section is subjected to normal, shear, and bending loads, as reported in Table 3.7. Normal and shear stresses are evaluated as follows:

$$\sigma = \sigma_N + \sigma_M = \frac{N_B}{A} + \frac{M_B}{W_f} = 189.47\ MPa \tag{3.50}$$

$$\tau = \tau_{shear} = \frac{T_B}{A} = 11.78\ MPa \tag{3.51}$$

Considering that torque stress is absent in this section, the equivalent stress $\sigma_{eq}$, measured as in Equation 3.49, equals 190.57 MPa.

Finally, section $L$ is featured by a hole along the entire section itself, as shown in Figures 3.10 and 3.11, in which the cylindrical pin to transmit motion to Link 1 of the finger-handling mechanism houses. Thus, calculations for designing the

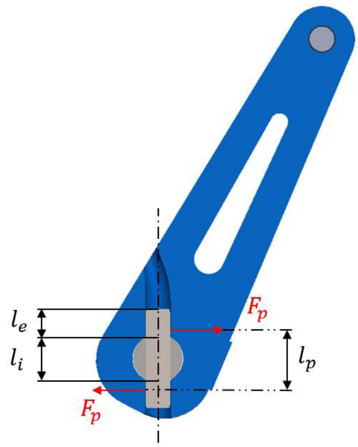


Figure 3.14: A sectional view of the driven shaft, cylindrical pin, and Link 1, in which the couple of forces $F_p$ due to $\tau_{out}$, length of the pin inner the shaft $l_i$, outer the shaft $l_e$, and distance between the forces' application points $l_P$ are shown.

cylindrical pin are required to evaluate the equivalent stress in this section.
Due to overall size constraints, an 8-mm-length cylindrical pin was considered for the application. Figure 3.14 reports a sectional view, including the pin, shaft, and Link 1, in which a schematic representation of the loads is shown. The driven shaft transfers the torque to Link 1 through a couple of forces $F_p$. A perfect fit was assumed between the shaft and pin. Given a non-constant pressure distribution between the pin and Link 1, with maximum values at the maximum shaft radius, the force resulting from pressures established between the two parts was considered to be applied at one-quarter of the length of the pin outside the shaft. Due to this assumption, the force $F_p$ can be evaluated as $F_p = \frac{M_t}{l_p} = 112.51$ N, in which the distance between its application points was measured as $l_p = l_i + \frac{1}{2}l_e = 5$ mm. The cylindrical pin has to withstand shear and bending loads. Thus, its diameter must be defined based on the minimum

value achieved through the following equations:

$$d > \sqrt{\frac{4F_p}{\pi\tau_{adm}}} \tag{3.52}$$

$$d > \sqrt[3]{\frac{32M_p}{\pi\sigma_{adm}}} \tag{3.53}$$

in which $M_p$ indicates the torque due to $F_p$ referred to the embedded length, while $\tau_{adm}$ and $\sigma_{adm}$ depend on the chosen material. Assuming to employ stainless steel (AISI 303) with yield tensile strength $\sigma_{sn}$ of about 200 MPa and a safety factor of 1.5, the minimum diameter resulting from the above equations is 1.36 and 1.62 mm, respectively. Thus, a 2-mm-diameter and 8-mm length cylindrical pin (HDP 2-8-A1) from Accu Delivered was chosen for the application and considered to verify section $L$ of the driven shaft.

Table 3.7 reveals that this section is loaded by shear and torque forces. However, in the worst loading condition analysed, the shear force is right along the cylindrical pin so that it can be neglected for shaft calculations. In particular, it is worth noting that the pin is mounted on the shaft so that it is vertical when the finger is in the rest position ($\theta_{MCP} = 0$), thus allowing for the passive a/a movement as well. Due to this assumption, only torque loads were considered to evaluate the total shear stress, as reported below:

$$\tau = k_t \frac{M_{tL}}{\frac{\pi D^3}{16} - \frac{dD^2}{6}} = 81.17\ MPa \tag{3.54}$$

in which $k_t$ is a stress-concentration factor that was applied since the hole produces a tension intensification in this region; it was derived from appropriate tables under the specific load condition and equals 1.04.

As expected, section $R$ resulted in the most stressed one. Given the equivalent stress measured in the three sections, a standard stainless steel (AISI 316) with admissible stress equal to 250 MPa was considered for the application. This resulted in a safety factor greater than 1.21, which is considered enough since it is evaluated at the worst load condition, matching the actuator stall, which should be reached as little as possible and, if reached, does not persist throughout the device's use. According to such calculations, the 4-mm-diameter driven shaft withstands the loads it is subjected to, and no section increases are needed.

As mentioned, a flanged bushing was introduced to hold the driven shaft and reduce friction issues with the actuation system housing, in which it has to be

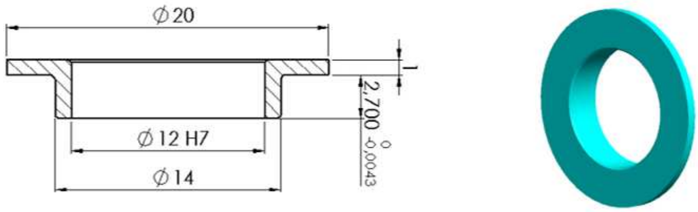


Figure 3.15: Technical drawing of the flanged bushing, on the left, and its CAD model, on the right.

mounted with interference. A flanged bushing from IGUS (W300 WFM-1214-04), made of iglidur® W300, was initially chosen for this purpose, considering that the driven wheel geometry dictates its inner diameter $d_h = 12$ mm and length $l = 4$ mm. Shear and bending loads were considered for calculations, as those that the bushing should withstand. Precisely, it was verified that the specific pressure due to the shear load $T$, measured as $p = \frac{T}{d_h l}$, and bending stress due to the matching load $M$ and shear one $T$ evaluated in section $B$ are less than the admissible value declared by the manufacturer, 60 and 125 MPa, respectively. However, it has been replaced by a brass bushing, specifically designed (Figure 3.15), due to the excessive clearance the IGUS bearing left between itself and the driven wheel, which in turn caused a lack of stability. The dimensions of the IGUS bushing were preserved in the brass one, except for the length reduced to 3.7 mm, consistent with the module's overall dimensions.

### 3.2.2 Finger-handling module

The actuation system analysis allowed for determining the torque the system can transmit and, thus, the forces the finger-handling mechanism has to withstand. Reaction forces due to the transmissible torque $\tau_{out} = 562.55$ Nmm were evaluated by reversing the kinetostatic analysis proposed in Section 3.1.1, and they are summarised in Table 3.5.
Starting from the previous section's achievements, the finger-handling mechanism, particularly its components, was developed. This section focuses on describing them and, finally, their embodiment.
From what is inherited from Section 3.1, the mechanism bars (meaning Link 1, Link 2, and Link 3) are parts of the rigid architecture to which the distal-phalanx

Figure 3.16: Different views of Link 1 of the finger-handling mechanism: side and top views on the left, sectional view on the centre, and axonometric view on the right.

EE is added. All these components were 3D printed in ABS-CF10, which combines ABS strengths with the carbon fibre stiffness, resulting in a thermoplastic stiffer and stronger than standard ABS 3D printing material. Specifically, they were 3D printed with a Stratasys F370 3D printer, which works with Fused Deposition Modeling (FDM) technology.

**Link 1**

Figure 3.16 shows some views of Link 1, in which the distance between the two holes at the ends corresponds to $a$, the first component of vector $\mathbf{x}$, defined in Section 3.1.1. This bar design mainly derives from that of the driven shaft and the need for the cylindrical pin that makes it integral right to the shaft. However, the pin has not only this purpose since its relative rotation to Link 1 was not fixed, but left free to introduce an additional DOF allowing for the passive a/a movement. Such a movement is fundamental for hand functionalities. In addition, leaving it passive prevents wrong and painful movements and improves the mechanism compliance with the finger. Nonetheless, adding a DOF for each finger might produce cumbersome architecture no more so portable and wearable.

Given these premises, the novel finger-handling mechanism was provided of this additional DOF through the straightforward cylindrical pin, assuming that a healthy hand can adduce and abduce, especially in the rest position, while the capability worsens during hand closing. Therefore, the orientation of the pin housing was determined so that it was vertical when the hand was resting, i.e., $\theta_{MCP} = 0°$. By doing so, the user can perform a/a movement when the hand is open, and the pin axis coincides with that of the MCP joint. During hand closing, the axes' correspondence is no longer verified since, while Link 1 rotates around the cylindrical pin, the pin rotates around the driven shaft. Although

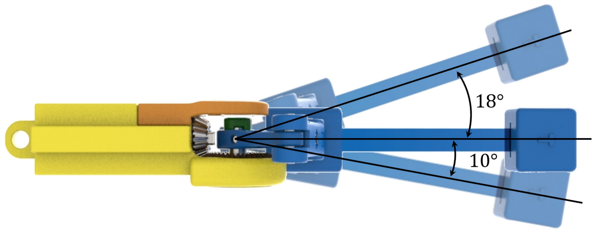


Figure 3.17: The a/a ROM achievable by the finger-handling mechanism.

this motion is reduced during hand closing, the assumption evidence led to consider the straightforward solution rather than introducing maybe more precise, but also more complex and cumbersome systems to implement this movement. Besides, another aspect has to be pointed out. Due to the stringent dimensional constraints on the hand back and the arrangement chosen for the actuation system (shown in Figure 3.10), which was still the one that required the minimum sizes, the a/a movement the finger-handling mechanism allows is not symmetrical to the finger, but it evolves as in Figure 3.17. Its ROM is higher on the free side rather than where the driven wheel is housed. It was, therefore, necessary to consider this asymmetry relating to the actual finger movement. Observing a hand in a rest position with the fingers arranged parallel to each other revealed the limited possibility of adduction and the fact that the index abduces in the opposite direction than the middle, ring, and small. Thus, the modules for these last fingers were assembled precisely counter to the index, as shown below. This choice allows matching the higher a/a ROM side with the abduction direction for all the fingers. For what concerns the thumb, its module was assembled as the index to give more freedom to the opposition movement and favour compliance, even if the a/a ROM around the MCP joint is almost zero.
For all these reasons, the hole for the driven shaft in Link 1 was appropriately shaped to not limit the a/a movement, as visible in Figure 3.16.

In addition, a further housing for the magnet (RMM3010A1A00 from RLS) required by the encoder chosen for the application, which will be introduced below, has to be fixed at the free end of the driven shaft, as shown in Figure 3.18. Specifically, the considered magnet (3 mm in diameter and 1 mm in thickness) was unsuitable for ferrous shafts. Thus, a housing to hold the magnet and be embedded in the shaft was tailored. For this reason, Link 1 was modelled to prevent interference with this component during the a/a movement, as visible


Figure 3.18: The housing designed for the magnet to be installed in the shaft: on the left, its front and back views with indications of overall sizes; on the centre, the magnet with its housing arranged on the shaft, and on the right, a view of the actuated joint of Link 1.

on the top left view in Figure 3.16. Instead, the view in the centre reveals the through-hole to house the cylindrical pin, ensuring the coupling between the pin and shaft can be disassembled.

#### Link 2

From Figure 3.19, some peculiar features of Link 2 emerged. It is worth noting that one end of the spring is attached to this component by a screw. The slight step on the bottom side of Link 2 in the top left view represents a stop for the spring and helps its thrust. Link 2, of length $b$ (as the second component of vector $\mathbf{x}$), consists of two asymmetric components, which are connected by form fit coupling, and subsequently fixed by the screw through the two components employed for the spring connection. The nut house is embedded in one of the two components to avoid exposed metal parts and improve safety. To add bearings among the two rotating bars, the holes made in Link 1 and Link 3 must have a higher diameter than the joints.

#### Link 3

Figure 3.20 shows how Link 3 evolves over time. Initially, the component had the geometry shown on the top row of the figure, which was then modified to

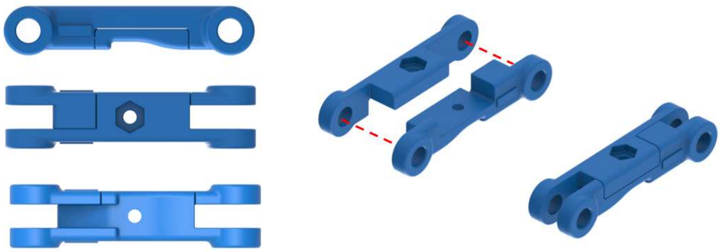

Figure 3.19: Different views of Link 2 of the finger-handling mechanism: from the top left, side, top, and bottom views, on the centre, the axonometric views of the two components of Link 2, and on the right, the definitive Link 2.

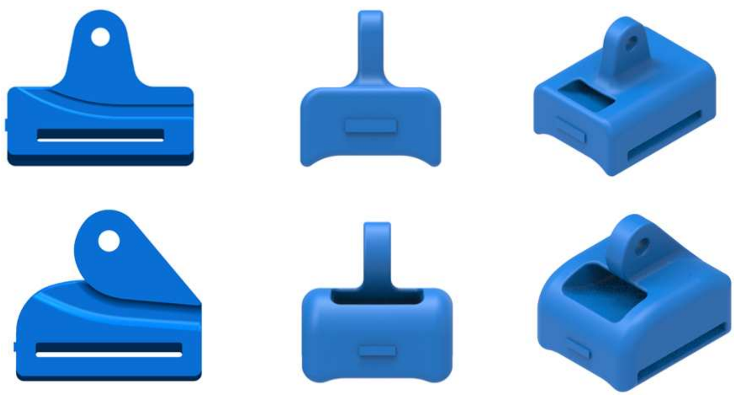

Figure 3.20: Evolution of Link 3 of the finger-handling mechanism: on the top row, the first version of Link 3, and on the bottom row, its second version; for each of them, from the left, a sectional view showing the spring housing, on the centre, a frontal view, and on the right, an axonometric view shows the definitive Link 3.

enlarge the house for the flat spring sliding, resulting in the geometry on the bottom row. Such a modification aims to increase the flat spring inlet region at Link 3 so as not to fix a very tight curvature but rather to leave it wider. For both versions, the distance between the hole and component base corresponds to $c$, the third component of vector $\mathbf{x}$. A further transversal through-hole was added for a Velcro strap to fix the component to the proximal phalanx.

### Distal phalanx EE

Figure 3.21: Views of the distal phalanx EE: on the left, a side and bottom views, on the centre, an axonometric view of the two components, and on the right, the definitive distal phalanx EE.

The soft architecture EE acting on the distal phalanx is also a rigid component. It consists of two parts, visible in Figure 3.21, which must be interlocked while the flat spring is secured to the component with a bolt. The bottom view on the left reveals the screw house, while the one in the centre shows a slope in the spring fastening area designed to favour its bending. As for Link 3, a through-hole was added to house a Velcro strap to make integral the component to the distal phalanx.

### FEM analysis

FEM analyses were performed during the design phase to detect the geometry of each bar of the finger-handling mechanism requiring the least overall sizes while withstanding the loads to which each of them is subjected. The analyses were carried out for all the components in the worst loading condition due to the actuation system implemented on the mechanism. Indeed, verifying the components' strength is necessary even when the actuation system transmits the maximum torque. It is worth noting that, due to the different bar lengths of each finger, the worst loading condition is not the same for all fingers and can occur at different ROM levels. In particular, the thumb, index, and small reached this condition at the complete finger opening, while the middle and ring at complete closing. For the sake of brevity, only the analyses performed on the index mechanism bars will be presented in detail since they resulted in the most stressed one, as derived from Table 3.5 in Section 3.2.1. However, the

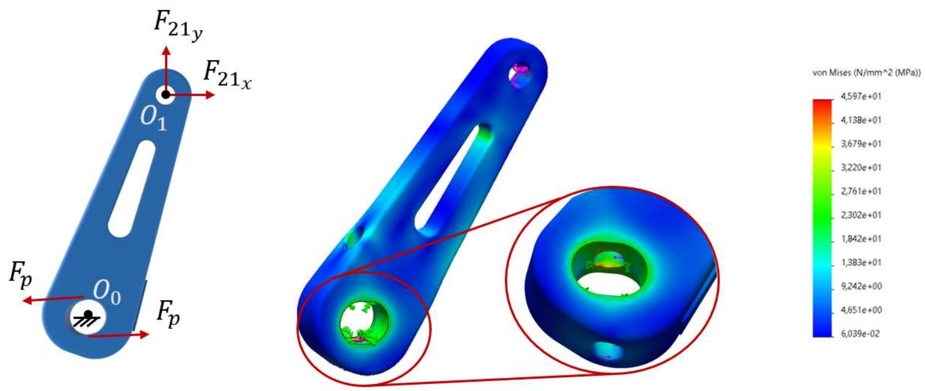


Figure 3.22: Arrangement of forces and Von Mises stress resulted from a static analysis on the index mechanism Link 1 and a focused view on the region where the maximum stress is measured.

same procedure was followed for the other finger mechanism bars, and similar trends were found for their stresses.

The Simulation tool in the SolidWorks environment was exploited to perform static analyses for each bar. Indeed, the tool first allows the choice of the type of analysis, and then constraint (e.g., interlock, hinge, slide) and load (e.g., force, torque) conditions can be set. The loads applied for these analyses are evaluated in the worst loading condition when the actuator reaches the stall condition and are reported in Table 3.5. Once the load conditions have been defined and the material has been chosen, it is possible to proceed with the component mesh, which means a triangulation that allows the structure to be discretised into many small elements on which the stresses, deformations, and displacements are calculated and then reintegrated for the entire structure. A parameter that can influence the analysis computational cost is the mesh density, which in this case can be very fine given the bar's simple geometry, still allowing analysis in less than 2 minutes.

Regarding Link 1, an interlock constraint was set in correspondence with the actuated joint ($O_0$), $F_{21x} = -21.42$ N and $F_{21y} = 35.68$ N are applied to the other joint ($O_1$), while $F_p = 112.15$ N was applied as shown in Figure 3.14 due to the torque transmission through the cylindrical pin. Figure 3.22 shows the arrangement of such constraints and loads on the left, while on the right, it reports the stresses according to Von Mises criterion resulting from the static

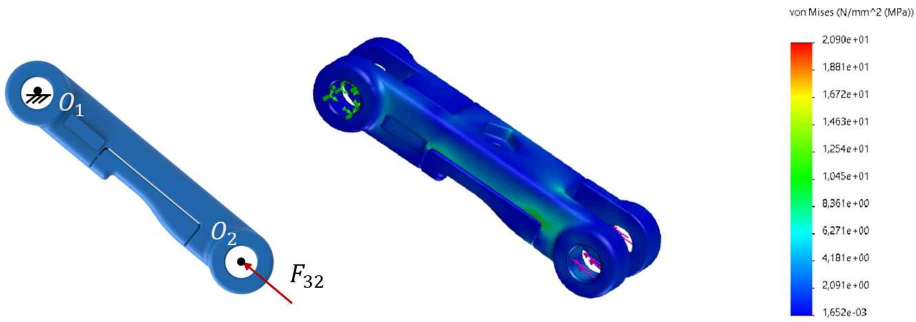


Figure 3.23: Arrangement of forces and Von Mises stress resulted from a static analysis on the index mechanism Link 2.

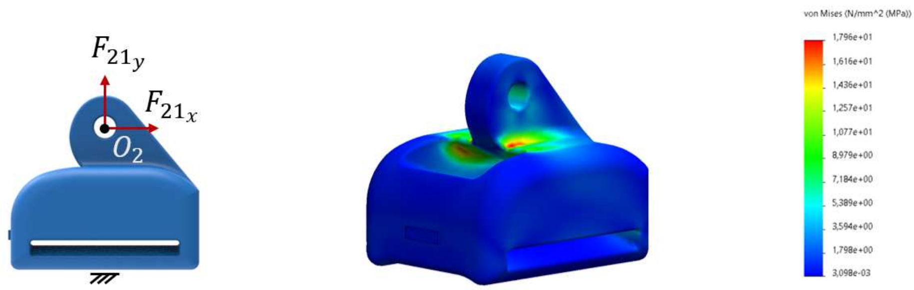


Figure 3.24: Arrangement of forces and Von Mises stress resulted from a static analysis on the index mechanism Link 3.

analysis. Attention is captured by the maximum measured stress, reaching 45.97 MPa, higher than the tensile strength of ABS-CF10 3D printing material equals 37.7 MPa. Nonetheless, it is worth noting that the high value is registered in correspondence with an edge (Figure 3.22), while the stresses drop below the material strength, reaching values of about 30 MPa, by moving a little away from the edge.

Figure 3.23 shows instead the arrangement of constraint and loads for the static analysis performed on the overall Link 2 after adding contact settings to prevent the interpenetration of the parts. It is worth noting that the force applied to the joint $O_2$ corresponds to the modulus of the vector sum of the two components $F_{32_x} = -21.42$ N and $F_{32_y} = 35.68$ N. The maximum stress mea-

| | Thumb | Index | Middle | Ring | Small |
|---|---|---|---|---|---|
| Link 1 | 31.44 | 30.06 | 31.26 | 31.66 | 28.06 |
| Link 2 | 21.84 | 20.9 | 24.45 | 25.73 | 25.61 |
| Link 3 | 19.59 | 17.96 | 16 | 11.33 | 8.61 |

Table 3.8: Maximum stresses $\sigma_{max}$ [MPa] measured on Link 1, Link 2, and Link 3 of all the fingers by performing static analyses.

| Thumb | Index | Middle | Ring | Small |
|---|---|---|---|---|
| 2.85 | 2.13 | 1.92 | 4.78 | 3.9 |

Table 3.9: The loading factor measured through buckling analyses performed on Link 2 of each finger-handling mechanism.

sured is 20.9 MPa, ensuring a 1.8 safety factor referring to the ABS-CF10 tensile strength. Due to the loading condition, a buckling analysis was also performed, resulting in a load factor of 2.131. Static analyses were also performed on each component of Link 2, resulting in 1.3 and 1.6 safety factors, respectively.

Finally, the constraint and loads setting for the static analysis of Link 3 and the matching results are reported in Figure 3.24. $F_{23x} = 21.42$ N and $F_{23y} = -35.68$ N were applied to the joint $O_2$, after interlocking its base, which is the mechanism contact with the finger. Although the peculiar geometry of the region highlighted in Figure 3.24, featured by thin thickness, the maximum stress from the analysis ensures a 2.1 safety factor.

For completeness, Table 3.8 shows the maximum stress values measured in the analyses performed on the bars of each finger mechanism. Since Link 1 of each exhibited stresses beyond the material strength that were measured at edges due to the stress intensification in these areas, stress values measured away from the edges to reduce these effects are shown in the table. Table 3.9 reports instead the loading factor resulting from the buckling analyses performed on Link 2 of each finger mechanism.

### Finger-handling module embodiment

The finger-handling module resulting from the design procedure described in the previous sections is shown in Figure 3.25. The figure reports the index module embodiment, as it can be repeated similarly for all other fingers.

Regarding the finger-handling mechanism, the rigid bars were coupled by ex-

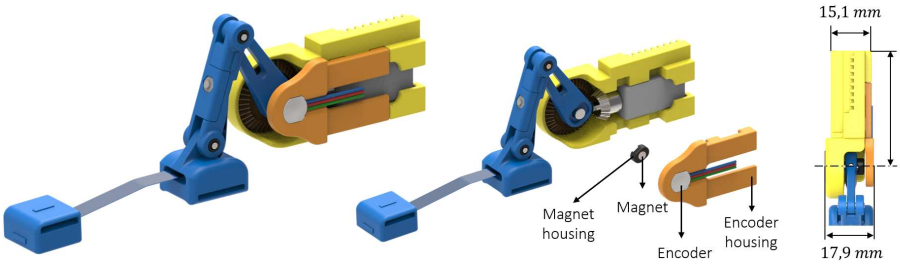


Figure 3.25: The finger-handling module: on the left, the index mechanism embodiment; on the centre, an exploded view showing the encoder, magnet and their matching housings; and on the right, the overall sizes of its actuation system.

ploiting pins as joints after introducing cylindrical bushings to reduce friction among the parts. As pins, HDP-2-10-A1 from Accu Delivered in AISI 303 were chosen and verified to withstand shear and bending loads (with a 1.51 safety factor) due to the forces $F_{21} = F_{32} = 41.61$ N acting on $O_1$ and $O_2$ joints, respectively.
Cylindrical bushings in iglidur® G (GSM-0203-03) with a 2-mm inner diameter, 3-mm outer diameter, and 3.5-mm length were introduced rather than radial ball bearings to keep sizes as low as possible. Verification, in this case as well, is carried out by evaluating the specific pressure, resulted less than the admissible value declared by the manufacturer, which equals 80 MPa.
Regarding the soft architecture, a flat spring in spring steel with section $0.3 \times 6$ mm$^2$ and a longitudinal slot 3 mm wide was initially considered for the application, and its length was measured in the CAD model and approximated to the nearest integer. Specifically, it was determined in the case with the finger is in the rest position ($\theta_{MCP} = \theta_{PIP} = \theta_{DIP} = 0°$), and depends on the specific user hand anatomy and mechanism bars length. Table 3.10 summarises all the finger-handling mechanism spring lengths. The spring has two holes at its ends to fix it to Link 2 and the distal-phalanx EE through little screws (M2).

After assembling the finger-handling mechanism, it can be connected to the actuation system through the cylindrical pin, resulting as in Figure 3.25. In addition, the figure reveals the presence of the magnet and its housing required for the encoder functioning. In particular, a linear-voltage non-contact miniature rotary encoder from RLS (RM08VB0010B02L2G00) and its magnet

| | Thumb | Index | Middle | Ring | Small |
|---|---|---|---|---|---|
| $l_s$ [mm] | 58 | 80 | 90 | 88 | 75 |

Table 3.10: The spring length $l_s$ for all the fingers.

(RMM3010A1A00) were added to each finger module to provide a direct measure of the finger f/e angle. By placing it in the axis with the driven shaft, it may provide measurements of the angle $\alpha_1$, which in Equation 3.21 was expressed as a function of $\alpha_0$, indicating the proximal phalanx f/e since directly related to $\theta_{MCP}$. Therefore, by reversing Equation 3.21, information about the finger f/e can be derived from encoder measurements and exploited for the control strategy, which has not been a study subject in this work. It is worth noting that each module includes an encoder, meaning that the angular position of each finger proximal phalanx can be derived. Thus, each finger can be separately controlled towards the independent finger movement that improves dexterity.
According to its specification, the magnet should be placed 0.5 mm axially from the encoder to achieve optimal measurements. Therefore, the encoder housing shown in Figure 3.25 was designed to meet such a requirement.
All the above mentioned components and their arrangement allow the finger module overall sizes to be kept low. In particular, the dimensions in correspondence with the driven shaft axis (17.9 mm) or the actuation system thickness (15.1 mm), as revealed by Figure 3.25, allow for repeating the same module for all fingers.

### 3.2.3 Hand exoskeleton embodiment

As mentioned in the previous section, the overall sizes of the single module allow placing all the finger modules on the hand back. The finger module housings shown in Figure 3.26 were designed for this purpose. As the figure reveals, the main housing was intended for the index, middle, ring, and small modules, while a separate housing was dedicated to the thumb module to disengage it from the other fingers and leave free its circumduction movements. Each module placement, differing based on the finger abduction direction, emerges from Figure 3.26.

The housings consist of two parts equipped with a magnetic coupling for easy assembly and disassembly. This choice is associated with the presence of a rack-and-pinion mechanism, which otherwise could not be assembled into the housing. This mechanism was introduced as a micro-regulation system for the

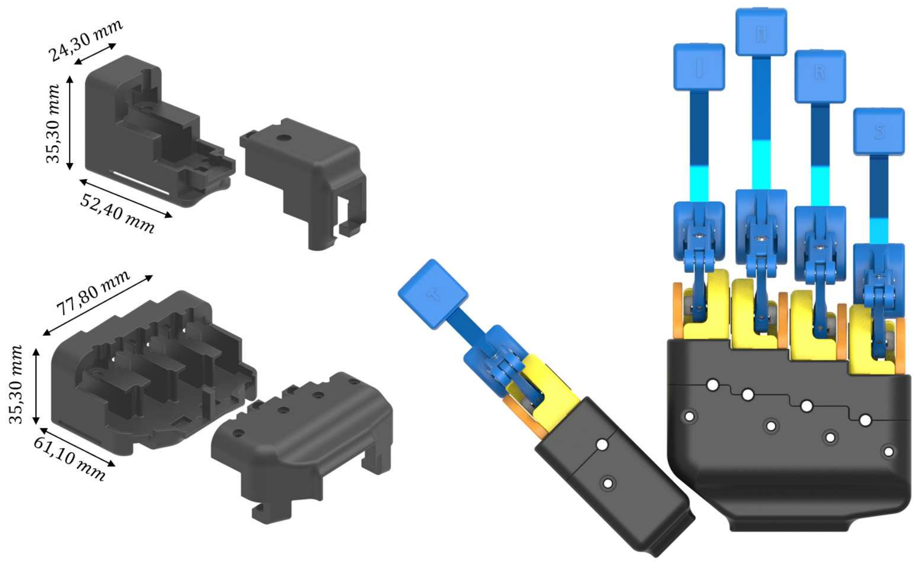


Figure 3.26: On the left, the housings for the thumb (top row) and the other finger modules (bottom row) in which overall dimensions are highlighted, and on the right, a top view of the hand exoskeleton where the module's placement is evident.

finger-handling mechanism position. Indeed, the linkage mechanism actuated joint must be placed right above the finger MCP joint so that the mechanism itself produces the *desired trajectory*, as mentioned in Section 3.1.1, and ensure the required kinematic accuracy. In the case of misalignment, the accuracy reduces as well as the ROM achievable by the mechanism. To prevent this issue, the rack and pinion mechanism was introduced, as shown in Figure 3.27. This micro-adjustment system, in addition to the kinematic optimisation presented above, gives the device an adaptability level that makes it suitable for hands of similar size without resorting to a new optimisation. Specifically, the rack was designed integral to the actuation system housing, while the pinion was made integral to a grub screw to straightforwardly rotate through a hex key to adjust the finger module position. A pinion-rack mechanism is introduced for each finger so that each can be adjusted independently.
The rack-and-pinion mechanism was designed for a 10-mm stroke $s$, which is

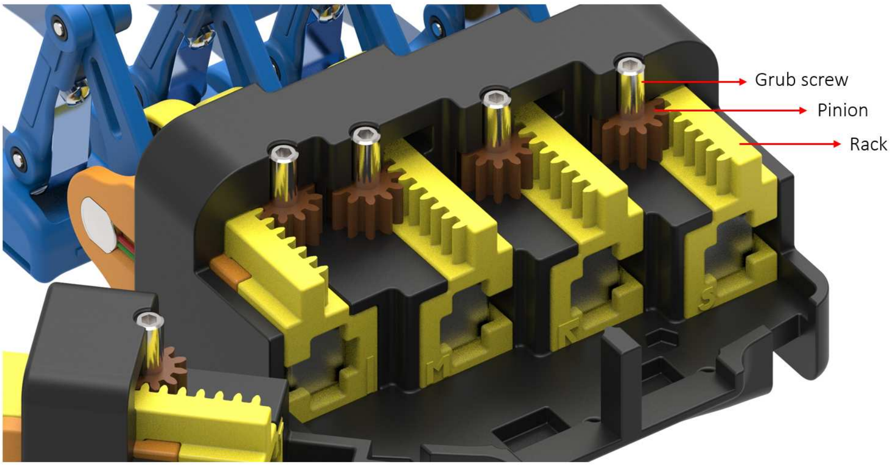


Figure 3.27: The rack-and-pinion mechanism in the overall device model.

considered an acceptable value for the needed regulation. The mechanism was initially designed to be 3D printed in ABS-CF10 due to its remarkable mechanical features. Given these premises, the mechanism was proportioned assuming a module $m$ of 0.8 and a number of teeth $z_p$ equals 11 for the pinion, according to which the revolution number $n$ needed to achieve the fixed stroke can be evaluated as $n = \frac{s}{z_p p} = 0.36$, where $p = \pi m$ indicates the pinion pitch. The rack number of teeth $z_r$ required for the measured revolution number is $z_r = \frac{z_p(360n)}{360}$, which appropriately increased and multiplied by the pitch reveals the minimum rack length to achieve this stroke, resulting in $\simeq 17.6$ mm. Due to the available dimension on the actuation system housing, this length was increased up to 21 mm.
Considering the module and teeth number assumed, the pinion reference diameter $d$ is 8.8 mm. The transmissible torque by the pinion was evaluated as $M_t = \frac{\sigma_{adm} m^2 bzy}{2} = 85.60$ Nmm, in which the tooth width $b$ is assumed equal to 6 mm, while the Lewis coefficient $y$ is 0.219. The resulting value is largely enough to regulate the module of mass 55 g since, considering a friction coefficient of 0.4 due to possible 3D printed irregular surfaces, a 0.95-Nmm torque would be required under these conditions. Nonetheless, the rack dimensions were not reduced so as not to compromise the 3D printing quality.
To further reduce the overall sizes, a commercial brass alternative from the

| | $m$ | $z$ | $d$ [mm] | $b$ [mm] | $M_t$ [Nmm] |
|---|---|---|---|---|---|
| ABS-CF10 | 0.8 | 11 | 8.8 | 6 | 85.60 |
| Brass | 0.3 | 20 | 6 | 3.2 | 216.44 |

Table 3.11: Comparison between the brass and ABS-CF10 pinions.

KG GEARS catalogue was also identified that would still allow the adjustment while ensuring lower vertical sizes above the hand. The features of brass and ABS-CF10 pinions are compared in Table 3.11.

Some considerations can be made about the finger module housing. Firstly, it is worth noting that the modules' housings are parallel and do not grow along the hand metacarpals due to their overall sizes. The possibility of placing the actuation system directly on this component rather than in the additional dedicated housing was also considered. This solution, however, would have made assembly more complicated and would not have allowed for introducing the finger-handling mechanism adjustment system, which, on the other hand, is essential to ensure kinematic accuracy. Secondly, this housing is tailored to the specific user hand anatomy so that the transversal distance between the MCP joints matches and, once the finger modules are placed, each driven shaft is as far above the MCP joint as possible. Then, the fine adjustment is delegated to the rack-and-pinion mechanism. Nonetheless, aiming at testing the device on multiple people, such a component can be designed for sizes, on which the linkage-mechanism bars can also be kinematically optimised so that a single adjustable device can be used.

After describing the actuation system, all the components along the driven shaft axis, and the rack-and-pinion adjustment system, the geometry of the actuation system housing is almost completely defined. Figure 3.28 shows some views of this component. The four indentations along the actuator housing need to be form-fitted to the encoder housing and to close the finger module. Mechanical stops in this housing frontal area should be emphasised since they especially avoid an excessive linkage-mechanism bending beyond the desired range, which would bring the mechanism into a singularity condition. Since the Link 1 ROM is different for all the fingers, an actuation system housing with different mechanical stops was designed for each finger.

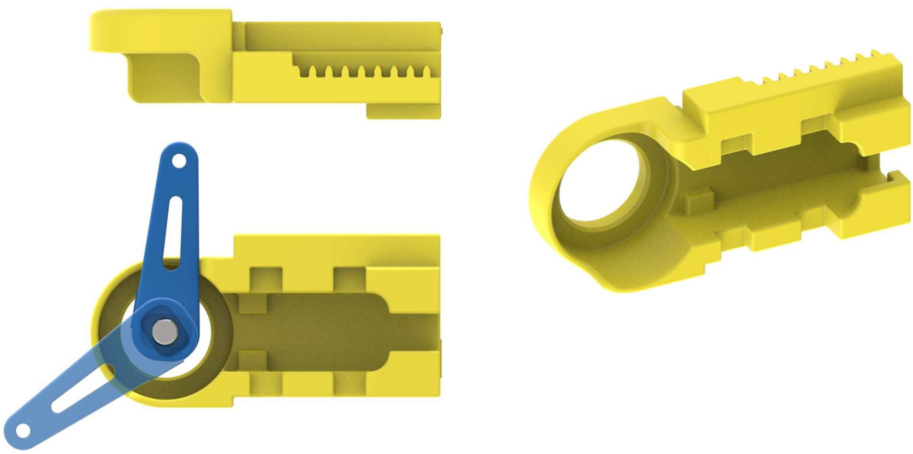

Figure 3.28: The actuation system housing of the index module: on the top left, its top view, on the bottom left, a frontal view, in which the mechanical stops limiting the Link 1 extreme position are highlighted, and, on the right, an axonometric view of the component.

#### Electronic components

This section has the sole scope of presenting the electronic components embedded in the device, which were exploited during the experimental test sessions reported in the following chapter.

Figure 3.29 reveals a backside area of the thumb and other finger module housings engaged with boards to which encoders and motors are connected. Respectively, one (RJ12) and two (RJ45) connectors are soldered to these boards, allowing cable communication with the hand exoskeleton secondary module (Figure 3.30). Here, the main electronic components are arranged, except for encoders, which are housed in the hand exoskeleton main module. The RJ12 connector is enough for managing the thumb module alone due to the lower number of cables involved than the other finger modules.

The hand exoskeleton secondary module, which has to be placed on the upper arm, encloses the power supply system, and a Printed Circuit Board (PCB) integrating all the other electronic components: in Figure 3.30 an outline of the board top side, including the power button, USB-C for charge and data transfer, and LEDs for visual feedback, is visible; the bottom side houses the

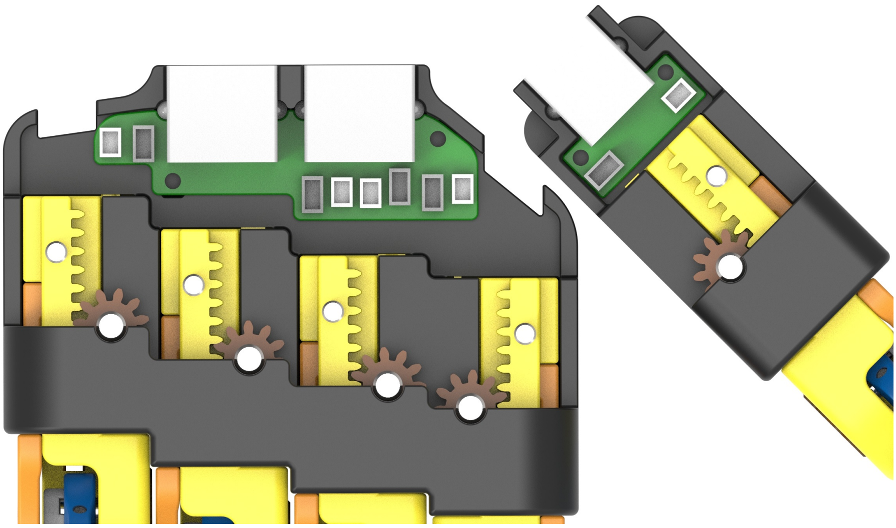

Figure 3.29: A view of the finger modules housing in which first electronic connections are shown.

motor drivers and microcontroller.

Referring to those components already mentioned in this chapter, the chosen encoders from RLS (RM08VB0010B02L2G00) require a supply voltage of 5 V while consuming a minimum current value equal to 0.26 mA. They have three AWG30 cables for ground, supply, and analogic relative angular position signal. Dual motor drivers (TB6612FNG) from TOSHIBA ($8.3 \times 7.6 \times 1.6$ mm$^3$) were considered to control the gearmotor included in the novel design (#4790 LP 6V from Pololu), which in stall conditions consumes up to 0.36 A. In particular, with a supply voltage of 3 V and a current consumption of 1.8 mA, these drivers can independently control two bidirectional DC motors, thus allowing to exploit only three drivers to manage the five gearmotors involved in the hand exoskeleton.

In addition, the device is provided with a low-cost ESP32-S3-WROOM-1 developed by Espressif Systems. It is integrated with Wi-Fi and Bluetooth, allowing wireless communications preferable in wearable robotic devices to avoid additional annoying cables. Its dimensions ($25.5 \times 18 \times 3.1$ mm$^3$) and technical features (a 3.6-V maximum supply voltage and a 0.5-A current consumption)

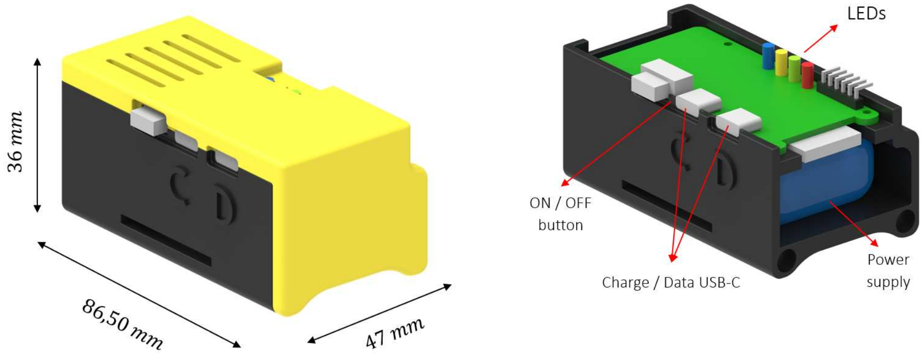


Figure 3.30: The hand exoskeleton secondary module enclosing the main electronic components: on the left, the overall sizes of the module are shown, while, on the left, the top side of the PCB is visible.

| Component | Model | Quantity | Voltage [V] | Current consumption [mA] |
|---|---|---|---|---|
| Motor | Pololu #4790 | 5 | 6 | 360 |
| Driver | TB6612FNG | 3 | 3.3 | 1.8 |
| Encoder | RM08VB0010B02L2G00 | 5 | 5 | 26 |
| Microcontroller | ESP32-S3-WROOM-1 | 1 | 3.3 | 250 |

Table 3.12: Current consumption and voltage of the main electronic components and actuator embedded in the hand exoskeleton.

favour its usage for this application. All these specifications are summarised in Table 3.12.

The total maximum power consumption $P_t$ of such components is around 13.26 W, according to the following expression:

$$P_t = 5(V_{motor}I_{motor}) + 5(V_{encoder}I_{encoder}) + 3(V_{driver}I_{driver}) + V_{esp}I_{esp} \quad (3.55)$$

in which $V$ and $I$ refer to each component's supply voltage and current consumption, reported in Table 3.12. To this purpose, a rechargeable battery pack with a capacity $C_b$ of 2.6 Ah and voltage $V_b$ of 7.4 V was exploited, ensuring a battery life $L_b$ of nearly two hours in the worst condition, as evaluated below:

$$L_b = \frac{C_b V_b}{P_t} = 1.57\ h \simeq 1\ h\ 35\ min \quad (3.56)$$

It is necessary to emphasise that the calculated battery life underestimates the actual value since it is evaluated in the worst-case scenario, meaning at the actuator stall. This condition, however, if reached, does not persist for the duration of the device's use. If, for instance, a mean value between the current consumption at stall condition (0.36 A) and maximum efficiency (0.08 A) was considered, the battery life increases to almost two hours and thirty minutes. Therefore, although the battery life might indeed be improved, the chosen power supply system was confirmed.

# Chapter 4

# Tests and results

Different experimental tests were performed to preliminary check if the set requirements for assistive purposes have been achieved. Firstly, tests on the achievable ROM and exerted forces were carried out in the thumb module, which is the first finger module developed due to its absence in the previous prototypes. Secondly, grasp and pinch forces were measured after developing the overall hand exoskeleton.

This chapter summarises the main results of these tests after describing how they were performed.

## 4.1 Thumb-handling module

A preliminary version of the thumb-handling module was the first one developed. All the custom components designed as presented in Chapter 3 were developed in-house or through the necessary manufacturing processes, while the commercially available ones were purchased. Then, the module was assembled, resulting in the prototype in Figure 4.1. Its mass is around 55 g, while its overall dimensions, except for the finger-handling mechanism that is user-dependent, are about $63.1 \times 35.3 \times 24.3$ mm$^3$. The module costs about 240 €, including the 3D printed and commercial components.

A healthy subject was involved in the tests upon signing an informed consent form. The specific user anatomic parameters were collected and used to optimise and customise the prototype (as mentioned in Section 3.1.1).

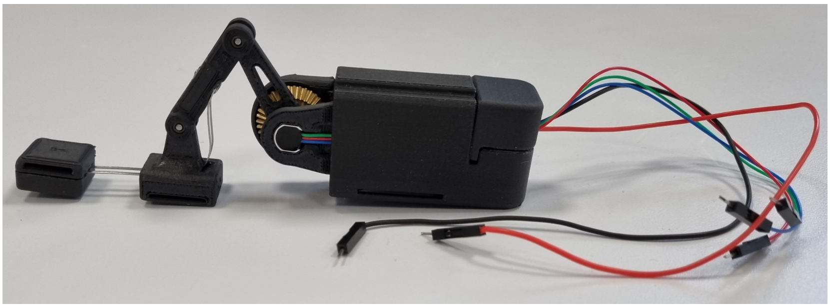

Figure 4.1: The prototype of the thumb-handling module with the hybrid architecture, embodiment of the design process described in this work.

### 4.1.1 ROM evaluation

The first crucial step is understanding if the hybrid architecture covers the user's finger ROM as much as possible. To this aim, some motion tests were performed after decoupling the mechanism from the actuation system and wearing it on the subject. While filmed, the subject was asked to flex and extend the thumb finger ten times, preventing metacarpal movement as much as possible. The same task was performed with and without the finger mechanism worn (Figure 4.2). The videos were elaborated using the open software Kinovea. Maximum f/e angles of the MCP ($\theta_{MCP}$) and IP ($\theta_{IP}$) joints were measured, and mean and Standard Deviation (SD) values are reported in Table 4.1. The evaluation highlighted an almost complete coverage of the MCP joint ROM while, globally, the mechanism allows for the coverage of 84% of the IP joint ROM.

A subsequent investigation exploited the encoder to verify and validate the $\theta_{MCP}$ angle measurements taken through Kinovea. Indeed, $\alpha_1$ (the angle Link 1 forms to the horizontal, shown in Figure 3.3) can be measured directly by the added encoder. An Arduino Nano Every was exploited for this task. From the kinematic study reported in Section 3.1.1, angle $\alpha_0$, thus also $\theta_{MCP}$, can be expressed and evaluated as a function of $\alpha_1$. The calculations were performed in MATLAB, and the comparison between the $\theta_{MCP}$ values resulting from the two acquisition methods is reported in Figure 4.3. It is interesting to observe the comparable measurements in correspondence with the maximum f/e conditions.

From the kinematic test, it has been possible to determine the relation between each joint angular coordinate and the angle $\alpha_1$. The scene was filmed

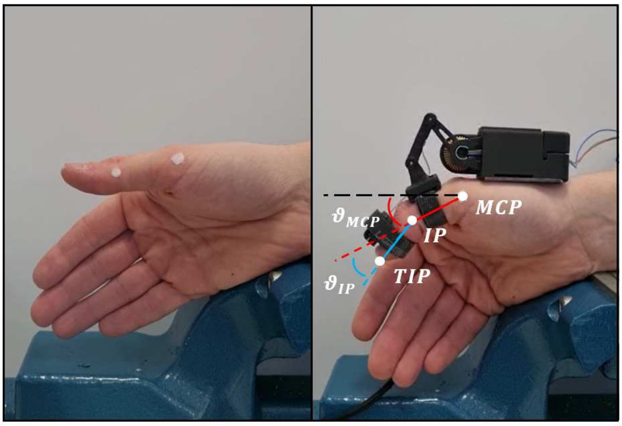


Figure 4.2: The setup for the ROM measurements during the thumb f/e while the subject wears and does not wear the prototype.

| | | *Unworn Device* | *Worn Device* |
|---|---|---|---|
| Extension | $\theta_{MCP}$ [°] | 3.53 ± 1.94 | 4.26 ± 3.1 |
| | $\theta_{IP}$ [°] | 17.21 ± 2.49 | 9.64 ± 2.72 |
| Flexion | $\theta_{MCP}$ [°] | - 54.69 ± 1.5 | - 55.74 ± 3.48 |
| | $\theta_{IP}$ [°] | - 60.25 ± 3.65 | - 55.26 ± 2.38 |

Table 4.1: The mean and SD values of the MCP and IP joints angles ($\theta_{MCP}$ and $\theta_{IP}$, respectively) while the subject wears (*Worn device)* and does not wear the device (*Unworn device)*.

while the subject performed five finger openings and closings. Still exploiting Kinovea, the angles $\theta_{MCP}$, $\theta_{IP}$, and $\alpha_1$ were measured each 0.15 s to detect the trend of the finger joints angular coordinates referred to that depending on the motor input. $\alpha_1$, indeed, varies from the motor angle by a constant corresponding to the transmission ratio chosen (1:2). Such measurements are reported as blue ($\theta_{MCP}$) and yellow ($\theta_{IP}$) dots in Figure 4.4. A linear regression resulted enough to approximate the relation between the angular coordinates $\theta_{MCP}$ and $\alpha_1$ ($R^2$ =0.9959), while a second-order polynomial best relates $\theta_{IP}$ and $\alpha_1$ ($R^2$ =0.98).

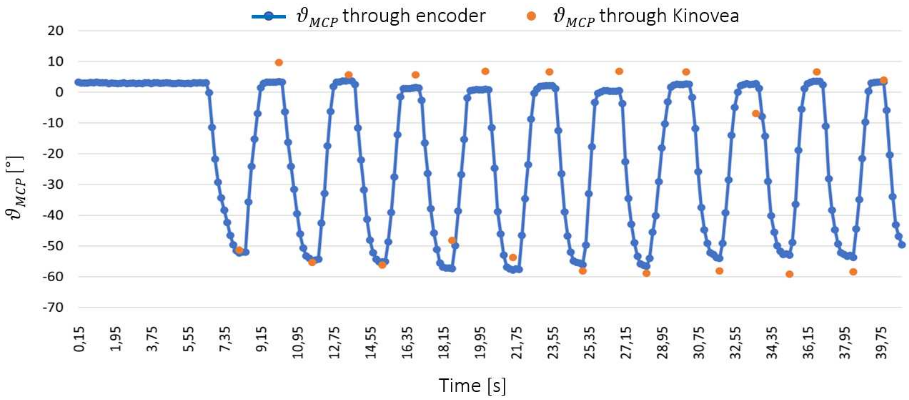


Figure 4.3: The $\theta_{MCP}$ angles evaluated by giving encoder data as input to the kinematic function (blue line) compared with the maximum f/e angles extracted from the recorded videos through Kinovea (orange points).

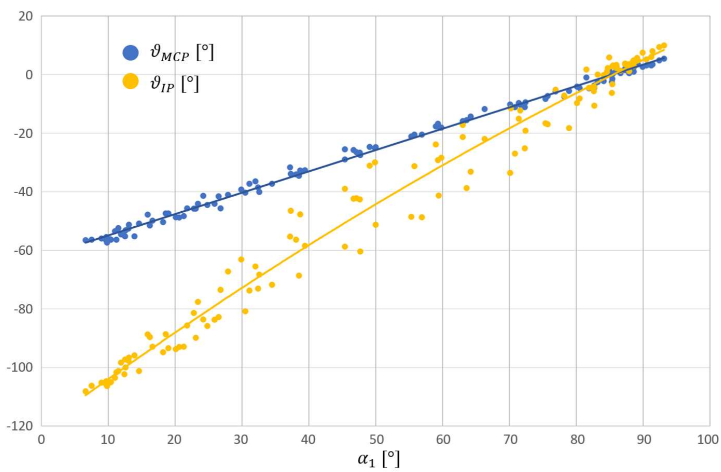


Figure 4.4: The relation between $\theta_{MCP}$ and $\alpha_1$, blue coloured, and that between $\theta_{IP}$ and $\alpha_1$, yellow coloured, resulted from the kinematic test.

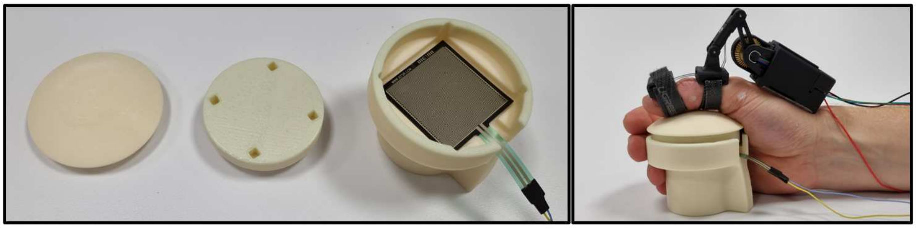

Figure 4.5: The component designed for housing the FSR during its characterisation and force measurement is on the left. From the left to the right, the three parts composing it are shown: (i) the coverage, (ii) the intermediate part, and (iii) the main body. On the right, instead, the configuration in which the measurements are taken is shown.

### 4.1.2 Forces evaluation

In addition to ROM evaluation, measurements of the exerted forces were performed. A Force Sensing Resistor (FSR) 406 from Interlink Electronics, coupled with a 3.3 kΩ resistor and a dual motor driver (TB6612FNG) from TOSHIBA, was hooked up to the same Arduino Nano Every to control the module actuator and collect indirect measures of the forces the actuated finger can exert on objects. They can sense forces ranging from 0,2 N (20 g) to 20 N (2000 g). When a force is applied to the FSR, the different layers composing it are pressed together, and protrusions make contact: higher forces determine more contact points, thus lowering resistance and increasing voltage.

Characterising the FSR is mandatory to derive the force applied based on the recorded output voltage. A custom 3D-printed housing for the FSR, shown on the left of Figure 4.5, was designed. It consists of three parts: (i) the main body to house the sensor; (ii) the coverage to be used only during the force measurement phase; (iii) an intermediate part designed to determine a flat and stable surface for placing masses during the sensor characterisation while distributing the load evenly on the sensor surface. Continuous incremental loading and unloading cycles (i.e., the masses were added or removed by incremental steps without entirely unloading the sensor between different measures) were performed according to the following setup. Measures were acquired at 1 Hz. A 100-g load was added every 20 s. The sensor was given 10 seconds to stabilise, and then the remaining ten measures were considered for characterisation. The complete loading/unloading cycle (from 0 to 2000 g and vice versa) was per-

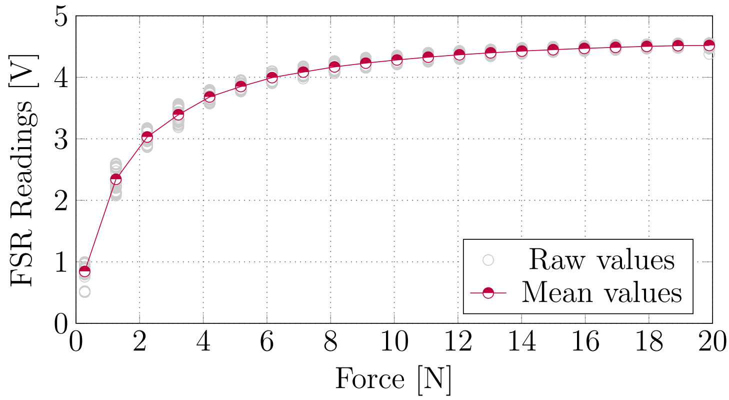


Figure 4.6: FSR characterisation: the graph shows the FSR voltage readings as the force applied to the sensor changes. The measurements (raw values) taken during the three repetitions are grey-coloured, while the mean values are purple-highlighted.

formed thrice. The recorded outputs (i.e., the 10-bit conversion operated by the microcontroller ADC) during the three cycles are reported in Figure 4.6. For each interval, the mean value was calculated. Then, they were linearly interpolated two by two to use that curve to derive the mass (i.e., the force) corresponding to the measured output during the tests. The interpolating curve is shown in Figure 4.6.

When the sensor characterisation was completed, the subject was asked to wear the device for force measurements. The subject was also asked to remain passive while the actuation system drove the mechanism. The experimenter sent extension, flexion, and resting commands to the finger module via serial communication. The experimental setup, as visible on the right of Figure 4.5, involved the thumb being pressed by the mechanism against the FSR sensor housing. The actuator power supply was limited to up to 90% of the stall current to avoid excessive overheating. As chosen during the characterisation, the second ten recorded measures were considered after the subject's finger got in touch with the sensor. Several repetitions were performed. However, only seven have tuned out to be appropriately acquired. The average of the ten acquisitions was calculated for each repetition; then, the corresponding force was extrapolated through the sensor characterisation. Table 4.2 summarises the results of this test. It is worth mentioning that the thumb module was designed to exert about 15 N on the finger and withstand the actuator stall condition. The measurements proposed in this section show that the target force was rather achieved by calculating a mean value of about 10.6 N. The significant variability in the results can be attributed in the first instance to the involvement of the human subject in the experimental setup.

| | M1 | M2 | M3 | M4 | M5 | M6 | M7 |
|---|---|---|---|---|---|---|---|
| Force [N] | 5,94 | 7,81 | 16,78 | 11,31 | 12,79 | 11,66 | 7,89 |

Table 4.2: The mean output force values for seven f/e movements.

## 4.2 Hand exoskeleton

Given the promising results achieved for the thumb module, the overall hand exoskeleton was developed. All the components were assembled, obtaining the device shown in Figure 4.7 The main module weighs 330 g, while the electronic one is 150 g. The rough dimensions of each are respectively as shown in Figures 3.26 and 3.30 of Chapter 3, thus $24.30 \times 52.40 \times 35.30$ mm$^3$ for the thumb module housing, $77.80 \times 61.10 \times 35.30$ mm$^3$ for the housing of the other finger modules, and $86.50 \times 47 \times 36$ mm$^3$ for electronics module. Its cost, including the electronic component, is around 1700 €.

Tests on the developed hand exoskeleton were performed to measure the exerted forces while grasping and pinching specific objects designed for the purpose. Grasping and pinching are indeed prehensile actions that are part of common daily activities.

### 4.2.1 Grasp and pinch forces evaluation with FSRs

Upon signing an informed consent, the subject involved in the previous experimental session was enrolled for the new tests. Grasping and pinching tests were performed twice, varying the soft component material: in the first session, flat springs in spring steel, as that exploited for the thumb module experimental session (Section 4.1), which is 0.3 mm thick, 6 mm wide, and has a longitudinal slot of 3 mm, were used, while in the second session, the hand exoskeleton was provided of polycarbonate foils 0.5 mm thick and 9 mm wide, with an entire cross-sectional area. The second alternative was considered to test the hand

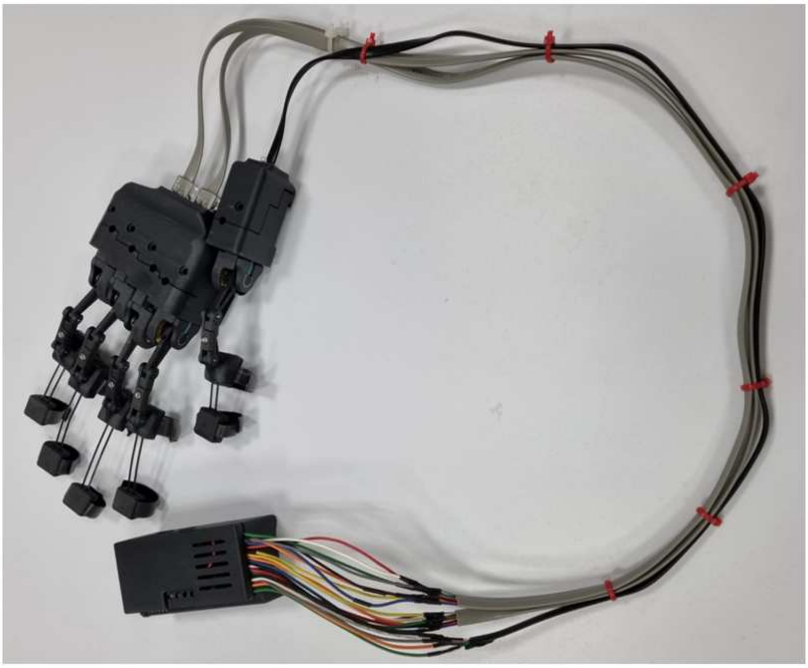

Figure 4.7: The hand exoskeleton developed following the design process presented in this thesis: the main module housing the actuation system and finger-handling mechanisms, and the secondary one enclosing the electronic components.

exoskeleton performances while exploiting a less stiff soft architecture than that in spring steel. Specifically, the polycarbonate elastic module, which influences the component stiffness, is 2400 MPa, while that of the spring steel is E= 206000 MPa.

To evaluate the grasping capabilities of the novel hand exoskeleton, the objects shown in Figure 4.8 were developed, allowing testing different types of grasp. They were designed to house a FSR 406 of square shape with 43.69 mm side and 0.46 mm thickness, used to measure the force exerted on the objects, as already done for the thumb module test. The specific dimensions of the developed objects are summarised in Table 4.3.

Concerning cubic and cylindrical objects, they were designed so that the

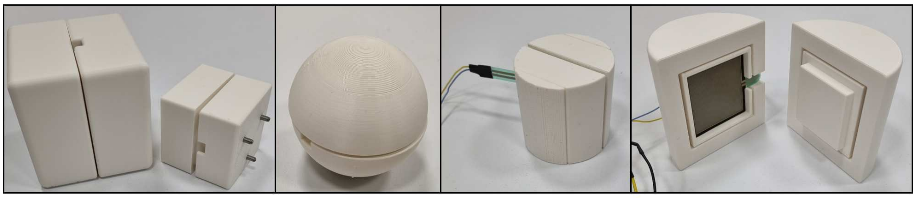

Figure 4.8: The objects designed for the grasping force measurements: from the left, the 75-mm and 50-mm cube, 75-mm sphere, 50-mm cylinder, and 75-mm cylinder with a view on the FSR housing in the 50-mm cube.

| Cube | | Sphere | Cylinder | |
|---|---|---|---|---|
| Size A | Size B | Size B | Size A | Size B |
| $50 \times 50 \times 50$ mm$^3$ | $75 \times 75 \times 75$ mm$^3$ | 75 mm$^3$ | $50 \times 50$ mm$^3$ | $75 \times 75$mm$^3$ |

Table 4.3: The dimensions of the sensorised objects for different sizes and geometries.

greater size objects, consisting of two parts, enclose the smaller ones during usage, which in turn houses the FSR, as visible on the right of Figure 4.8. Indeed, the smaller size cube-and-cylinder objects consist of two parts as well: on one side, the sensor is housed, while on the other, a thickening corresponding to the sensor active area (39.6 mm$^2$) was designed so that the force is discharged as equally as possible over the entire measurement area. Both parts of the greater size objects present thickening equal to the sensor's active area, and centring pins allow for maintaining contact only in this area and prevent displacement among them.
Due to the sensor dimensions, only the greater size of the spherical object was developed instead, but it was designed following the same concept as the previous smaller-sized objects. All of them are 3D printed in ABS with a Stratasys F370 3D printer.

The FSR, whose sensing capability ranges from 0.2 N (20 g) to 20 N (2000 g), was characterised following a procedure analogous to that presented in Section 4.1.2, after hooking it up to an Arduino Nano Every to collect forces measurements. It means that the 100-g load is incremented every 20 s, of which the first ten are left for sensor stabilisation, while only the second ten recorded measurements are considered for the sensor characterisation. The resulting curve is

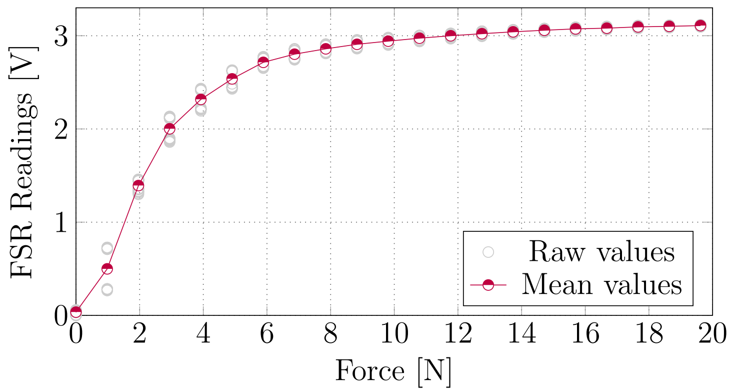


Figure 4.9: FSR 406 characterisation for grasping tests: the graph shows the FSR voltage readings as the force applied to the sensor changes. The measurements (raw values) taken are grey-coloured, while the mean values are purple-highlighted.

reported in Figure 4.9.

After the sensor characterisation, the subject was asked to wear the hand exoskeleton for the force measurements and remain as passive as possible during the mechanism actuation. The experimenter sent extension, flexion, and resting commands to the hand exoskeleton via serial communications. The actuator power supply was limited to up to 90 % of the stall current to avoid excessive overheating.

The grasping tasks were performed as shown in Figure 4.10. Following the same criterion exploited during the sensor characterisation, only the second ten recordings were considered after the subject grasped the object under analysis. Five repetitions were performed, and the average value of the ten measurements was calculated for each of them. Finally, the corresponding force was derived from the FSR characterisation curve. The same procedure was followed for all the objects tested and repeated for the two mentioned sessions. The results of both are summarised in Table 4.4. It is worth noting that, during the first session (polycarbonate one), two measurements are lacking in cube grasping since they were not properly acquired. They are indicated with the symbol (-) in Table 4.4.

The same procedure reported for the previous force test was followed for evaluating pinch forces. The object to pinch was designed to house the FSR

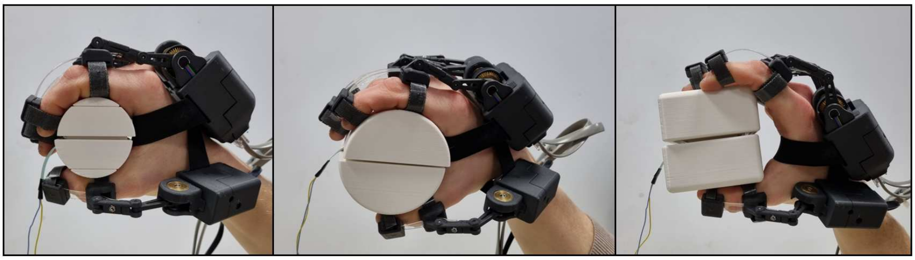

Figure 4.10: The grasping tasks: a view of the 50-mm cylinder, 75-mm cylinder, and 75-mm cube grasps.

| | | M1 [N] | M2 [N] | M3 [N] | M4 [N] | M5 [N] | Mean [N] | SD |
|---|---|---|---|---|---|---|---|---|
| Polycarbonate | 50-mm cylinder | 5.67 | 4.08 | 3.37 | 2.67 | 3.00 | 3.76 | 1.07 |
| | 75-mm cylinder | 7.10 | 6.42 | 6.5 | 8.01 | 8.55 | 7.32 | 0.84 |
| | 50-mm cube | 4.25 | 5.12 | 3.31 | 4.20 | - | 4.22 | 0.64 |
| | 75-mm cube | 6.05 | 5.27 | 5.00 | 4.20 | - | 5.13 | 0.66 |
| | 75-mm sphere | 5.70 | 5.54 | 5.59 | 4.81 | 5.71 | 5.47 | 0.3 |
| Spring steel | 50-mm cylinder | 4.50 | 8.46 | 8.72 | 8.31 | 7.70 | 7.54 | 1.55 |
| | 75-mm cylinder | 6.69 | 15.29 | 15.55 | 8.47 | 7.74 | 10.74 | 3.85 |
| | 50-mm cube | 4.88 | 7.20 | 6.46 | 5.49 | 4.20 | 6.01 | 0.88 |
| | 75-mm cube | 5.71 | 5.07 | 5.41 | 6.24 | 10.21 | 6.53 | 1.88 |
| | 75-mm sphere | 6.66 | 4.96 | 5.10 | 7.16 | 11.10 | 6.99 | 2.23 |

Table 4.4: The output force values measured (Mx) during the five repetitions of each object grasping in the two sessions, differing in the soft component material, their mean and SD values.

400 of circular shape and a maximum diameter of 7.6 mm (Figure 4.11). It is a 30-mm-diameter cylinder with a central thinning (12 mm) corresponding to the area to pinch, divided into two parts, one for housing the sensor and the other to press on it. Three cylindrical pins allow for aligning the two parts.

The FSR has the same sensing capability as that exploited for grasping tests. Thus, the characterisation procedure does not change from that already followed for the previous tests. The resulting curve is shown in Figure 4.12.

Once the sensor was characterised to measure the force value corresponding to the FSR readings, the subject wore the hand exoskeleton and was asked to remain as passive as possible during the measurements. In particular, three finger combinations were tested: thumb-index, thumb-middle, and thumb-ring. The thumb-small combination was not considered as infrequent in daily activ-

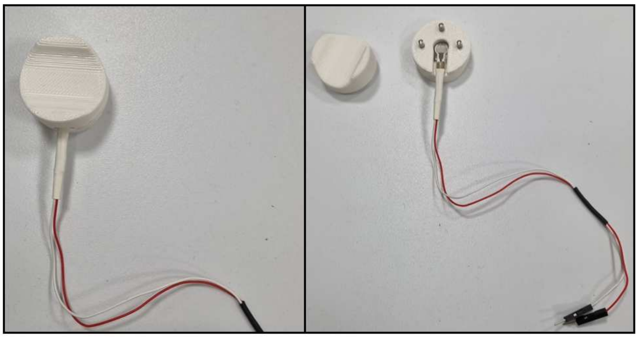

Figure 4.11: The object designed for pinch force measurements.

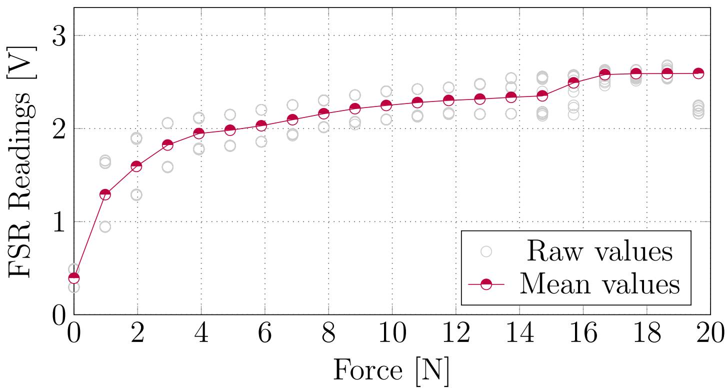


Figure 4.12: FSR 400 characterization for pinch tests: the graph shows the FSR voltage readings as the force applied to the sensor changes. The measurements (raw values) taken are grey-coloured, while the mean values are purple-highlighted.

ities. The experimenter sent flexion, extension, and resting commands to the fingers involved in the combination under analysis. The pinch task was repeated five times for each combination, and the last ten recordings were considered to evaluate the corresponding mean force value of each repetition. As for the grasp tasks, the test was repeated twice, involving the different materials for the soft component. Table 4.5 summarises the results achieved with these tests in terms

| | | M1 [N] | M2 [N] | M3 [N] | M4 [N] | M5 [N] | Mean [N] | SD |
|---|---|---|---|---|---|---|---|---|
| Polycarbonate | Thumb-Index | 2.01 | 3.51 | 2.35 | 1.77 | 1.63 | 2.25 | 0.67 |
| | Thumb-Middle | 2.22 | 0.81 | 3.11 | 2.8 | 2.53 | 2.31 | 0.89 |
| | Thumb-Ring | 2.27 | 2.01 | 2.53 | 3.53 | 2.62 | 2.58 | 0.57 |
| Spring steel | Thumb-Index | 5.98 | 3.00 | 3.04 | 3.61 | 2.99 | 3.72 | 1.15 |
| | Thumb-Middle | 3.17 | 4.75 | 4.90 | - | - | 4.27 | 0.78 |
| | Thumb-Ring | 5.20 | 7.17 | 8.37 | - | - | 6.91 | 1.31 |

Table 4.5: The output force values measured during five repetitions of the pinch task between thumb and index, thumb and middle, and thumb and ring, their mean and SD values. The values are reported for both sessions, differing in the soft component material.

of the mean force measured in each test repetition for the three combinations. The measurements that were not adequately acquired are indicated with the symbol (-).

Tables 4.4 and 4.5 show that using flat springs in spring steel for the soft architecture allows the achievement of higher mean force values than those measured in the case of exploiting polycarbonate foils both in grasping and pinching tasks, especially due to the stiffness the material confers to the component.
Regarding grasping tasks, larger objects allowed a better grip because each finger was in contact with the object to be grasped. On the contrary, some fingers were not adequately gripped when grasping smaller objects, leading to measuring higher force values when grasping larger objects than smaller ones. The subject could grasp, hold, and manipulate the proposed items. However, the measured forces turned out to be below expectations, not reaching the 15-N-per-finger target value. In particular, the subject could effectively grasp the 75-mm cylinder, resulting in the highest force values measured (10.74 N is the mean value among the five repetitions). The force measurements decrease in pinch tasks due to the lower number of fingers involved.

The results obtained from the experimental tests on the hand exoskeleton show that the target force was achieved only thanks to the contribution of all the fingers. This achievement can be attributed to two main aspects, one related to the measuring instrument and the other to the interface between the hand and exoskeleton. Concerning the measuring instrument, FSRs are low-cost and easy-to-use force sensors that require little space and can be easily integrated into objects for grasping tasks. However, these strengths are coupled with worse accuracy than other sensors, such as load cells, that could provide more precise measurements and wider ranges of measurable forces. Indeed, the mean values

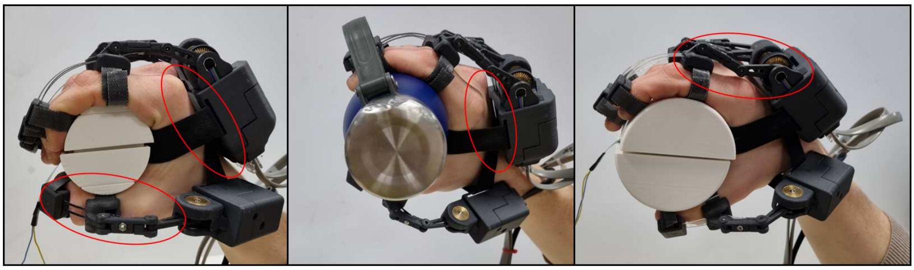

Figure 4.13: Some pictures showing the flaws that emerged during the experimental session: on the left, the exoskeleton does not adhere properly to the hand, and the thumb does not oppose correctly; on the centre, another view of the connection issue; on the right, the change in the index four-bar mechanism configuration.

measured in this experimental session are comparable with those achieved while testing only the thumb module, revealing that the measurement instrument can influence the results.
Besides, there were side findings. The tests indeed revealed an abnormal behaviour of the main module housing the actuation system, which tends to discharge, what it seems, a large part of the transmitted forces onto the hand back rather than to the mechanism. The differences in curvature generated between the hand and exoskeleton during movement, as highlighted in Figure 4.13, do not allow the elastic band used to hold the module to adhere correctly to the hand, thus not ensuring the correct force transmission that is consequently discharged onto the hand and limiting the device comfort. Similarly, the Velcro straps used to connect the hybrid-architecture end-effectors to the fingers do not guarantee sufficient adherence between the parts, sometimes resulting in the end-effector itself sliding along the matching phalanx, which in some cases nullifies the effect of mechanical stop and changes the four-bar mechanism configuration after overcoming the singularity condition (Figure 4.13). This effect was less pronounced in the thumb-module tests, as the movement of the other fingers had only a minor influence on the Velcro strap connecting the module to the finger. However, in the whole hand exoskeleton, the thumb module does not allow the finger to always oppose correctly in grasping tasks (as visible in Figure 4.13), affecting force measurements.

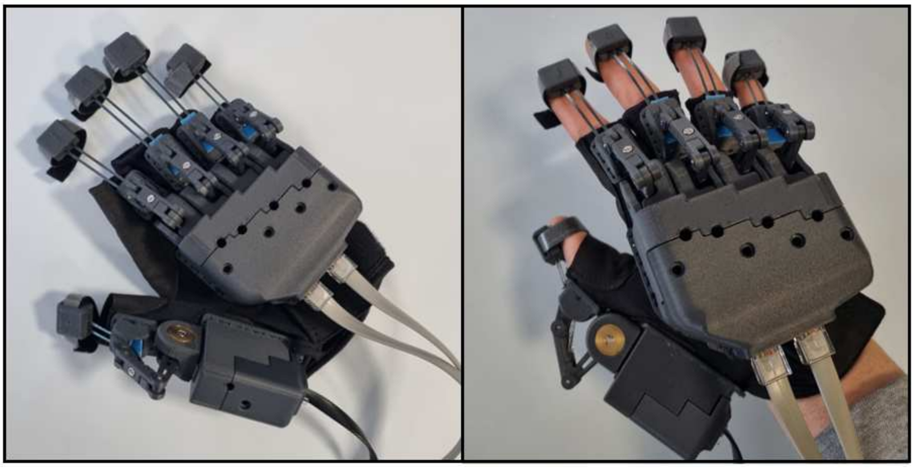

Figure 4.14: The new exoskeleton embodiment.

### 4.2.2 Grasp and pinch forces evaluation with load cells

The tests described above highlighted two main issues, one related to the measurement instrument and one to the interface between the hand and exoskeleton. With the aim of overcoming them, the device equipped with flat springs in spring steel was sewn to a glove before running new tests to reduce its movement relative to the hand. Specifically, the module on the hand back and the thumb one were sewn to a non-elastic glove covering the fingers up to the proximal phalanges. Such a feature preserves the sense of touch of the finger palm while allowing each mechanism end-effector to be sewn to the glove. Besides, a Velcro strap fixes the glove in correspondence with the wrist. The new exoskeleton embodiment is reported in Figure 4.14. Sewing the exoskeleton to the glove improved the device's adherence to the hand and prevented the mechanism end-effectors from sliding along the matching phalanges.

In addition to the interface modifications, the new experimental tests were conducted by exploiting load cells for measuring the gripping force during grasping and pinching tasks. Specifically, a cylindrical artefact (shown in Figure 4.15) was designed and 3D-printed in ABS to house two FSSM (0-500 N) load cells from Forsentek, placed perpendicular to each other and at a distance of 70 mm, approximately equal to the hand-palm width. The artefact includes (i) the main body, consisting of two parts that house the load cells, and alternatively, (ii) two

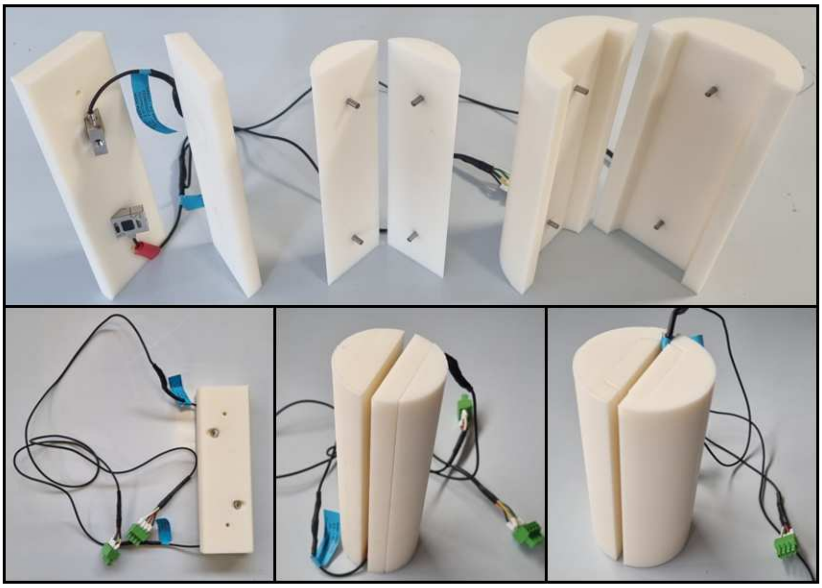

Figure 4.15: The cylindrical artefact provided with load cells: on the top, the parts of the artefact, on the bottom, from the left to the right, the main body for the pinch task, and the 50-mm and 75-mm cylinders for grasping tasks.

cylindrical caps to form a 50-mm diameter cylinder or two caps to form a 75-mm diameter cylinder. Cylindrical pins prevent misalignment and displacement among the parts. The artefact design ensured the same load cell arrangement during all the tests, avoiding the need to screw and unscrew them in different components each time. Moreover, this mounting configuration releases the need to orient the gripping force, the direction of which is difficult to predict, along the load cell axis.

Each load cell was coupled with an FSF (0-5V) amplifier from Forsentek to read the measurements taken. Each load cell *zero* was adjusted under no-load conditions. The *span* was instead regulated under compression conditions (as during the tests). Figure 4.16 shows the force outline for both calibration and experimental phases. In this last phase, the total grasping force $F$ is evaluated as $F = \sqrt{{F_x}^2 + {F_y}^2}$ to include all the gripping contributions. $F_x$ and $F_y$ can be calculated as $F_x = \sqrt{2}(F_{2//} - F_{1//})$ and $F_y = \sqrt{2}(F_{2//} + F_{1//})$, respectively,

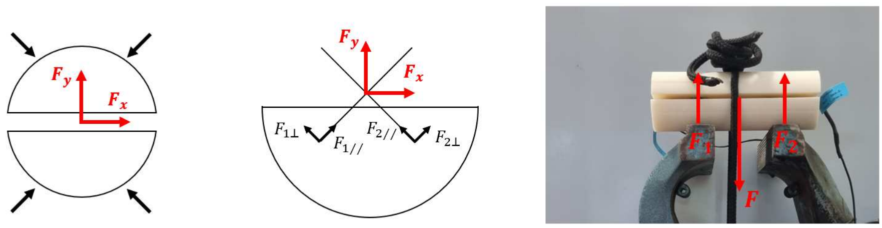


Figure 4.16: The force outline: from the left to the right, the gripping force and its outline in the experimental phase, and the weight force in the calibration phase.

where $F_{1//}$ and $F_{2//}$ are the forces measured along the load cell, derived according to the corresponding characterisation curve, reported below. It is worth noting that during the calibration phase, the cylinder was resting on two supports, and the load $F$ was assumed to be applied to the centre of the artefact's main body only along the $y$ direction. Due to this load cells configuration, the forces along the load cell $F_{1//}$ and $F_{2//}$ are equal to $\frac{F}{2}cos45$, from which it follows that the mass read for each cell corresponds to $\frac{\sqrt{2}M}{4}$.
Under the assumption that each cell can read up to 25 kg (well within the maximum measurement range of up to 50 kg), the *span* was adjusted by applying to the cylinder a mass $M$ of around 14 kg and considering a proportional law between the load cell reading and the corresponding mass read by each load cell ($\frac{\sqrt{2}M}{4} \simeq 4.9$ kg).

Following the calibration, the load cells' characterisation curve was determined to derive the force applied based on the recorded output voltage. In the same compression condition, three continuous loading and unloading cycles were performed by applying known masses to the cylindrical artefact. As done for the FSR characterisation, the masses were added or removed by incremental steps without unloading the sensor between different measures.
During the loading phase, the masses were added in the following order: (i) 4.000, (ii) 4.966, (iii) 4.872, (iv) 4.975, (v) 5.061 kg; therefore, the resulting loads applied to the artefact are (i) 4.000, (ii) 8.966, (iii) 13.838, (iv) 18.813, (v) 23.874 kg. The order is contrary in the unloading phase. Measures were acquired at 10 Hz. The recorded outputs for each load cell (due to the 10-bit conversion operated by the microcontroller ADC) were reported in Figures 4.17 and 4.18. For each mass, the readings' mean value was calculated after sen-

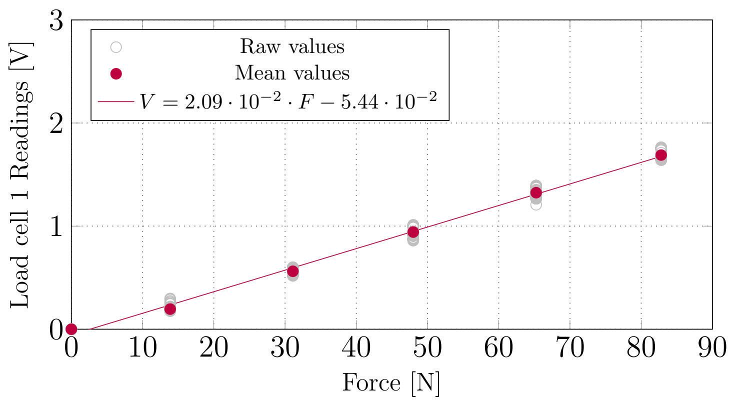


Figure 4.17: Characterisation curve of load cell 1: the graph shows the load cell voltage readings as the force applied to the sensor $F_1$ changes. The measurements (raw values) taken during the three repetitions are grey-coloured, while the mean values and regression line are purple-highlighted. The line expression is reported in the legend.

sor stabilisation. Linear regressions enabled interpolating data from both load cells ($R^2 = 0.9972$ and $R^2 = 0.999$, respectively) and approximating the relation to derive the force on each load cell based on the matching readings. The Voltage-Force curves of the load cells are reported in Figures 4.17 and 4.18.

The load cells' outputs were then recorded and combined while applying the setting-span mass (13.838 kg) in the same configuration and rotating the 50-mm cylinder to evaluate the error due to the difference in the object grasping direction (Figure 4.19). Mass readings were recorded every 15° along the circumference at 10 Hz. Two complete rotations were performed while the load was applied to the cylinder centre, and the mean value at each step was evaluated. The maximum error was detected when the cylinder had been rotated 90° from the position in Figure 4.19 and reached 4,2 kg, while the mean value along the circumference is about 12,7 kg, with a SD of 1,2 kg, which is 9.5% of the measuring mass. The percentage reduces up to 6.1% by averaging values recorded with rotations between 120° and 240° and those between -60° and 60°.

Once the characterisation curve of the load cells and the error caused by the grasping direction were known, new tests were carried out, performing grasping and pinching tasks.

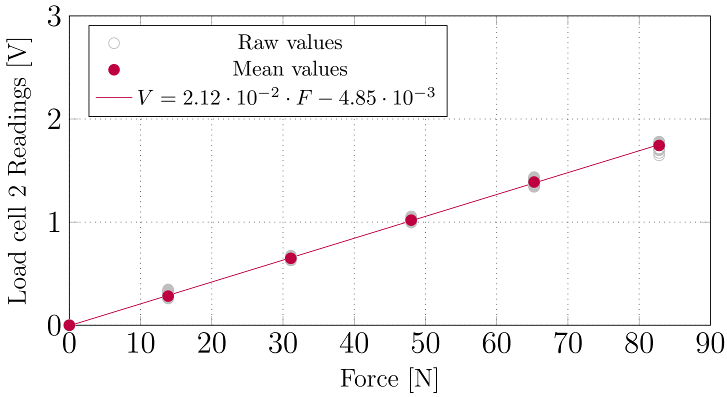


Figure 4.18: Characterisation curve of load cell 2: the graph shows the load cell voltage readings as the force applied to the sensor $F_2$ changes. The measurements (raw values) taken during the three repetitions are grey-coloured, while the mean values and regression line are purple-highlighted. The line expression is reported in the legend.

Seven healthy subjects (6 males aged between 27 and 60 and 1 female aged 29) were enrolled for these tests upon signing informed consent. Only one of them had already experienced the exoskeleton since participating in the previous test sessions. The same device was used for all the subjects since compatible with their hand sizes.

Each subject was administered three tasks: two grasp and one pinch tasks, consisting of gripping 50-mm and 75-mm cylinders and only the main body of the artefact housing the load cells (25-mm thick), respectively. It is worth highlighting that if the diameter of the cylindrical artefacts developed for these tests is the same as the cylinders used in the previous tests, the thickness of the artefact to pinch is higher than the one previously exploited due to the load cell sizes and mounting configuration.

One at a time, subjects were asked to don the exoskeleton and remain as passive as possible during the actuation. The experimenter sent extension, flexion, and resting commands via serial communications to the finger modules involved in each task. Once the object was gripped, the force measurements, depending on the characterisation curves derived above, were recorded at 10 Hz. Each task was repeated several times, and for each, the mean and SD values were

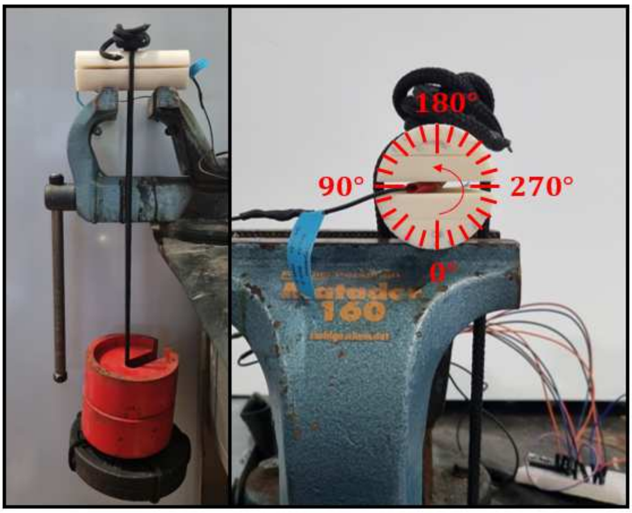


Figure 4.19: The set-up for load cells characterisation, on the left, and the angles at which the setting-span mass was evaluated to calculate the measurement error along the circumference.

calculated if at least 15 stable signal measurements had been read. The 10 best grips were considered to calculate the overall mean and SD values of the force measured for each subject and task, as reported in Table 4.6. The values out of the trends were deleted and not considered to determine the results reported in the table.

The table shows that all the subjects were able to perform the proposed tasks. Averaging the results of the subjects involved, higher forces were measured in this session (50-mm cylinder grasp: 16.73 ± 6.51 N; 75-mm cylinder grasp: 19.41 ± 3.76 N; pinch: 7.41 ± 1.52 N) than those recorded in the previous one (50-mm cylinder grasp: 7.54 ± 1.55 N; 75-mm cylinder grasp: 10.74 ± 3.85 N; pinch: 3.72 ± 1.15 N) thanks to the higher accuracy and wider range of measurable force of load cells compared to FSRs and the improved adherence determined by the glove. Indeed, as visible in Figure 4.20, the mechanism end-effectors act on the middle of the proximal phalanges and cannot slide along them. In addition, the sewing prevents the device from rising on the hand back.

Better results were achieved in the case of Subject 1 than in the other participants. It can be attributed to the prior experience the subject had had with

| | 50-mm-cylinder | | 75-mm-cylinder | | Pinch (Thumb-Index) | |
|---|---|---|---|---|---|---|
| | Mean value [N] | SD [N] | Mean value [N] | SD [N] | Mean value [N] | SD [N] |
| S1 | 31.413 | 5.301 | 27.006 | 3.259 | 7.220 | 0.431 |
| S2 | 13.250 | 2.983 | 20.757 | 3.575 | 8.069 | 0.851 |
| S3 | 11.798 | 2.511 | 16.903 | 1.269 | 5.942 | 0.217 |
| S4 | 15.429 | 1.638 | 21.598 | 2.652 | 10.506 | 2.740 |
| S5 | 19.128 | 2.352 | 17.806 | 2.569 | 5.708 | 0.424 |
| S6 | 10.831 | 1.292 | 15.179 | 1.574 | 6.556 | 0.604 |
| S7 | 15.241 | 1.743 | 16.630 | 1.250 | 7.920 | 0.890 |

Table 4.6: The mean output force and SD values for each subject and task performed during this experimental session.

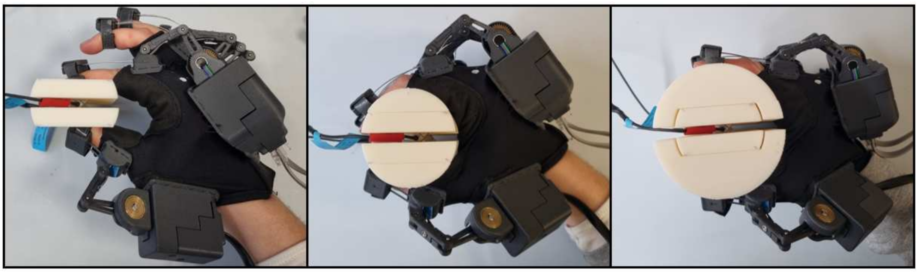

Figure 4.20: The gripping tasks administered: from the left to the right, the pinch task, the 50-mm and 75-mm cylinder grasp, in which the improved adherence of the new exoskeleton embodiment is visible.

the exoskeleton, revealing that training can improve results.
For grasping tasks, most participants expressed higher forces for gripping the 75-mm cylinder rather than the 50-mm one, as deduced from the previous tests, since grasping large objects allows more fingers to make contact than small ones. Specifically, the small finger usually failed to make contact with the 75-mm cylinder to grasp, while sometimes even the ring finger did not make contact if the 50-mm cylinder grasp is performed, as highlighted in Figure 4.21. This happens because their mechanisms do not remain kinematically coupled to the corresponding fingers during the hand closure due to the metacarpals movement, which is larger for the small finger than the others. Accordingly, the forces are not always adequately transmitted from the mechanism to the finger.

The measured forces are higher than those recorded in the previous test ses-

Figure 4.21: Fingers not in contact in grasping the 50-mm cylinder, on the left, and the 75-mm one, on the right.

sion. Nonetheless, the target force has not yet been achieved. This finding can be attributed to the same aspects highlighted above, i.e., the measurement instrument and interface between the hand and exoskeleton, which require further improvements. Concerning the former, even though the load cells' positioning releases from the need to apply force along the load cell axis, the variability of the outcomes is still dependent on the grip direction, as evaluated before. However, when an object is gripped, the forces are not exchanged at only one point, and it is not certain that the forces' resultant is centred, referring to the load cells. On the contrary, this aspect does not affect pinch tasks, which accordingly have more stable results among the subjects involved than grasp ones. Regarding the interface between the hand and exoskeleton, instead, on one side, the hand back module sewing on the glove improved the adherence; on the other, its compactness and rigidity do not allow it to follow the metacarpals movement during the hand closing, which can also be very large, as in the case of the small finger, leading to a substantial increase in the distance between the finger MCP and mechanism actuated joint, which, in turn, compromises the kinematic coupling between them (Figure 4.21).
Finally, another aspect influencing the results achieved has to be highlighted. Tests with FSRs showed better results when flat springs in spring steel were exploited than polycarbonate ones. However, as emerged also from the tests with load cells, the foil stiffness compromises the change in curvature during move-

ment and also the force transmission to the finger-handling mechanism, which feels high resistance, resulting in exceeding the actuator effort and preventing the full ROM coverage. To identify the foil's optimal material and section size for this purpose, a model of the hybrid-architecture finger-handling mechanism was developed and simulated, as reported in the following chapter.

## 4.3 Discussion

The hand exoskeleton presented in this thesis is a novel assistive device that meets most requirements for this purpose among those listed in Chapter 1 and stands out within the state of the art. Although slightly higher than the threshold on the hand, the whole hand exoskeleton mass is comparable to or less than the other current state-of-the-art devices reported in Table 1.1, ensuring its *lightness*. Only a few devices in Table 1.1 are lighter than that presented in this work. However, [48, 53] do not actuate all the fingers; similarly, [49, 51, 52, 58, 56, 69, 73, 98, 104] place their actuation systems (pneumatic [49, 58, 69, 104], hydraulic [72], or electric [51, 52, 56, 73, 98]) away from the hand, reducing the device mass on the hand itself but compromising its wearability.

The *lightness* and *small overall sizes* have been pursued through careful design and selection of each component, which in turn ensure the complete device *wearability* and *portability*. Figure 4.22 shows some grasping tasks involving different-sized water bottles, a stapler, and a door handle, highlighting the possibility of using the device even in confined spaces due to its small size.

One motor per finger enables independent finger movement (not always present in the devices in Table 1.1), while coupling each to a bevel gear rigid transmission ensures bidirectional movements. Both aspects contribute to improving the device's *dexterity*.

Exploiting a RCM mechanism and a validated kinematic optimisation procedure to tailor the device to the user's hand anatomy add *safety* and promote *comfort*, even if it has to be improved. In addition, the actuator has a minimum back-drivability that enhances *safety* strength of the new hand exoskeleton since, in case of an operating failure, the mechanism can be manually returned to the resting condition. Concerning *comfort*, instead, a more compliant interface between the hand and exoskeleton must be detected so that the device can also be used for prolonged periods without annoyance.

The interface also deals with two other requirements, the immediate one concerning *sense-of-touch preservation*, and that relating to the *efficacy in ADLs*.

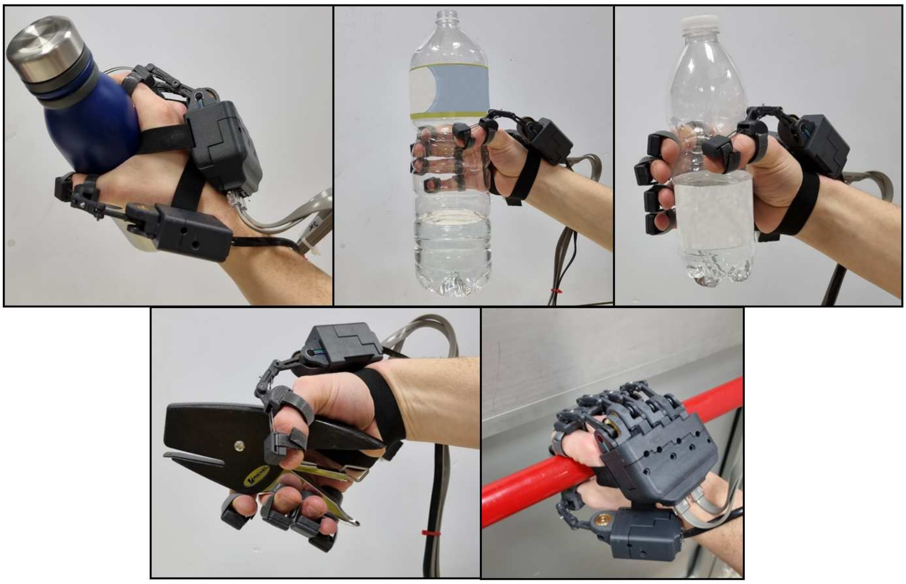

Figure 4.22: Some pictures of the subject involved in the experimental test while grasping ordinary objects: different-sized water bottles on the top, a stapler and a door handle on the bottom.

The device tested in Section 4.2.1 completely preserves the *sense of touch*, but issues related to its adherence to the hand back arose. The device tested in Section 4.2.2 was thus sewn to a glove to reduce its movement on the hand back. As mentioned before, using a glove may limit the *sense of touch*. However, the chosen one covers up to the proximal phalanges, leaving free the fingers' palm, and additional openings can be created in correspondence with the palm to increase the *sense of touch* in this area as well. Concerning the *efficacy in ADLs*, the interface might affect the force transmission to the finger-handling mechanism. It is evident with the device tested in Section 4.2.1 since it does not prevent the relative movement between the parts. However, even the device sewn onto the glove cannot be the definitive solution since, besides the complex wearability on impaired hands, the unique hand-back module prevents the correct kinematic coupling between the mechanism and the matching finger despite the improved adherence. Furthermore, force measurements can be affected by

incorrect thumb opposition. Thus, a compliant interface consisting of a hand-back module per finger and including a system to manage thumb opposition could improve *efficacy in ADLs* and *comfort* requirements.
Nonetheless, except for [58, 79], the force measured during grasping and pinching is greater than or similar to those reported in Table 1.1, but the target force has not yet been achieved. This can also be attributed to the load cells, which, while more accurate than FSRs, are subject to errors due to the direction of the applied force. Designing an artefact equipped with strain gauges can be considered for future measurements to disengage from the gripping direction and measure the force applied in relation to the strain produced.

*Intuitiveness* instead is not the focus of this work since it is related to developing the control strategy.

Last but not least, the device cost makes it *affordable*, even if no easy terms of comparison are available.

# Chapter 5

# Hybrid-architecture multibody modelling

Experimental tests performed on the finger and hand exoskeleton, as reported in Chapter 4, highlighted how results can vary based on the soft architecture implemented in the hybrid architecture. On one side, the rigid architecture and actuation system have been the subject of an extensive study that has made it possible to pursue most requirements for assistance set out in Chapter 1. On the other side, the soft architecture was preliminarily studied, and tests highlighted the lack of an in-depth analysis of this crucial component, favouring the pursuit of lightweight and small-size requirements, allowing movements even in confined spaces.

To fill this gap, this component behaviour was modelled by exploiting its equations of motion to simulate the whole hybrid architecture. The model was developed in the Simulink/Simscape environment of the MATLAB Software and then simulated.

This chapter will outline the hybrid-architecture multibody modelling and show some preliminary simulation results. It should be pointed out that the one presented is only a first step towards the complex analysis of the soft architecture and that the preliminary results achieved are not definitive.

## 5.1 Finger-handling mechanism modelling

The soft component was preliminarily studied in Section 3.1.2, but the analysis presented is not enough to describe its contribution to the hybrid architecture completely. Indeed, experimental tests revealed some flaws in the soft architecture, especially related to the high resistance to movement that increases as the component's stiffness increases. This variable, in turn, depends on multiple parameters, including the material stiffness and foil section geometry and sizes, which can lead to different foil behaviours. Given the multiple variables, developing alternative solutions to test would have been costly in terms of money and time. For these reasons, the multibody model of the hybrid-architecture finger mechanism, including the soft component, was developed in the Simscape environment to simulate its kinematic and dynamic behaviour and detect the best trade-off between material, section geometry and sizes.

For this first study, the thumb-handling mechanism was considered for two main reasons: the first related to the fact that the analyses on the hybrid architecture were all initially performed on the thumb, as it was the missing finger in the previous prototypes; the second, instead, associated with its greater simplicity due to the presence of one less phalanx. However, while rigid-multibody modelling in Simscape is a well-known procedure thanks to the specific Multibody tool available in the Simulink libraries, the same straightforwardness is not found while modelling the soft architecture.

For what concerns the rigid architecture, the procedure runs as follows. Firstly, three blocks from the Simscape libraries defining the *Mechanism Configuration*, *World Frame*, and *Solver Configuration* must be dragged into a Simulink blank model to set the fixed reference frame orientation and solver parameters to use for simulation. Then, the linkage mechanism can be built by adding blocks to introduce its bars and joints in the model. Specifically, the bars' geometry is imported through their file .step generated in SolidWorks (the path file can be selected in the *Body Element File Solid* block), while *Revolute Joint* blocks model mechanism hinges. The *Body Element* block is fundamental to define reference frames integral to the matching rigid body through which the mechanism is assembled. Once the model is built, the mechanism can be actuated by imposing specific trajectories or torques on the joints, while their position, velocity, acceleration, and torque can be measured through the sensing functionality. The block diagram for the rigid architecture of the thumb-handling mechanism and the resulting model visualisation, once run, are shown in Figure 5.1. It is worth highlighting that, by the kinematic analysis in Section 3.1.1, the 1-DOF linkage mechanism closes on the proximal phalanx; therefore,

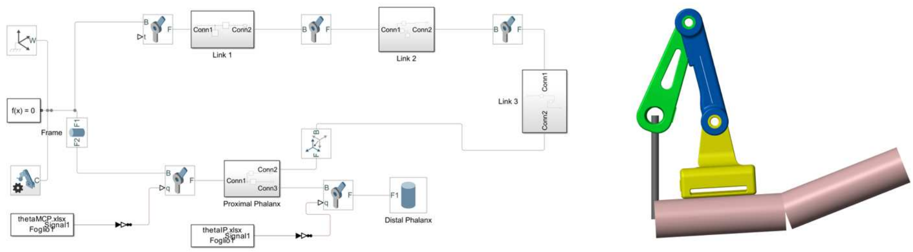


Figure 5.1: The block diagram of the rigid architecture of the thumb-handling mechanism developed in Simscape, on the left, and its resulting visualisation in Mechanics Explorer, on the right.

it is enough to provide the $\theta_{MCP}$ joint with its desired trajectory to achieve the desired motion.

Greater complexity was instead found in modelling the soft architecture. Indeed, even if Simscape provides tools for flexible bodies, it was not possible to model with existing blocks the particular soft-architecture behaviour, whereby, due to the relative movement of the mechanism bars, the flat spring must slide into one of them, in turn, causing the distal-phalanx flexion. Therefore, to introduce the soft component to the hybrid architecture model, it was chosen to use its equations of motion, and in particular to solve them within a *MATLAB Function* block (among the *User-Defined Functions*, present in the Simulink libraries as well) to introduce into the block diagram in Simscape.

The main output of the *MATLAB Function*, which solves the system equations of motion, is the system accelerations vector $\ddot{\mathbf{X}}$, assuming $\mathbf{X}$ corresponding to the system's state vector. By integrating vector $\ddot{\mathbf{X}}$ twice, it is possible to derive the velocities $\dot{\mathbf{X}}$ and positions $\mathbf{X}$ vectors to return as input to the *MATLAB Function*. In addition, vector $\mathbf{d}$, including a set of variables sensed from the rigid architecture, is introduced as input as well, while interaction forces, as forces $F$ and torque $M$, between the two architectures are derived in the *MATLAB Function*, and then applied to the rigid architecture. The outline of this model can be seen in Figure 5.2

To solve the soft component equations of motion, it is necessary to choose a modelling method. No similar applications were found in the literature. However, various approaches to the multibody dynamics problems can be detected, among which the floating frame of reference, incremental, large rotation vector formulations or the finite segment method [122, 123, 124]. This last formulation

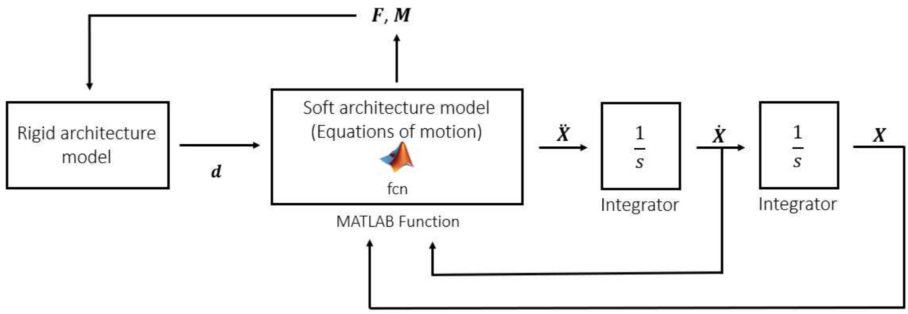


Figure 5.2: The outline of the hybrid-architecture finger-handling mechanism model.

differs from the previous ones since, if the former is based on the finite element method, the finite segment one involves considering the deformable body as a set of bodies connected by springs and dampers [122]. This technique has the advantage that rigid-body methods can be used to formulate equations of motion for deformable bodies [122]. Although the finite element method might allow for more accurate results, the finite segment one requires higher simplicity of modelling and lower computational cost. For these reasons, this case study considered an approach similar to the finite segment method.

Assuming that the finger-handling mechanism soft component of length $L$ is divided into $n$ equal elements connected by springs and dampers, its equations of motion can be derived from the following equations valid for the $i$-th element (it is worth noting that unless otherwise indicated, vectors refer to the fixed reference system $O_f x_f y_f$):

$$M_i \ddot{\mathbf{G}}_i = \mathbf{F}_{i-1,i} + \mathbf{F}_{i+1,i} + \mathbf{F}_i^{est} \quad (5.1)$$

$$I_i \ddot{\phi}_i = T_{i-1,i} + T_{i+1,i} + T_i^{est} \quad (5.2)$$

where $M_i$ and $I_i$ are the mass matrix and inertia of the $i$-th element, $\ddot{\mathbf{G}}_i = [\ddot{X}_i \; \ddot{Y}_i]'$ is the acceleration vector of the $i-th$ element center of mass, in which $\ddot{X}_i$ and $\ddot{Y}_i$ are its Cartesian coordinates, while $\ddot{\phi}_i$ is its angular acceleration. $\mathbf{F}_i^{est}$ and $T_i^{est}$ represent the external forces and moments acting on the $i$-th element. Finally, $\mathbf{F}_{i-1,i}$ and $\mathbf{F}_{i+1,i}$ indicate forces acting on the $i$-th element due to the interaction with the previous $i-1$ and next $i+1$ elements, while $T_{i-1,i}$ and $T_{i+1,i}$ are the corresponding moments. Such forces and moments can

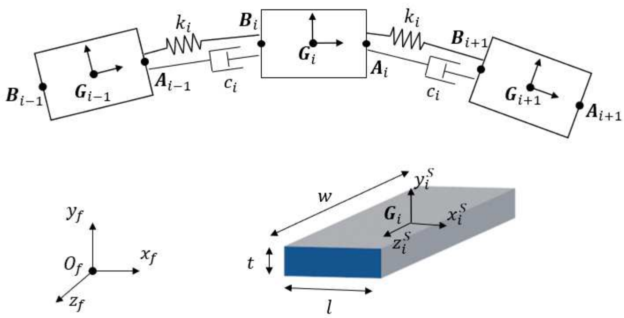


Figure 5.3: The $i$-th element of the soft component: the $O_f x_f y_f$ is the fixed reference frame, while $O_s x_s y_s$ is the one integral to the $i$-th element.

be split into the elastic and damping contributions as follows:

$$\mathbf{F}_{i-1,i} = \mathbf{F}_{i-1,i}{}^{el} + \mathbf{F}_{i-1,i}{}^{dam} \tag{5.3}$$

$$T_{i-1,i} = T_{i-1,i}{}^{el} + T_{i-1,i}{}^{dam} \tag{5.4}$$

$$\mathbf{F}_{i+1,i} = \mathbf{F}_{i+1,i}{}^{el} + \mathbf{F}_{i+1,i}{}^{dam} \tag{5.5}$$

$$T_{i+1,i} = T_{i+1,i}{}^{el} + T_{i+1,i}{}^{dam} \tag{5.6}$$

Referring to Figure 5.3, for the $i$-th element it is valid that $\mathbf{A}_i = \mathbf{G}_i + R(\phi_i)\mathbf{A}_i{}^S$ and $\mathbf{B}_i = \mathbf{G}_i + R(\phi_i)\mathbf{B}_i{}^S$, where $R(\phi_i)$ is the $z$-axis rotation matrix of the angle $\phi_i$, while $\mathbf{A}_i{}^S = [\frac{l}{2}\ 0]'$ and $\mathbf{B}_i{}^S = [-\frac{l}{2}\ 0]'$ are the position vector of points $\mathbf{A}_i$ and $\mathbf{B}_i$ referred to the frame integral to the $i$-th element and centred in $\mathbf{G}_i$. Bearing in mind such considerations, elastic and damping contributions in Equations 5.3 and 5.4 can be expressed as reported below (for the sake of brevity, from now on, contributions due to the interactions with the $(i+1)$-th element are not reported, but can be evaluated analogously to those due to the $(i-1)$-th element:

$$\mathbf{F}_{i-1,i}{}^{el} = k_i(\mathbf{A}_{i-1} - \mathbf{B}_i) = k_i(\mathbf{G}_{i-1} + R(\phi_{i-1})\mathbf{A}^S{}_{i-1} - \mathbf{G}_i - R(\phi_i)\mathbf{B}^S{}_i) \tag{5.7}$$

$$\mathbf{F}_{i-1,i}{}^{dam} = c_i(\dot{\mathbf{A}}_{i-1} - \dot{\mathbf{B}}_i) = c_i(\dot{\mathbf{G}}_{i-1} + R'(\phi_{i-1})\mathbf{A}^S{}_{i-1}\dot{\phi}_{i-1} - \dot{\mathbf{G}}_i - R'(\phi_i)\mathbf{B}^S{}_i\dot{\phi}_i) \tag{5.8}$$

$$T_{i-1,i}{}^{el} = k_{f\,i}(\phi_{i-1} - \phi_i) + [(\mathbf{B}_i - \mathbf{G}_i) \wedge \mathbf{F}_{i-1,i}{}^{el}]_z = k_{f\,i}(\phi_{i-1} - \phi_i) + \\ + [S(R(\phi_i)\mathbf{B}^S{}_i)k_i]_z(\mathbf{G}_{i-1} + R(\phi_{i-1})\mathbf{A}^S{}_{i-1} - \mathbf{G}_i - R(\phi_i)\mathbf{B}^S{}_i) \quad (5.9)$$

$$T_{i-1,i}{}^{dam} = c_{f\,i}(\dot{\phi_{i-1}} - \dot{\phi}_i) + [(\mathbf{B}_i - \mathbf{G}_i) \wedge \mathbf{F}_{i-1,i}{}^{sm}]_z = c_{f\,i}(\dot{\phi_{i-1}} - \dot{\phi}_i) + \\ + [S(R(\phi_i)\mathbf{B}^S{}_i)c_i]_z(\dot{\mathbf{G}}_{i-1} + R'(\phi_{i-1})\mathbf{A}^S{}_{i-1}\dot{\phi}_{i-1} - \dot{\mathbf{G}}_i - R'(\phi_i)\mathbf{B}^S{}_i\dot{\phi}_i) \quad (5.10)$$

In these equations, $k_i$ and $c_i$ correspond to the $i$-th element stiffness and damping matrix, while $k_{f\,i}$ and $c_{f\,i}$ are bending stiffness and damping of the $i$-th element, and will be detailed below. $S(R(\phi_i)\mathbf{B}^S)$ indicates the antisymmetric matrix of its argument.
After defining the following terms

$$\mathbf{n}^{el}{}_{i-1,i} = [S(R(\phi_i)\mathbf{B}^S{}_i)k_i]_z \quad (5.11)$$
$$\mathbf{n}^{dam}{}_{i-1,i} = [S(R(\phi_i)\mathbf{B}^S{}_i)c_i]_z \quad (5.12)$$
$$\mathbf{q}^{el}{}_{i-1,i} = k_i(R(\phi_{i-1})\mathbf{A}^S{}_{i-1} - R(\phi_i)\mathbf{B}^S{}_i) \quad (5.13)$$
$$r^{el}{}_{i-1,i} = \mathbf{n}^{el}{}_{i-1,i}(R(\phi_{i-1})\mathbf{A}^S{}_{i-1} - R(\phi_i)\mathbf{B}^S{}_i) \quad (5.14)$$
$$\mathbf{s}^{dam}{}_{i-1,i} = c_i(R'(\phi_{i-1})\mathbf{A}^S{}_{i-1}\dot{\phi}_{i-1} - R'(\phi_i)\mathbf{B}^S{}_i\dot{\phi}_i) \quad (5.15)$$
$$v^{dam}{}_{i-1,i} = \mathbf{n}^{dam}{}_{i-1,i}(R'(\phi_{i-1})\mathbf{A}^S{}_{i-1}\dot{\phi}_{i-1} - R'(\phi_i)\mathbf{B}^S{}_i\dot{\phi}_i) \quad (5.16)$$

and the state vector of the $i$-th element $\mathbf{X}_i$ as $\mathbf{X}_i = [\mathbf{G}_i\ \phi_i]'$, Equations 5.1 and 5.2 can be written in the following matrix form:

$$M_i\ddot{\mathbf{X}}_i = \begin{bmatrix} k_i & \begin{bmatrix}0\\0\end{bmatrix} \\ \mathbf{n}^{el}{}_{i-1,i} & k_{f\,i} \end{bmatrix} \mathbf{X}_{i-1} + \begin{bmatrix} c_i & \begin{bmatrix}0\\0\end{bmatrix} \\ \mathbf{n}^{dam}{}_{i-1,i} & c_{f\,i} \end{bmatrix} \dot{\mathbf{X}}_{i-1} + \\ \begin{bmatrix} -2k_i & \begin{bmatrix}0\\0\end{bmatrix} \\ -\mathbf{n}^{el}{}_{i-1,i} - \mathbf{n}^{el}{}_{i+1,i} & -2k_{f\,i} \end{bmatrix} \mathbf{X}_i + \begin{bmatrix} -2c_i & \begin{bmatrix}0\\0\end{bmatrix} \\ -\mathbf{n}^{dam}{}_{i-1,i} - \mathbf{n}^{dam}{}_{i+1,i} & -2c_{f\,i} \end{bmatrix} \dot{\mathbf{X}}_i + \\ \begin{bmatrix} k_i & \begin{bmatrix}0\\0\end{bmatrix} \\ \mathbf{n}^{el}{}_{i+1,i} & k_{f\,i} \end{bmatrix} \mathbf{X}_{i+1} + \begin{bmatrix} c_i & \begin{bmatrix}0\\0\end{bmatrix} \\ \mathbf{n}^{sm}{}_{i+1,i} & c_{f\,i} \end{bmatrix} \dot{\mathbf{X}}_{i+1} + \\ \begin{bmatrix} \mathbf{q}^{el}{}_{i-1,i} \\ r^{el}{}_{i-1,i} \end{bmatrix} + \begin{bmatrix} \mathbf{s}^{dam}{}_{i-1,i} \\ v^{dam}{}_{i-1,i} \end{bmatrix} + \begin{bmatrix} \mathbf{q}^{el}{}_{i+1,i} \\ r^{el}{}_{i+1,i} \end{bmatrix} + \begin{bmatrix} \mathbf{s}^{dam}{}_{i+1,i} \\ v^{dam}{}_{i+1,i} \end{bmatrix} + \begin{bmatrix} \mathbf{F}_i^{est} \\ T_i^{est} \end{bmatrix} \quad (5.17)$$

By combining the matrices to write the equations of motion of all the elements' centre of mass into which the soft component was divided, the following matrix equation can be derived:

$$M\ddot{\mathbf{X}} = C\dot{\mathbf{X}} + K\mathbf{X} + \mathbf{f}^{el} + \mathbf{f}^{dam} + \mathbf{f}^{est} \tag{5.18}$$

where $M \in R^{3n\times 3n}$, $\ddot{\mathbf{X}} \in R^{3n}$, $\dot{\mathbf{X}}, \mathbf{X} \in R^{3(n+2)}$ since the pose of the attachment points of the bodies with which the foil interacts was also introduced, and thus $C, K \in R^{3n\times 3(n+2)}$. $\mathbf{f}^{el}, \mathbf{f}^{dam} \in R^{3(n+2)}$ include the secondary contribution to forces and moments due to elastic and damping effects, respectively, on each element as defined in Equations from 5.13 to 5.16, while $\mathbf{f}^{est} \in R^{3(n+2)}$ represents all the external forces acting on each element, among which the contact ones.

However, before introducing the contact model, the terms $M_i$, $I_i$, $k_i$, and $c_i$ must be defined to construct the matrices in Equation 5.18. Every element of the soft component was treated as a 1D beam, in which normal, shear, and bending stresses are considered (Timoshenko theory). Bearing in mind the reference frame in Figure 5.3, the stress tensor is as follows:

$$\sigma = \begin{bmatrix} \sigma_{xx} & \sigma_{xy} & \sigma_{xz} \\ \sigma_{yx} & \sigma_{yy} & \sigma_{yz} \\ \sigma_{zx} & \sigma_{zy} & \sigma_{zz} \end{bmatrix} \tag{5.19}$$

in which $\sigma_{xz} = \sigma_{xz} = 0$, $\sigma_{yz} = \sigma_{zy} = 0$, $\sigma_{yy} = 0$, and $\sigma_{zz} = 0$ since the motion is considered to develop in the plane, and that torsion ($\sigma_{yz} = \sigma_{zy}$) and traction/compression along $y$ ($\sigma_{yy}$) and $z$ ($\sigma_{zz}$) axes are neglected.

At this point of the study, only pure normal, shear, and bending stresses were considered by neglecting mixed contributions. Therefore, given these premises, the stiffness matrix of the $i$-th element was defined as

$$k_i = \begin{bmatrix} \frac{EA}{l} & 0 \\ 0 & \frac{GA}{l} \end{bmatrix} \tag{5.20}$$

in which $E$ and $G$ indicate the material elastic and shear modulus, and $A$ the element transversal area ($A = wt$). The bending stiffness $k_{f\,i}$ is determined as $k_{f\,i} = \frac{EI_z}{l}$, in which $I_z$ is the axial moment of inertia of the section referred to $z$ axis ($I_z = \frac{wt^3}{12}$).

Since considering a plane motion, the mass matrix to multiply to the Cartesian coordinate $\mathbf{G}_i$ is defined as

$$M_i = \begin{bmatrix} m_i & 0 \\ 0 & m_i \end{bmatrix} \tag{5.21}$$

while the inertia moment of the $i$-th element referred to its centre of mass is $I_i = \frac{m_i(t^2+l^2)}{12}$. $m_i$ is determined as $m_i = \rho wtl$, in which $\rho$ in the material density. If the component is divided into elements of equal length, they all have the same mass.

The $i$-th element damping matrix instead was determined based on the formulation of the proportional Rayleigh damping [125], according to which

$$c_i = \alpha M_i + \beta k_i \tag{5.22}$$

where $\alpha$ and $\beta$ are arbitrary constant coefficients that are related through the following equation:

$$\zeta = \frac{\alpha}{2\omega} + \beta\frac{\omega}{2} \tag{5.23}$$

Here, $\zeta$ indicates the viscous damping ratio, while $\omega$ is the system's natural frequency. By imposing this equation under two different conditions $(\zeta_1, \omega_1)$ and $(\zeta_2, \omega_2)$, a system of two equations in two unknowns from which derive $\alpha$ and $\beta$ is obtained. The bending damping $c_{f_i}$ can be determined by following the same procedure.

After that, the contact model can be introduced as well. It is worth noting that the contact phenomenon allows for modelling the peculiar behaviour of the soft component of the finger-handling mechanism that slides into a rigid bar of the linkage mechanism. The literature is full of formulations that model contact in different ways, for instance, as a nonlinear spring along the collision direction, or which also considered losses through the damping effect in both the linear or nonlinear field [126, 127].
For this case study, the Hertz contact law was considered, and a damping term was added to model the contact as a nonlinear viscous-elastic spring damper element, thus correlating the indentation among the parts and the corresponding contact forces. For clarity, the following dissertation reports only contact on the element's bottom side, but it is analogous to the upper one.

Referring to Figure 5.4, the relative indentation is defined as ${\delta^D}_i = {\mathbf{n}^D}_i \cdot (\mathbf{Q}_i - \mathbf{D}_i)$, where $\mathbf{D}_i = \mathbf{G}_i + R(\phi){\mathbf{D}^S}_i = \mathbf{G}_i + R(\phi)[0 \ \ -\frac{t}{2} \ \ 0]'$ is the point in which the indentation is measured, and contact forces are considered applied. $\mathbf{Q}_i$ is instead the point belonging to the contacting body that is at the shortest

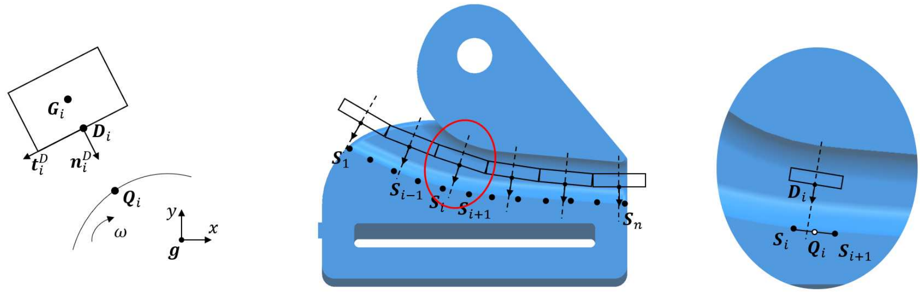


Figure 5.4: The contact model: on the left, the contact outline; on the centre, the search for a contact in Link 3; on the right, an enlargement showing the determination of the possible contact point.

distance from the element and is searched along the normal to the element itself, while $\mathbf{n}^D{}_i$ is the versor normal to the $i$-th element in its lower side. Points give the surface area of the contact component. To evaluate the contact point $\mathbf{Q}_i$ for each $i$-th element, the following steps have been carried out: the line perpendicular to the $i$-th element belonging to its centre of mass was calculated; then, the position of each point on the contact surface referred to this line was evaluated; once the points immediately before and after that ($\mathbf{S}_i$ and $\mathbf{S}_{i+1}$, respectively in Figure 5.4) were identified, point $\mathbf{Q}_i$ was determined as the midpoint between these. The same procedure is repeated for all the elements entering the possible contact region. The contact happens if the indentation $\delta^D{}_i$ thus evaluated is negative. Therefore, the normal contact force can be determined based on the chosen model as reported below:

$$\mathbf{N}^D{}_i = \begin{cases} 0 \quad \text{if} \quad \delta^D{}_i \geq 0 \\ -|\delta^D{}_i|^\alpha K_c \mathbf{n}^D{}_i - C_c \dot{\delta}_i^D \mathbf{n}^D{}_i \quad \text{if} \quad \delta^D{}_i < 0 \end{cases} \tag{5.24}$$

where $\dot{\delta}_i^D$ is the indentation rate and can be evaluated as $\dot{\delta}_i^D = \mathbf{n}^D{}_i \cdot (\dot{\mathbf{Q}}_i - \dot{\mathbf{D}}_i)$, and $\alpha$ is a geometry constant equal to $\frac{3}{2}$ by approximating the surfaces in the contact zone to spherical. $K_c$ and $C_c$ are the contact stiffness and damping. $C_c$ is considered as $0.01K_c$, while $K_c$ was hypothesised and tuned for the case study, bearing in mind that higher values cause higher contact force but lower indentation than lower values.

The sliding parameter $\mathbf{s}^D{}_i$ must be introduced concerning the tangential contact force. It is defined as $\mathbf{s}^D{}_i = ((\dot{\mathbf{Q}}_i - \dot{\mathbf{D}}_i) \cdot \mathbf{t}^D{}_i)\mathbf{t}^D{}_i$, where $\mathbf{t}^D{}_i$ is the tangential versor to the $i$-th element in its lower side. Specifically, the tangential force can be evaluated as follows:

$$\mathbf{T}^D{}_i = -f_i(\mathbf{s}^D{}_i)||\mathbf{N}^D{}_i||\frac{\mathbf{s}^D{}_i}{||\mathbf{s}^D{}_i|| + \epsilon} \tag{5.25}$$

where $\epsilon$ is any small constant to avoid denominator cancellations, while $f_i(\mathbf{s}^D{}_i)$ is the friction factor that is determined as a function of the sliding $\mathbf{s}^D{}_i$.

Among those available in the literature [128, 129], for this case study, the friction coefficient has been derived from a pseudo-Coulomb model, for which the static friction condition is established when bodies start sliding between each other that decreases to the kinetic value when their relative velocity increases. If the first part of the curve has a linear trend, the second part follows an exponential decrement as reported below and in Figure 5.5:

$$f_i(\mathbf{s}^D{}_i) = \begin{cases} ||\mathbf{s}^D{}_i|| \tan\alpha_f & \text{if} \quad ||\mathbf{s}^D{}_i|| < ||\mathbf{s}^D{}_i||^* \\ f_k + (f_s - f_k)\exp(-(\frac{||\mathbf{s}^D{}_i||}{||\mathbf{s}^D{}_i||^*})^2 & \text{if} \quad ||\mathbf{s}^D{}_i|| \geq ||\mathbf{s}^D{}_i||^* \end{cases} \tag{5.26}$$

In this equation, $\alpha_f$ indicates the line slope, $f_s$ and $f_k$ the static and kinetic friction coefficient, respectively, while $||\mathbf{s}^D{}_i||^*$ is the sliding value for which the transition between static and kinetic friction happens. It is essential to point out that the parameters $\alpha_f$ and $||\mathbf{s}^D{}_i||^*$ have to be alternatively tuned once $f_s$ is defined based on the components material.

## 5.2 Preliminary tests

Some preliminary tests were carried out for the case study to verify the model and tune the needed parameters. As mentioned, the first simulations were performed on the thumb-handling mechanism, assuming a flat spring length of 70 mm. The overall model was built as shown in Figure 5.2. From the rigid architecture, sensing the Cartesian and angular coordinates of position and velocity of Link 2, Link 3, and distal-phalanx EE (vector **d** in Figure 5.2) was required to evaluate interaction and contact forces between the rigid and soft architectures. In this case, indeed, contact has been modelled in Link 3 and distal-phalanx EE, while attachment points between the two architectures are in this last component and Link 2. These interaction forces were also modelled as a spring and damper, for which the damping $C$ was considered 1% of the stiffness $K$, which, in turn, was assumed to be an order of magnitude higher than contact stiffness.

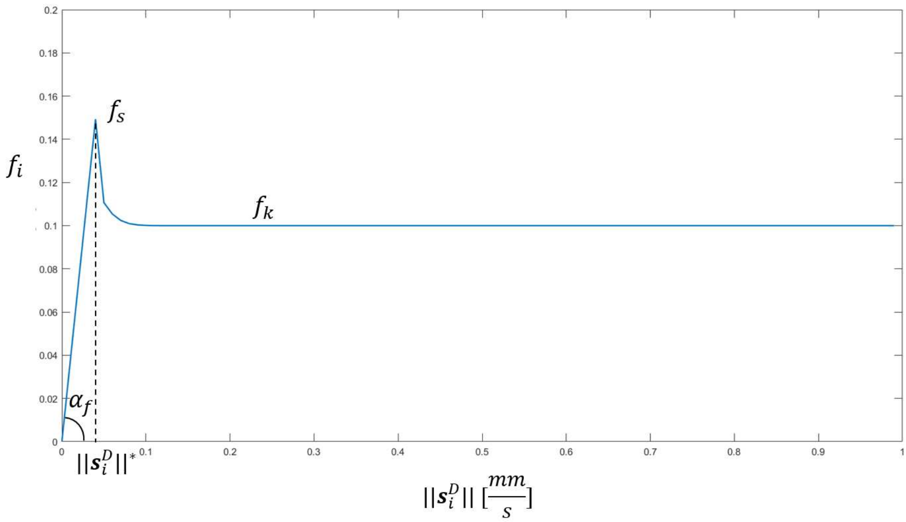


Figure 5.5: The friction model, in which $\alpha_f$, the limit sliding $||\mathbf{s}^D{}_i||^*$, and static $f_s$ and kinetic $f_k$ coefficient are highlighted.

After a series of iterations, discretising the flat spring with 70 elements, each 1 mm long, seemed to be a good compromise between computation time and the results obtained. It is important to point out that a limited number of elements also results in an overestimation of the contact forces since indentations, for example, in the entrance area of the foil in Link 3 can increase.
The integrator blocks need initial conditions of the variables to integrate. Since such blocks must integrate the acceleration vector $\ddot{\mathbf{X}}$, each element centre of mass velocities and positions at time 0 s must be defined. The initial condition for vector $\dot{\mathbf{X}}$ is set equal to the null vector, while those for vector $\mathbf{X}$ were detected from the CAD model of the finger-handling mechanism. It is worth noting that in this CAD model, the soft component must be discretised into an appropriate number of elements, the same in which it will be discretised in the model, bearing in mind that the number of the elements influences the simulation computational cost and results accuracy.
In this phase, giving as input point $\mathbf{B}$ of the first element and the angular coordinates of all the others made it possible not to introduce an initial error on the elements' position, making all the $\mathbf{B}_i$ points coincide with the $\mathbf{A}_{i-1}$ of the

previous one.
The variable-size daessc solver was chosen as recommended for the Simscape model. A relative and absolute tolerances of $10^-3$ and $10^-4$, respectively, were initially set for the solver.
To visualise the soft architecture behaviour on the Mechanics Explorer, a number of prismatic elements (through *Brick Solid* block) equal to that into which the soft component was discretised was introduced to the model, and the trajectory was imposed on them by giving as input to each the Cartesian and angular coordinates derived from the system state vector $\mathbf{X}$.
As for the rigid architecture, simulations of the overall hybrid architecture were initially performed by imposing trajectory to the MCP and IP joints through their desired angular coordinates, mentioned in Section 2.1.
Finally, material properties and element geometry must be defined.

First simulations were performed considering a flat spring in spring steel ($E$ = 206000 MPa, $G$ = 81500 MPa, $\rho$= 7.850*$10^{-6}$ kg/mm$^3$) with section 0.3$\times$10 mm$^2$. Due to the chosen material, it is valid that $\zeta$ <0.01 while $\omega$ can be assumed between 0 and 100 Hz. The parameters $\alpha$ and $\beta$ required to derive the damping matrix (Equation 5.22) were thus determined by imposing Equation 5.23 in two conditions, for which $(\zeta_1, \omega_1) = (0.01, 1)$ and $(\zeta_2, \omega_2) = (0.01, 100)$. A kinetic friction $f_k$ of 0.1 and a static friction $f_s = 1.5 f_k$ were considered for the application. The slope of the straight line, determined by $\alpha_f$, which represents friction at low velocities, was initially set by imposing the limit sliding $||\mathbf{s}^D{}_i||^*$ equal to 1% of the maximum sliding measured during a simulation. Due to this assumption, $||\mathbf{s}^D{}_i||^*$ and $\alpha_f$ resulted equal to 0.25 mm/s, and $\simeq$ 30°. Different stiffness $K_c$ were tested, deriving an appropriate behaviour in the range of 10000-15000, which determines maximum indentations on the order of millimetre tenths, as shown in Table 5.1. These maximum values are usually

| $K_c$ [N/mm] | 10000 | 12000 | 15000 |
|---|---|---|---|
| $\delta^D{}_{max}$ [mm] | 0.3053 | 0.2885 | 0.2308 |
| $\delta^U{}_{max}$ [mm] | 0.3445 | 0.3110 | 0.2757 |

Table 5.1: The maximum indentation in the bottom $\delta^D{}_{max}$ and top $\delta^U{}_{max}$ sides measured among all the elements during simulations performed for different values of the contact stiffness $K_c$.

reached in the maximum bending condition by the elements that are at the extremes of the contact region, while indentation values for elements far from these points are on the order of a tenth, if not even a hundredth of a millimetre.

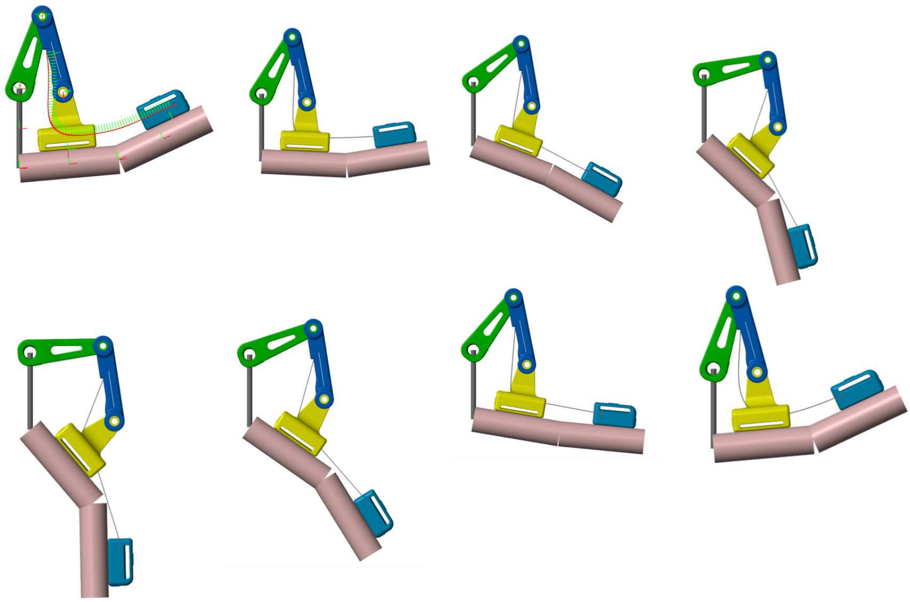

Figure 5.6: Pictures of the advancing simulation: in the first one, the reference frames integral to each element in which the soft component was discretised are highlighted.

By gradually increasing the straight-line slope, the indentation values are reduced. In particular, in the case of a contact stiffness $K_c$ of 10000 N/mm and $\alpha_f = 70°$, the corresponding maximum indentations resulted $\delta^D{}_{max} = 0.257$ mm and $\delta^U{}_{max} = 0.3426$ mm. It can be noted the reduced value of $\delta^D{}_{max}$ referring to that in Table 5.1, which still has room for improvement by increasing the contact stiffness.
Lower stiffness values compared to this range lead to higher indentation depth, while higher values increase the simulation time (it is worth noting that these simulations have an average duration of about 20 minutes). Higher slopes than those mentioned have not yet been tested.

Figure 5.6 shows some shots of the advancing simulation, revealing the goodness of the contact model that is appropriately detected in Link 2 and distal-phalanx EE, but also that of the spring itself, the dynamics of which is determined by solving their equations of motion.

Going into details of the material behaviour, the stresses to which each element is subjected were evaluated. In particular, the interaction forces among the elements were reported in the frame integral to each element, decomposing them in normal (N), shear (T) forces, and bending torque (M). Such loads were considered applied to one end of the element by framing the other for stress calculations, as reported below:

$$\sigma_{xx} = \frac{N}{A} + \frac{M}{EI} \tag{5.27}$$

$$\tau_{xy} = \frac{T}{A} \tag{5.28}$$

The equivalent stress $\sigma_{eq}$ was evaluated following the Von-Mises criterion, according to which $\sigma_{eq} = \sqrt{\sigma_{xx}{}^2 + 3\tau_{xy}{}^2}$.

By following such a procedure, the stress value $\sigma_{eq}$ measured in the case of $K_c = 10000$ N/mm and $\alpha_f = 70°$ reached 6107.9 MPa, which is much higher than the material admissible stress $\sigma_{adm} \simeq 1400$ MPa. However, the result is compatible with what was observed during the experimental tests, which revealed how the stiffness of the flat spring in spring steel does not allow it to cover the entire imposed ROM. If the flat spring was pulled up to this range, as imposed in the simulations, the material would not withstand. At the same time, it is worth noting that the highest stresses are measured for those elements that enter Link 3 due to the curvature that the flat spring undergoes in that area compared to those found elsewhere.

Other materials were preliminarily tested; in the case of polycarbonate and aluminium alloy, the cross-sectional area was $0.5 \times 10$ mm$^2$. Some results are summarised in Table 5.2.

| | E [MPa] | G [MPa] | $\rho$ [$\frac{kg}{mm^3}$] | $\sigma_{adm}$ [MPa] | $K_c$ [$\frac{N}{mm}$] | $\alpha_f$ [°] | $\delta^D{}_{max}$ [mm] | $\delta^U{}_{max}$ [mm] | $\sigma_{eq}$ [MPa] |
|---|---|---|---|---|---|---|---|---|---|
| Polycarbonate | 2400 | 870 | 1.2*10$^{-6}$ | 70 | 10000 | 70 | 0.2885 | 0.1454 | 2286.7 |
| High-strength stainless steel | 193000 | 86200 | 7.93*10$^{-6}$ | 1700 | 15000 | 30 | 0.3933 | 0.2309 | 6515.4 |
| Aluminum alloy (6061) | 68900 | 26000 | 2.7*10$^{-6}$ | 280 | 10000 | 30 | 0.2285 | 0.2765 | 3687.7 |

Table 5.2: The results obtained by preliminary simulations carried out with different materials for the soft component.

It is evident that a combination of element geometry, material, and contact properties that do not result in excessive element stress has not yet been identified. Indeed, even if varying the contact stiffness can reduce maximum indentation values, the stresses measured on the elements (maximum in correspondence with the curvature) are still too high. The model allows to observe that the change in foil curvature mainly contributes to these stresses and that materials with greater stiffness than others tend to reach higher stresses when pulled up to the imposed range if the same cross-section is considered. This aspect can be attributed to the greater resistance such materials offer to bend, as also revealed by the experimental tests comparing the performances of the exoskeleton equipped with spring steel or polycarbonate foils. Due to these preliminary findings, a design of Link 3 that allows this curvature to be softened could improve such results. In addition, the element foil geometry could be varied, for instance, by reducing its thickness within the limits of the manufacturing processes or the cross-sectional area to reduce each element's stiffness. For the same purpose, materials with different stiffness can be considered for simulations.

Therefore, while some parameters still need fine-tuning and preliminary results did not show a solution suitable for the application, early results show that the model approximates the foil's behaviour quite well. However, experimental validation is still needed to confirm this and future developments will focus on this aspect.

# Chapter 6

# Conclusions

This work collects part of the research activities on Wearable Robotics carried out at the Mechatronics and Dynamic Modelling Laboratory of the Department of Industrial Engineering at the University of Florence from November 2020 to January 2024. This Ph.D. research activity stands in the broad Wearable Robotics for the Healthcare System field. These pages focused on the path taken to develop a new hand exoskeleton for assisting users in Activities of Daily Living to regain their independence and improve their quality of life.
Specifically, hand exoskeletons are considered special tools that allow users with hand impairments to interact with the environment by restoring their functional capabilities. The World Health Organisation declared in 2022 that the world population age is steadily increasing, and the same goes for chronic diseases, thus determining a growing number of people with disabilities. Therefore, research in these areas focuses on developing low-cost assistive and rehabilitative devices for use in daily life to support primary activities and be integrated with functional recovery processes.

The research activity presented in this thesis is precisely in this context. Specifically, it focuses on developing a hand exoskeleton following the design requirements for assistive purposes, which are still largely unmet. The research began with an in-depth literature search, which had two main purposes: first, to identify the primary design requirements that assistive hand exoskeletons should meet, and second, to provide an overview of current state-of-the-art technologies for pursuing them. The primary design requirements can be summarised with wearability, portability, lightness, small overall size, safety, comfort, dexterity, efficacy in ADLs, sense-of-touch preservation, and last but not least, affordability, as detailed in Chapter 1. However, the state of the art does not present devices meeting all these requirements. Even the latest hand exoskeleton prototype developed by the research group of the MDM Lab could not satisfy them all but lacked dexterity, lightness, small overall dimensions, and comfort, as Chapter 2 showed, in which the results achieved by performing an ARAT were reported.

Therefore, the design process for developing the new exoskeleton focused initially on how to pursue these requirements, thus outlining its main features. The novel hand exoskeleton is entirely wearable and portable thanks to the lightness and small overall dimensions of its two main modules: one to connect to the hand enclosing the actuation system and finger-handling mechanisms, and the other one to fix to the upper limb, housing the electronic components and power supply system. The hand module's mass and size are mainly due to the actuation system implemented into the device. Five micro metal gearmotors were coupled with straight bevel gear to provide the device with dexterity, ensured by independent finger and bidirectional motion, and by introducing the thumb-handling mechanism, not included in the previous MDM Lab prototypes. The size above the fingers is instead due to the finger-handling mechanism architecture.

In this thesis, an innovative hybrid architecture was presented. It involves rigid and soft components so that the mechanism can effectively transmit force while keeping the overall dimensions above the matching finger contained. Specifically, the well-known four-bar mechanism architecture is exploited to flex and extend the proximal phalanx in which acts and determines a RCM in the MCP joint, thus ensuring alignment between the finger and the matching mechanism and preventing wrong and painful motion. This aspect, along with the fact that the device is tailored to the user's hand anatomy since a kinematic optimisation procedure was exploited to determine the mechanism bar dimensions, add safety, and promote comfort to the device. The distal-phalanx f/e is instead determined by a flat spring sliding into a bar of the rigid mechanism.

The sense of touch is preserved by using Velcro straps and elastic bands to connect the device to the hand. The low device cost, thanks to the careful selection of materials, components, and manufacturing processes, makes it affordable. Most components were indeed in-house 3D printed in ABS-CF10, while the commercial ones were purchased.

The overall design process is reported in this thesis (Chapter 3): from the kinematic and kinetostatic analyses performed on the single finger-handling mechanism to the development of the whole hand exoskeleton, going through the design and analysis of the actuation system.

The first prototype of the thumb-handling mechanism was tested in terms of achievable ROM, verifying that the hybrid architecture does not limit it, and the exerted forces, showing that the target force is rather reached ($\simeq$ 10.6 N), as reported in Chapter 4. The promising results led to the development of the whole hand exoskeleton shown in Figure 6.1 and the evaluation of its grasping and pinching force capabilities. Two device's embodiments, sewn or not to

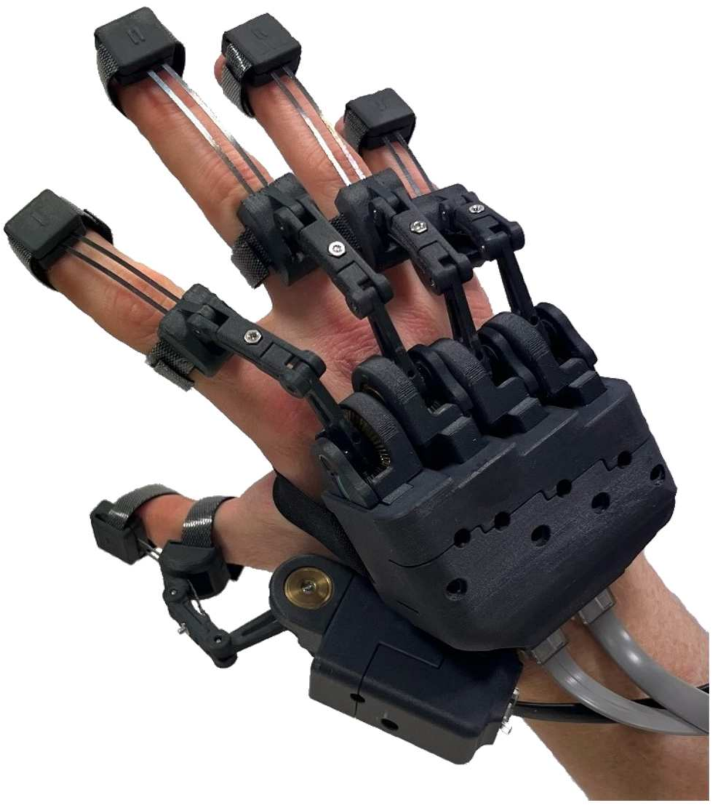

Figure 6.1: The assistive hand exoskeleton developed during this research activity.

a glove, were tested, measuring the gripping force with load cells and FSR, respectively. Force tests revealed that the device enables the subject wearing

it to grasp, hold, and manipulate the proposed items. The forces measured (in grasp tasks, $\simeq 16.7$ N and $\simeq 19.4$ N, depending on the object size, and in pinch task, $\simeq 7.4$ N) are greater than or similar to the values detected in the literature. The load cells provided higher accuracy and a wider range of measurement than FSRs, while the glove increased the exoskeleton adherence to the hand compared to using only Velcro straps. However, further improvements in the measurement instrument and interface between the hand and exoskeleton, ensuring the correct force transmission and kinematic coupling to the finger-handling mechanism, are required to achieve the target force. Therefore, in the near future, developing a compliant interface that prevents these issues and integrates a system for the thumb module opposition is needed to allow the device usage for prolonged periods without annoyance and improve efficacy in ADLs.
In addition to the interface, the soft component stiffness compromises the force transmission to the finger and its handling mechanism due to the high resistance it feels, preventing the full ROM coverage.
To perform an in-depth analysis of the soft component and overcome this last flaw, the hybrid architecture was modelled in Simscape/Simulink, as reported in Chapter 5, by solving the equations of motion of the elements in which the foil was discretised according to the finite segment method. Contact forces allow to model the soft component sliding in a bar of the rigid architecture. Preliminary results obtained from the first simulations are in accordance with what was found with experimental tests. However, conclusions cannot yet be drawn due to the few results the model has had so far. More findings are needed to detect the best solution for the hybrid architecture.

All these topics, whose investigation constitutes a natural continuation of the research activity carried out thus far, will be subjected to further developments.

# References

[1] N. G. Hockstein, C. Gourin, R. Faust, and D. J. Terris, “A history of robots: from science fiction to surgical robotics,” *Journal of robotic surgery*, vol. 1, pp. 113–118, 2007.

[2] A. M. Okamura, M. J. Matarić, and H. I. Christensen, “Medical and health-care robotics,” *IEEE Robotics & Automation Magazine*, vol. 17, no. 3, pp. 26–37, 2010.

[3] A. A. Morgan, J. Abdi, M. A. Syed, G. E. Kohen, P. Barlow, and M. P. Vizcaychipi, “Robots in healthcare: a scoping review,” *Current Robotics Reports*, vol. 3, no. 4, pp. 271–280, 2022.

[4] A. Attanasio, B. Scaglioni, E. De Momi, P. Fiorini, and P. Valdastri, “Autonomy in surgical robotics,” *Annual Review of Control, Robotics, and Autonomous Systems*, vol. 4, pp. 651–679, 2021.

[5] A. Cieza, “Rehabilitation the health strategy of the 21st century, really?,” *Archives of physical medicine and rehabilitation*, vol. 100, no. 11, pp. 2212–2214, 2019.

[6] M. den Hollander and A. Hoekstra, “Hand function in children with congenital disorders,” in *Hand Function*, pp. 189–200, Springer, 2019.

[7] C. M. Chew, “Caregiver shortage reaches critical stage,” *Provider (Washington, DC)*, vol. 43, no. 5, pp. 14–28, 2017.

[8] A. Budreviciute, S. Damiati, D. K. Sabir, K. Onder, P. Schuller-Goetzburg, G. Plakys, A. Katileviciute, S. Khoja, and R. Kodzius, “Management and prevention strategies for non-communicable diseases (ncds) and their risk factors,” *Frontiers in public health*, vol. 8, p. 788, 2020.

[9] A. Mohebbi, "Human-robot interaction in rehabilitation and assistance: a review," *Current Robotics Reports*, vol. 1, pp. 131–144, 2020.

[10] J. L. Pons, *Wearable robots: biomechatronic exoskeletons.* John Wiley & Sons, 2008.

[11] J. T. Meyer, R. Gassert, and O. Lambercy, "An analysis of usability evaluation practices and contexts of use in wearable robotics," *Journal of NeuroEngineering and Rehabilitation*, vol. 18, no. 1, pp. 1–15, 2021.

[12] K. G. Davis, C. R. Reid, D. D. Rempel, and D. Treaster, "Introduction to the human factors special issue on user-centered design for exoskeleton," 2020.

[13] F. Molteni, G. Gasperini, G. Cannaviello, and E. Guanziroli, "Exoskeleton and end-effector robots for upper and lower limbs rehabilitation: narrative review," *PM&R*, vol. 10, no. 9, pp. S174–S188, 2018.

[14] S. F. Duncan, C. E. Saracevic, and R. Kakinoki, "Biomechanics of the hand," *Hand clinics*, vol. 29, no. 4, pp. 483–492, 2013.

[15] M. T. Duruoz, *Hand function.* Springer, 2016.

[16] P. F. Edemekong, D. L. Bomgaars, S. Sukumaran, and C. Schoo, "Activities of daily living," in *StatPearls [Internet]*, StatPearls Publishing, 2022.

[17] E. Carmeli, H. Patish, and R. Coleman, "The aging hand," *The Journals of Gerontology Series A: Biological Sciences and Medical Sciences*, vol. 58, no. 2, pp. M146–M152, 2003.

[18] N. A. İncel, "Functional assessment in geriatric hand," in *Hand Function*, pp. 211–225, Springer, 2019.

[19] C. Duret, A.-G. Grosmaire, and H. I. Krebs, "Robot-assisted therapy in upper extremity hemiparesis: overview of an evidence-based approach," *Frontiers in neurology*, vol. 10, p. 412, 2019.

[20] T. du Plessis, K. Djouani, and C. Oosthuizen, "A review of active hand exoskeletons for rehabilitation and assistance," *Robotics*, vol. 10, no. 1, p. 40, 2021.

[21] F. Aggogeri, T. Mikolajczyk, and J. O'Kane, "Robotics for rehabilitation of hand movement in stroke survivors," *Advances in Mechanical Engineering*, vol. 11, no. 4, p. 1687814019841921, 2019.

[22] H. Rodgers, H. Bosomworth, H. I. Krebs, F. van Wijck, D. Howel, N. Wilson, L. Aird, N. Alvarado, S. Andole, D. L. Cohen, *et al.*, "Robot assisted training for the upper limb after stroke (ratuls): a multicentre randomised controlled trial," *The Lancet*, vol. 394, no. 10192, pp. 51–62, 2019.

[23] S. Regal, S. Maschke, and Z.-M. Li, "Hand and wrist biomechanics," in *Frontiers in Orthopaedic Biomechanics*, pp. 89–104, Springer, 2020.

[24] Y. Liu, L. Jiang, H. Liu, and D. Ming, "A systematic analysis of hand movement functionality: qualitative classification and quantitative investigation of hand grasp behavior," *Frontiers in Neurorobotics*, vol. 15, p. 658075, 2021.

[25] T. Feix, J. Romero, H.-B. Schmiedmayer, A. M. Dollar, and D. Kragic, "The grasp taxonomy of human grasp types," *IEEE Transactions on human-machine systems*, vol. 46, no. 1, pp. 66–77, 2015.

[26] M. Vergara, J. L. Sancho-Bru, V. Gracia-Ibáñez, and A. Pérez-González, "An introductory study of common grasps used by adults during performance of activities of daily living," *Journal of Hand Therapy*, vol. 27, no. 3, pp. 225–234, 2014.

[27] D. T. Wade, "What is rehabilitation? an empirical investigation leading to an evidence-based description," 2020.

[28] O. Lambercy, R. Ranzani, and R. Gassert, "Robot-assisted rehabilitation of hand function," in *Rehabilitation Robotics*, pp. 205–225, Elsevier, 2018.

[29] A. A. J. Ortega, M. D. L. A. O. Del, P. Hellström, E. Åstrand, M. Ekström, *et al.*, "On understanding the role of exoskeleton robots in hand rehabilitation: A brief review," in *2022 8th International Engineering, Sciences and Technology Conference (IESTEC)*, pp. 432–439, IEEE, 2022.

[30] X. Huang, F. Naghdy, G. Naghdy, H. Du, and C. Todd, "Robot-assisted post-stroke motion rehabilitation in upper extremities: a survey," *International Journal on Disability and Human Development*, vol. 16, no. 3, pp. 233–247, 2017.

[31] Z. Yue, X. Zhang, and J. Wang, "Hand rehabilitation robotics on post-stroke motor recovery.," *Behavioural neurology*, 2017.

[32] R. Kabir, M. S. H. Sunny, H. U. Ahmed, and M. H. Rahman, "Hand rehabilitation devices: a comprehensive systematic review," *Micromachines*, vol. 13, no. 7, p. 1033, 2022.

[33] S. Bhujel and S. Hasan, "A comparative study of end-effector and exoskeleton type rehabilitation robots in human upper extremity rehabilitation," *Human-Intelligent Systems Integration*, pp. 1–32, 2023.

[34] C. N. Schabowsky, S. B. Godfrey, R. J. Holley, and P. S. Lum, "Development and pilot testing of hexorr: hand exoskeleton rehabilitation robot," *Journal of neuroengineering and rehabilitation*, vol. 7, pp. 1–16, 2010.

[35] M. Bouzit, G. Burdea, G. Popescu, and R. Boian, "The rutgers master ii-new design force-feedback glove," *IEEE/ASME Transactions on mechatronics*, vol. 7, no. 2, pp. 256–263, 2002.

[36] L. Dovat, O. Lambercy, R. Gassert, T. Maeder, T. Milner, T. C. Leong, and E. Burdet, "Handcare: a cable-actuated rehabilitation system to train hand function after stroke," *IEEE Transactions on Neural Systems and Rehabilitation Engineering*, vol. 16, no. 6, pp. 582–591, 2008.

[37] Y. Tian, H. Wang, B. Niu, Y. Zhang, J. Du, J. Niu, and L. Sun, "Mechanical design and analysis of the end-effector finger rehabilitation robot (efrr) for stroke patients," *Machines*, vol. 9, no. 6, p. 110, 2021.

[38] J. A. Diez, A. Blanco, J. M. Catalán, F. J. Badesa, L. D. Lledó, and N. Garcia-Aracil, "Hand exoskeleton for rehabilitation therapies with integrated optical force sensor," *Advances in Mechanical Engineering*, vol. 10, no. 2, p. 1687814017753881, 2018.

[39] P. Milia, M. C. Peccini, F. De Salvo, A. Sfaldaroli, C. Grelli, G. Lucchesi, N. Sadauskas, C. Rossi, M. Caserio, M. Bigazzi, *et al.*, "Rehabilitation with robotic glove (gloreha) in poststroke patients," *Digital Medicine*, vol. 5, no. 2, p. 62, 2019.

[40] F. Zhang, L. Lin, L. Yang, and Y. Fu, "Design of an active and passive control system of hand exoskeleton for rehabilitation," *Applied Sciences*, vol. 9, no. 11, p. 2291, 2019.

[41] L. Zhao, C. Xie, and R. Song, "Design and validation of a wearable hand exoskeleton system," in *2020 5th International Conference on Advanced Robotics and Mechatronics (ICARM)*, pp. 559–563, IEEE, 2020.

[42] M. Haghshenas-Jaryani, R. M. Patterson, N. Bugnariu, and M. B. Wijesundara, "A pilot study on the design and validation of a hybrid exoskeleton robotic device for hand rehabilitation," *Journal of Hand Therapy*, vol. 33, no. 2, pp. 198–208, 2020.

[43] J. C. Castiblanco, I. F. Mondragon, C. Alvarado-Rojas, and J. D. Colorado, "Assist-as-needed exoskeleton for hand joint rehabilitation based on muscle effort detection," *Sensors*, vol. 21, no. 13, p. 4372, 2021.

[44] N. Sun, G. Li, and L. Cheng, "Design and validation of a self-aligning index finger exoskeleton for post-stroke rehabilitation," *IEEE Transactions on Neural Systems and Rehabilitation Engineering*, vol. 29, pp. 1513–1523, 2021.

[45] G. Li, L. Cheng, and N. Sun, "Design, manipulability analysis and optimization of an index finger exoskeleton for stroke rehabilitation," *Mechanism and Machine Theory*, vol. 167, p. 104526, 2022.

[46] L. Bartalucci, N. Secciani, C. Brogi, A. Topini, A. Della Valle, A. Ridolfi, and B. Allotta, "An original mechatronic design of a kinaesthetic hand exoskeleton for virtual reality-based applications," *Mechatronics*, vol. 90, p. 102947, 2023.

[47] B. A. De la Cruz-Sánchez, M. Arias-Montiel, and E. Lugo-González, "Emg-controlled hand exoskeleton for assisted bilateral rehabilitation," *Biocybernetics and Biomedical Engineering*, vol. 42, no. 2, pp. 596–614, 2022.

[48] Y. Yun, S. Dancausse, P. Esmatloo, A. Serrato, C. A. Merring, P. Agarwal, and A. D. Deshpande, "Maestro: An emg-driven assistive hand exoskeleton for spinal cord injury patients," in *2017 IEEE international conference on robotics and automation (ICRA)*, pp. 2904–2910, IEEE, 2017.

[49] L. Cappello, J. T. Meyer, K. C. Galloway, J. D. Peisner, R. Granberry, D. A. Wagner, S. Engelhardt, S. Paganoni, and C. J. Walsh, "Assisting hand function after spinal cord injury with a fabric-based soft robotic glove," *Journal of neuroengineering and rehabilitation*, vol. 15, no. 1, pp. 1–10, 2018.

[50] H. In, B. B. Kang, M. Sin, and K.-J. Cho, "Exo-glove: A wearable robot for the hand with a soft tendon routing system," *IEEE Robotics & Automation Magazine*, vol. 22, no. 1, pp. 97–105, 2015.

[51] C. G. Rose and M. K. O'Malley, "Hybrid rigid-soft hand exoskeleton to assist functional dexterity," *IEEE Robotics and Automation Letters*, vol. 4, no. 1, pp. 73–80, 2018.

[52] J. Dittli, U. Hofmann, T. Bützer, O. Lambercy, and R. Gassert, "Remote actuation systems for fully wearable assistive devices: requirements, selection, and optimization for out-of-the-lab application of a hand exoskeleton," *Frontiers in Robotics and AI*, vol. 7, p. 187, 2020.

[53] D. Popov, I. Gaponov, and J.-H. Ryu, "Portable exoskeleton glove with soft structure for hand assistance in activities of daily living," *IEEE/ASME Transactions on Mechatronics*, vol. 22, no. 2, pp. 865–875, 2016.

[54] N. Secciani, C. Brogi, M. Pagliai, F. Buonamici, F. Gerli, F. Vannetti, M. Bianchini, Y. Volpe, and A. Ridolfi, "Wearable robots: An original mechatronic design of a hand exoskeleton for assistive and rehabilitative purposes," *Frontiers in Neurorobotics*, vol. 15, 2021.

[55] T. Bagneschi, D. Chiaradia, G. Righi, G. Del Popolo, A. Frisoli, and D. Leonardis, "a soft hand exoskeleton with a novel tendon layout to improve stable wearing in grasping assistance," *IEEE Transactions on Haptics*, 2023.

[56] W. Chen, "Underactuated base-to-distal hand exoskeleton for adaptive grasping assistance," 2023.

[57] E. R. Triolo and B. F. BuSha, "Design and experimental testing of a force-augmenting exoskeleton for the human hand," *Journal of NeuroEngineering and Rehabilitation*, vol. 19, no. 1, pp. 1–16, 2022.

[58] J. C. Maldonado-Mejía, M. Múnera, C. A. Diaz, H. Wurdemann, M. Moazen, M. J. Pontes, M. E. Vieira Segatto, M. E. Monteiro, and C. A. Cifuentes, "A fabric-based soft hand exoskeleton for assistance: the exhand exoskeleton," *Frontiers in Neurorobotics*, vol. 17, p. 1091827, 2023.

[59] I. Sarakoglou, A. Brygo, D. Mazzanti, N. G. Hernandez, D. G. Caldwell, and N. G. Tsagarakis, "Hexotrac: A highly under-actuated hand exoskeleton for finger tracking and force feedback," in *2016 IEEE/RSJ International Conference on Intelligent Robots and Systems (IROS)*, pp. 1033–1040, IEEE, 2016.

[60] E. Amirpour, R. Fesharakifard, H. Ghafarirad, S. M. Rezaei, A. Saboukhi, M. Savabi, and M. R. Gorji, "A novel hand exoskeleton to enhance fingers motion for tele-operation of a robot gripper with force feedback," *Mechatronics*, vol. 81, p. 102695, 2022.

[61] W. Wei, B. Zhou, B. Fan, M. Du, G. Bao, and S. Cai, "An adaptive hand exoskeleton for teleoperation system," *Chinese Journal of Mechanical Engineering*, vol. 36, no. 1, p. 60, 2023.

[62] H. Al-Fahaam, S. Davis, S. Nefti-Meziani, and T. Theodoridis, "Novel soft bending actuator-based power augmentation hand exoskeleton controlled by human intention," *Intelligent Service Robotics*, vol. 11, pp. 247–268, 2018.

[63] P. W. Ferguson, Y. Shen, and J. Rosen, "Hand exoskeleton systems—overview," *Wearable Robotics*, pp. 149–175, 2020.

[64] M. Sarac, M. Solazzi, and A. Frisoli, "Design requirements of generic hand exoskeletons and survey of hand exoskeletons for rehabilitation, assistive, or haptic use," *IEEE Transactions on Haptics*, vol. 12, no. 4, pp. 400–413, 2019.

[65] T. Desplenter, Y. Zhou, B. P. Edmonds, M. Lidka, A. Goldman, and A. L. Trejos, "Rehabilitative and assistive wearable mechatronic upper-limb devices: A review," *Journal of Rehabilitation and Assistive Technologies Engineering*, vol. 7, p. 2055668320917870, 2020.

[66] Y. Bouteraa, I. B. Abdallah, and A. M. Elmogy, "Training of hand rehabilitation using low cost exoskeleton and vision-based game interface," *Journal of Intelligent & Robotic Systems*, vol. 96, no. 1, pp. 31–47, 2019.

[67] M. Sandison, K. Phan, R. Casas, L. Nguyen, M. Lum, M. Pergami-Peries, and P. S. Lum, "Handmate: Wearable robotic hand exoskeleton and integrated android app for at home stroke rehabilitation," in *2020 42nd Annual International Conference of the IEEE Engineering in Medicine & Biology Society (EMBC)*, pp. 4867–4872, IEEE, 2020.

[68] M. Dragusanu, M. Z. Iqbal, T. L. Baldi, D. Prattichizzo, and M. Malvezzi, "Design, development, and control of a hand/wrist exoskeleton for rehabilitation and training," *IEEE Transactions on Robotics*, vol. 38, no. 3, pp. 1472–1488, 2022.

[69] N. Kladovasilakis, I. Kostavelis, P. Sideridis, E. Koltzi, K. Piliounis, D. Tzetzis, and D. Tzovaras, "A novel soft robotic exoskeleton system for hand rehabilitation and assistance purposes," *Applied Sciences*, vol. 13, no. 1, p. 553, 2023.

[70] N. Ho, K. Tong, X. Hu, K. Fung, X. Wei, W. Rong, and E. Susanto, "An emg-driven exoskeleton hand robotic training device on chronic stroke subjects: task training system for stroke rehabilitation," in *2011 IEEE international conference on rehabilitation robotics*, pp. 1–5, IEEE, 2011.

[71] O. Lambercy, D. Schröder, S. Zwicker, and R. Gassert, "Design of a thumb exoskeleton for hand rehabilitation," in *Proceedings of the 7th international convention on rehabilitation engineering and assistive technology*, p. 41, Singapore Therapeutic, Assistive & Rehabilitative Technologies (START) Centre, 2013.

[72] P. Polygerinos, Z. Wang, K. C. Galloway, R. J. Wood, and C. J. Walsh, "Soft robotic glove for combined assistance and at-home rehabilitation," *Robotics and Autonomous Systems*, vol. 73, pp. 135–143, 2015.

[73] L. Randazzo, I. Iturrate, S. Perdikis, and J. d. R. Millán, "mano: A wearable hand exoskeleton for activities of daily living and neurorehabilitation," *IEEE Robotics and Automation Letters*, vol. 3, no. 1, pp. 500–507, 2017.

[74] D. Wang, Q. Meng, Q. Meng, X. Li, and H. Yu, "Design and development of a portable exoskeleton for hand rehabilitation," *IEEE Transactions on Neural Systems and Rehabilitation Engineering*, vol. 26, no. 12, pp. 2376–2386, 2018.

[75] A. Yurkewich, I. J. Kozak, A. Ivanovic, D. Rossos, R. H. Wang, D. Hebert, and A. Mihailidis, "Myoelectric untethered robotic glove enhances hand function and performance on daily living tasks after stroke," *Journal of rehabilitation and assistive technologies engineering*, vol. 7, p. 2055668320964050, 2020.

[76] A. Hadi, K. Alipour, S. Kazeminasab, and M. Elahinia, "Asr glove: A wearable glove for hand assistance and rehabilitation using shape memory alloys," *Journal of Intelligent Material Systems and Structures*, vol. 29, no. 8, pp. 1575–1585, 2018.

[77] K. Tong, S. Ho, P. Pang, X. Hu, W. Tam, K. Fung, X. Wei, P. Chen, and M. Chen, "An intention driven hand functions task training robotic system," in *2010 Annual International Conference of the IEEE Engineering in Medicine and Biology*, pp. 3406–3409, IEEE, 2010.

[78] B. W. Ang and C.-H. Yeow, "Print-it-yourself (piy) glove: a fully 3d printed soft robotic hand rehabilitative and assistive exoskeleton for stroke patients," in *2017 IEEE/RSJ International Conference on Intelligent Robots and Systems (IROS)*, pp. 1219–1223, IEEE, 2017.

[79] D. Esposito, J. Centracchio, E. Andreozzi, S. Savino, G. D. Gargiulo, G. R. Naik, and P. Bifulco, "Design of a 3d-printed hand exoskeleton based on force-myography control for assistance and rehabilitation," *Machines*, vol. 10, no. 1, p. 57, 2022.

[80] Q. A. Boser, M. R. Dawson, J. S. Schofield, G. Y. Dziwenko, and J. S. Hebert, "Defining the design requirements for an assistive powered hand exoskeleton: A pilot explorative interview study and case series," *Prosthetics and Orthotics International*, p. 0309364620963943, 2020.

[81] A. F. Pérez Vidal, J. Y. Rumbo Morales, G. Ortiz Torres, F. d. J. Sorcia Vázquez, A. Cruz Rojas, J. A. Brizuela Mendoza, and J. C. Rodríguez Cerda, "Soft exoskeletons: Development, requirements, and challenges of the last decade," in *Actuators*, vol. 10, p. 166, MDPI, 2021.

[82] F. Montagnani, M. Controzzi, and C. Cipriani, "Independent long fingers are not essential for a grasping hand," *Scientific reports*, vol. 6, p. 35545, 2016.

[83] M. Riddle, K. MacDermid-Watts, S. Holland, J. C. MacDermid, E. Lalone, and L. Ferreira, "Wearable strain gauge-based technology measures manual tactile forces during the activities of daily living," *Journal of rehabilitation and assistive technologies engineering*, vol. 5, p. 2055668318793587, 2018.

[84] J. Cepriá-Bernal and A. Pérez-González, "Dataset of tactile signatures of the human right hand in twenty-one activities of daily living using a high spatial resolution pressure sensor," *Sensors*, vol. 21, no. 8, p. 2594, 2021.

[85] K. Matheus and A. M. Dollar, "Benchmarking grasping and manipulation: Properties of the objects of daily living," in *2010 IEEE/RSJ International Conference on Intelligent Robots and Systems*, pp. 5020–5027, IEEE, 2010.

[86] B. Noronha and D. Accoto, "Exoskeletal devices for hand assistance and rehabilitation: A comprehensive analysis of state-of-the-art technologies," *IEEE Transactions on Medical Robotics and Bionics*, vol. 3, no. 2, pp. 525–538, 2021.

[87] P. Tran, S. Jeong, K. R. Herrin, and J. P. Desai, "Hand exoskeleton systems, clinical rehabilitation practices, and future prospects," *IEEE Transactions on Medical Robotics and Bionics*, vol. 3, no. 3, pp. 606–622, 2021.

[88] J. Iqbal, N. G. Tsagarakis, and D. G. Caldwell, "A multi-dof robotic exoskeleton interface for hand motion assistance," in *2011 Annual International Conference of the IEEE Engineering in Medicine and Biology Society*, pp. 1575–1578, IEEE, 2011.

[89] A. Chiri, N. Vitiello, F. Giovacchini, S. Roccella, F. Vecchi, and M. C. Carrozza, "Mechatronic design and characterization of the index finger module of a hand exoskeleton for post-stroke rehabilitation," *IEEE/ASmE Transactions on mechatronics*, vol. 17, no. 5, pp. 884–894, 2011.

[90] M. Cempini, M. Cortese, and N. Vitiello, "A powered finger–thumb wearable hand exoskeleton with self-aligning joint axes," *IEEE/ASME Transactions on mechatronics*, vol. 20, no. 2, pp. 705–716, 2014.

[91] A. Wege, K. Kondak, and G. Hommel, "Mechanical design and motion control of a hand exoskeleton for rehabilitation," in *IEEE International Conference Mechatronics and Automation, 2005*, vol. 1, pp. 155–159, IEEE, 2005.

[92] G. Zong, X. Pei, J. Yu, and S. Bi, "Classification and type synthesis of 1-dof remote center of motion mechanisms," *Mechanism and Machine Theory*, vol. 43, no. 12, pp. 1585–1595, 2008.

[93] J. Li, R. Zheng, Y. Zhang, and J. Yao, "ihandrehab: An interactive hand exoskeleton for active and passive rehabilitation," in *2011 IEEE International Conference on Rehabilitation Robotics*, pp. 1–6, IEEE, 2011.

[94] M. Fontana, S. Fabio, S. Marcheschi, and M. Bergamasco, "Haptic hand exoskeleton for precision grasp simulation," *Journal of Mechanisms and Robotics*, vol. 5, no. 4, 2013.

[95] A. Battezzato, “Kinetostatic analysis and design optimization of an n-finger underactuated hand exoskeleton,” *Mechanism and Machine Theory*, vol. 88, pp. 86–104, 2015.

[96] R. Conti, E. Meli, A. Ridolfi, M. Bianchi, L. Governi, Y. Volpe, and B. Allotta, “Kinematic synthesis and testing of a new portable hand exoskeleton,” *Meccanica*, vol. 52, no. 11-12, pp. 2873–2897, 2017.

[97] I. Jo and J. Bae, “Design and control of a wearable and force-controllable hand exoskeleton system,” *Mechatronics*, vol. 41, pp. 90–101, 2017.

[98] W. Chen, G. Li, N. Li, W. Wang, P. Yu, R. Wang, X. Xue, X. Zhao, and L. Liu, “Soft exoskeleton with fully actuated thumb movements for grasping assistance,” *IEEE Transactions on Robotics*, vol. 38, no. 4, pp. 2194–2207, 2022.

[99] C.-Y. Chu and R. M. Patterson, “Soft robotic devices for hand rehabilitation and assistance: a narrative review,” *Journal of neuroengineering and rehabilitation*, vol. 15, no. 1, p. 9, 2018.

[100] S. K. Manna and V. N. Dubey, “Comparative study of actuation systems for portable upper limb exoskeletons,” *Medical engineering & physics*, vol. 60, pp. 1–13, 2018.

[101] M. Pan, C. Yuan, X. Liang, T. Dong, T. Liu, J. Zhang, J. Zou, H. Yang, and C. Bowen, “Soft actuators and robotic devices for rehabilitation and assistance,” *Advanced Intelligent Systems*, vol. 4, no. 4, p. 2100140, 2022.

[102] S. Grosu, L. De Rijcke, V. Grosu, J. Geeroms, B. Vanderboght, D. Lefeber, and C. Rodriguez-Guerrero, “Driving robotic exoskeletons using cable-based transmissions: A qualitative analysis and overview,” *Applied Mechanics Reviews*, vol. 70, no. 6, 2018.

[103] M. Li, Y. Zhuo, B. He, Z. Liang, G. Xu, J. Xie, and S. Zhang, “A 3d-printed soft hand exoskeleton with finger abduction assistance,” in *2019 16th International Conference on Ubiquitous Robots (UR)*, pp. 319–322, IEEE, 2019.

[104] Y. M. Zhou, D. Wagner, K. Nuckols, R. Heimgartner, C. Correia, M. Clarke, D. Orzel, C. O’Neill, R. Solinsky, S. Paganoni, *et al.*, “Soft robotic glove with integrated sensing for intuitive grasping assistance post spinal cord injury,” in *2019 International conference on robotics and automation (ICRA)*, pp. 9059–9065, IEEE, 2019.

[105] M. Bianchi, F. Fanelli, E. Meli, A. Ridolfi, F. Vannetti, M. Bianchini, and B. Allotta, "Optimization-based scaling procedure for the design of fully portable hand exoskeletons," *Meccanica*, vol. 53, no. 11-12, pp. 3157–3175, 2018.

[106] T. Burton, R. Vaidyanathan, S. Burgess, A. Turton, and C. Melhuish, "Development of a parametric kinematic model of the human hand and a novel robotic exoskeleton," in *2011 IEEE International Conference on Rehabilitation Robotics*, pp. 1–7, IEEE, 2011.

[107] Y. Huang and K. Low, "Initial analysis and design of an assistive rehabilitation hand device with free loading and fingers motion visible to subjects," in *2008 IEEE International Conference on Systems, Man and Cybernetics*, pp. 2584–2590, IEEE, 2008.

[108] N. Secciani, M. Bianchi, A. Ridolfi, F. Vannetti, Y. Volpe, L. Governi, M. Bianchini, and B. Allotta, "Tailor-made hand exoskeletons at the university of florence: From kinematics to mechatronic design," *Machines*, vol. 7, no. 2, p. 22, 2019.

[109] N. Secciani, M. Bianchi, E. Meli, Y. Volpe, and A. Ridolfi, "A novel application of a surface electromyography-based control strategy for a hand exoskeleton system: A single-case study," *International Journal of Advanced Robotic Systems*, vol. 16, no. 1, p. 1729881419828197, 2019.

[110] N. Secciani, A. Topini, A. Ridolfi, E. Meli, and B. Allotta, "A novel point-in-polygon-based semg classifier for hand exoskeleton systems," *IEEE Transactions on Neural Systems and Rehabilitation Engineering*, 2020.

[111] W. De Weerdt and M. Harrison, "Measuring recovery of arm-hand function in stroke patients: a comparison of the brunnstrom-fugl-meyer test and the action research arm test," *Physiotherapy Canada*, vol. 37, no. 2, pp. 65–70, 1985.

[112] N. Yozbatiran, L. Der-Yeghiaian, and S. C. Cramer, "A standardized approach to performing the action research arm test," *Neurorehabilitation and neural repair*, vol. 22, no. 1, pp. 78–90, 2008.

[113] M. McDonnell, "Action research arm test," *Aust J Physiother*, vol. 54, no. 3, p. 220, 2008.

[114] D. Rodriguez-Cianca, C. Rodriguez-Guerrero, T. Verstraten, R. Jimenez-Fabian, B. Vanderborght, and D. Lefeber, "A flexible shaft-driven remote and torsionally compliant actuator (rtca) for wearable robots," *Mechatronics*, vol. 59, pp. 178–188, 2019.

[115] C. J. Nycz, T. Bützer, O. Lambercy, J. Arata, G. S. Fischer, and R. Gassert, "Design and characterization of a lightweight and fully portable remote actuation system for use with a hand exoskeleton," *IEEE Robotics and Automation Letters*, vol. 1, no. 2, pp. 976–983, 2016.

[116] C. Brogi, N. Secciani, L. Bartalucci, M. Pagliai, B. Allotta, A. Ridolfi, and A. Rindi, "Wearable exoskeletons for hand assistance: Concept and design of a thumb module with hybrid architecture," in *Symposium on Robot Design, Dynamics and Control*, pp. 70–78, Springer, 2022.

[117] C. Brogi, N. Secciani, L. Bartalucci, F. Di Iorio, E. Meli, M. Rinchi, B. Allotta, and A. Ridolfi, "An original hybrid-architecture finger mechanism for wearable hand exoskeletons," *Mechatronics*, vol. 98, p. 103117, 2024.

[118] H.-T. Lin, L.-C. Kuo, H.-Y. Liu, W.-L. Wu, and F.-C. Su, "The three-dimensional analysis of three thumb joints coordination in activities of daily living," *Clinical Biomechanics*, vol. 26, no. 4, pp. 371–376, 2011.

[119] P. Braido and X. Zhang, "Quantitative analysis of finger motion coordination in hand manipulative and gestic acts," *Human movement science*, vol. 22, no. 6, pp. 661–678, 2004.

[120] F. Chen Chen, S. Appendino, A. Battezzato, A. Favetto, M. Mousavi, F. Pescarmona, *et al.*, "Constraint study for a hand exoskeleton: human hand kinematics and dynamics," *Journal of Robotics*, vol. 2013, 2013.

[121] G. I. Bain, N. Polites, B. Higgs, R. Heptinstall, and A. McGrath, "The functional range of motion of the finger joints," *Journal of Hand Surgery (European Volume)*, vol. 40, no. 4, pp. 406–411, 2015.

[122] A. A. Shabana, "Flexible multibody dynamics: review of past and recent developments," *Multibody system dynamics*, vol. 1, pp. 189–222, 1997.

[123] S. K. Dwivedy and P. Eberhard, "Dynamic analysis of flexible manipulators, a literature review," *Mechanism and machine theory*, vol. 41, no. 7, pp. 749–777, 2006.

[124] S. Arbatani, A. Callejo, J. Kövecses, M. Kalantari, N. R. Marchand, and J. Dargahi, "An approach to directional drilling simulation: finite element and finite segment methods with contact," *Computational Mechanics*, vol. 57, pp. 1001–1015, 2016.

[125] M. Liu and D. G. Gorman, "Formulation of rayleigh damping and its extensions," *Computers & structures*, vol. 57, no. 2, pp. 277–285, 1995.

[126] P. Flores, M. Machado, M. T. Silva, and J. M. Martins, "On the continuous contact force models for soft materials in multibody dynamics," *Multibody system dynamics*, vol. 25, pp. 357–375, 2011.

[127] L. Skrinjar, J. Slavič, and M. Boltežar, "A review of continuous contact-force models in multibody dynamics," *International Journal of Mechanical Sciences*, vol. 145, pp. 171–187, 2018.

[128] E. Pennestrì, V. Rossi, P. Salvini, and P. P. Valentini, "Review and comparison of dry friction force models," *Nonlinear dynamics*, vol. 83, pp. 1785–1801, 2016.

[129] S. Petkun, "Modelling of friction in mechatronics systems," *Tagungsband*, p. 170.